

CHEMICAL EVOLUTION OF TURBULENT PROTOPLANETARY DISKS AND THE SOLAR NEBULA

D. SEMENOV¹

Max Planck Institute for Astronomy, Königstuhl 17, D-69117 Heidelberg, Germany

AND

D. WIEBE

Institute of Astronomy of the RAS, Pyatnitskaya St. 48, 119017 Moscow, Russia

Draft version January 20, 2013

ABSTRACT

This is the second paper in a series where we study the influence of transport processes on the chemical evolution of protoplanetary disks. Our analysis is based on a 1+1D flared α -model of a ~ 5 Myr DM Tau-like system, coupled to a large gas-grain chemical network. To account for production of complex molecules, the chemical network is supplied with an extended set of surface reactions and photo-processes in ice mantles. Our chemo-dynamical disk model covers a wide range of radii, 10–800 AU (from a Jovian planet-forming zone to the outer disk edge). Turbulent transport of gases and ices is implicitly modeled in full 2D along with the time-dependent chemistry, using the mixing-length approximation. Two regimes are considered, with high and low efficiency of turbulent mixing. The results of the chemical model with suppressed turbulent diffusion are close to those from the laminar model, but not completely. A simple analysis for the laminar chemical model to highlight potential sensitivity of a molecule to transport processes is performed. It is shown that the higher the ratio of the characteristic chemical timescale to the turbulent transport timescale for a given molecule, the higher the probability that its column density will be affected by diffusion. We find that turbulent transport enhances abundances and column densities of many gas-phase species and ices, particularly, complex ones. For such species a chemical steady-state is not reached due to long timescales associated with evaporation and surface photoprocessing and recombination ($t \gtrsim 10^5$ years). When a grain with an icy mantle is transported from a cold disk midplane into a warm intermediate/inner region, heavy radicals become mobile on the surface, enriching the mantle with complex ices, which are eventually released into the gas phase. The influence of turbulent mixing on disk chemistry is more pronounced in the inner, planet-forming disk region where gradients of temperature and high-energy radiation intensities are steeper than in the outer region. In contrast, simple radicals and molecular ions, which chemical evolution is fast and proceeds solely in the gas phase, are not much affected by dynamics. All molecules are divided into three groups according to the sensitivity of their column densities to the turbulent diffusion. The molecules that are unresponsive to transport include, e.g., C₂H, C⁺, CH₄, CN, CO, HCN, HNC, H₂CO, OH, as well as water and ammonia ice. Their column densities computed with the laminar and 2D-mixing model differ by a factor of $\lesssim 2-5$ (“steadfast” species). Molecules which vertical column densities in the laminar and dynamical models differ by up to 2 order of magnitude include, e.g., C₂H₂, some carbon chains, CS, H₂CS, H₂O, HCO⁺, HCOOH, HNCO, N₂H⁺, NH₃, CO ice, H₂CO ice, CH₃OH ice, and electrons (“sensitive” species). Molecules which column densities are altered by diffusion by more than 2 orders of magnitude include, e.g., C₂S, C₃S, C₆H₆, CO₂, O₂, SiO, SO, SO₂, long carbon chain ices, CH₃CHO ice, HCOOH ice, O₂ ice, and OCN ice (“hypersensitive” species). The chemical evolution of assorted molecules in the laminar and turbulent models is thoroughly analyzed and compared with previous studies. We find that column densities of observed gas-phase molecules in the DM Tau disk are well reproduced by both the laminar and the chemo-dynamical disk models. The observed abundances of many reduced and oxidized cometary ices are also successfully reproduced by the both models. We indicate several observable or potentially detectable tracers of transport processes in protoplanetary disks and the Solar nebula, e.g., elevated concentrations of heavy hydrocarbon ices, complex organics, CO₂, O₂, SO, SO₂, C₂S, C₃S compared to CO and the water ice. A combination of UV photodesorption, grain growth, and turbulent mixing leads to non-negligible amount of molecular gases in the cold disk midplane.

Subject headings: accretion, accretion disks — astrochemistry — molecular processes — protoplanetary disks — stars: DM Tau — turbulence

1. INTRODUCTION

One of the most exciting questions in astrophysics is the genesis of prebiotic molecules served as life-building blocks in the Solar system and preserved in meteorites and comets. Nowadays protoplanetary disks are believed to be birth places

semenov@mpia.de
 dwiebe@inasan.ru

¹ Visiting Astronomer, Astronomy Department, University of California, Berkeley, CA 94720-3411, USA

of planetary systems, so we may expect prebiotic molecules to be the eventual outcome of the disk evolution. However, our understanding of the chemical composition and evolution of protoplanetary disks is far from being complete. Apart from CO and its isotopologues, and occasionally HCO⁺, DCO⁺, CN, HCN, DCN, CCH, H₂CO, and CS, the molecular content of protoplanetary disks remains largely unknown (e.g., Dutrey et al. 1997; Kastner et al. 1997; Aikawa et al. 2003; Thi et al. 2004; Piétu et al. 2007; Qi et al.

2008; Henning et al. 2010). Molecular line data are limited in their sensitivity and resolution. This means that spatial distribution of molecular abundances in disks is still poorly determined (e.g., Piétu et al. 2005; Dutrey et al. 2007b; Panić et al. 2009), hampering a detailed comparison with existing chemical models, which is often based on global data (e.g. integrated line profiles).

Multi-molecule, multi-transition interferometric observations, coupled to line radiative transfer and chemical modeling, allowed to constrain disk sizes, kinematics, distribution of temperature, surface density, and molecular column densities (see reviews by Bergin et al. (2007) and Dutrey et al. (2007a)). The measured line intensities are indicative of vertical temperature gradients in disks (e.g., Dartois et al. 2003; Qi et al. 2006), though several disks with large inner cavities do not show evidence for such a gradient (e.g., GM Aur and LkCa 15; Dutrey et al. 2008; Hughes et al. 2009). A significant reservoir of very cold CO, HCO⁺, CN and HCN gases has been found in the disk of DM Tau at temperatures \lesssim 6–17 K, which cannot be explained by conventional chemical models without invoking a non-thermal desorption or transport mechanism (e.g., Semenov et al. 2006; Aikawa 2007; Hersant et al. 2009). Non-thermal broadening of emission lines of $\sim 0.1 \text{ km s}^{-1}$ has been reported (e.g., Bergin et al. 2007; Dutrey et al. 2007a; Hughes et al. 2011), which is likely due to subsonic turbulence driven by the magnetorotational instability (Balbus & Hawley 1991).

Recently, with space-borne (*Spitzer*) and ground-based (Keck, VLT, Subaru) infrared telescopes, molecules have been detected in very inner zones of planet-forming systems, at $r \lesssim 1 - 10 \text{ AU}$. Rotational-vibrational emission lines from CO, CO₂, C₂H₂, HCN, OH, H₂O imply a rich chemistry driven by endothermic reactions or reactions with activation barriers and photoprocesses (Lahuis et al. 2006; Carr & Najita 2008; Salyk et al. 2008; Pontoppidan et al. 2008a; Pascucci et al. 2009; van der Plas et al. 2009; Salyk et al. 2011). Through *ISO* and *Spitzer* infrared spectroscopy abundant ices in cold disk regions consisting of water ice and substantial amounts ($\sim 1 - 30\%$) of volatile materials like CO, CO₂, NH₃, CH₄, H₂CO, and HCOOH have been detected (e.g., Pontoppidan et al. 2005; Terada et al. 2007; Zasowski et al. 2009).

The conditions of planets formation in the early Solar system have been revealed by a detailed analysis of chemical and mineralogical composition of meteoritic samples and cometary dust particles (e.g., Bradley 2005). The recent *Stardust* and *Genesis* space missions have returned first samples of pristine materials, likely of cometary origin, showing a complex structure of high-temperature crystalline silicates embedded in low-temperature condensates (Brownlee et al. 2004; Flynn et al. 2006; Brownlee et al. 2008). Comets have been assembled around or beyond Neptune and expelled gravitationally outward, however the presence of Mg-rich crystalline silicates in cometary dust indicates annealing of amorphous presolar grains at temperatures above 800 K (Wooden et al. 1999, 2007). The presence of crystalline silicates in outer regions of protoplanetary disks has also been revealed (e.g., van Boekel et al. 2004; Juhász et al. 2010).

Recently, an anti-correlation between the age of a disk and the X-ray hardness/luminosity of a central star, and the observed crystallinity fraction has been inferred, making the overall picture even more complicated (e.g., Glauser et al. 2009).

An isotopic analysis of refractory condensates in unaltered chondritic meteorites shows strong evidence that the inner part of the Solar Nebula has been almost completely mixed during the first several Myr of evolution (e.g., Boss 2004; Ciesla 2009). This mixing (either advective or turbulent), along with high-energy irradiation, could have also been important for fractionation ratios in both gas-phase and solid compounds in the nebula (e.g., Clayton 1993; Clayton & Mayeda 1996; Lee et al. 1998b; Hersant et al. 2001; Lyons & Young 2005). The rich variety of organic compounds in meteorites, including amino acids, suggest that these complex species have formed just prior or during the formation of planets in heavily irradiated, warm regions of the Solar Nebula (e.g., Ehrenfreund & Charnley 2000; Busemann et al. 2006). Combustion and pyrolysis of hydrocarbons at high temperatures, coupled with outward transport, has been inferred to explain the omni-presence of kerogen-like (mainly aromatic) carbonaceous material in meteoritic and cometary samples (Morgan et al. 1991).

These intriguing findings are partly understood in modern astrochemical models of protoplanetary disks (Willacy & Langer 2000; Aikawa et al. 2002; Markwick et al. 2002; van Zadelhoff et al. 2003; Ilgner et al. 2004; Kamp & Dullemond 2004; Semenov et al. 2005; Aikawa & Nomura 2006; Tscharnutter & Gail 2007; Agúndez et al. 2008; Woods & Willacy 2009; Visser et al. 2009b; Walsh et al. 2010). The major result of the chemical modeling is that disks have a layered chemical structure due to heavy freeze-out of gas-phase molecules in the cold midplane and their photodissociation in the atmosphere. Vertical column densities of CO, HCO⁺, N₂H⁺, CN, HCN, HNC, CS, etc. are reproduced with modern chemical models (e.g., Aikawa et al. 2002; Semenov et al. 2005; Willacy et al. 2006; Dutrey et al. 2007b; Schreyer et al. 2008; Henning et al. 2010).

While most of the chemical studies are still based on laminar disk models, evidences for mixing, mentioned above, call for a more sophisticated treatment. A few such dynamical studies have been presented. Models of the early Solar nebula with radial transport by advective flows have been developed (e.g., Morfill & Völk 1984; Gail 2001, 2002; Wehrstedt & Gail 2002; Boss 2004; Keller & Gail 2004). Ilgner et al. (2004) for the first time simultaneously modeled the influence of turbulent diffusion in the vertical direction and advection flows in the radial direction on the chemical composition of the inner disk region. They found that dynamical processes significantly affect the chemical evolution of sulfur-bearing species. Willacy et al. (2006) have shown that 1D vertical mixing modifies chemical composition of the outer disk region and that the mixing results better agree to observations. Semenov et al. (2006, Paper I) and Aikawa (2007) have found that turbulent transport allows explaining the presence of a large amount of cold ($\lesssim 15 \text{ K}$) CO gas in the disk of DM Tau. Tscharnutter & Gail (2007) have used a 2D disk chemo-hydrodynamical model and showed that in the disk midplane matter moves outward, carrying out the angular momentum, while the accretion flows toward the star are located at elevated altitudes. Consequently, gas-phase species produced by warm chemistry in the inner nebula can be steadily transported into the cold outer region and freeze out. Tscharnutter & Gail (2007) have claimed that global radial advective flows dominate over diffusive mixing for the disk chemical evolution. A radial advection model has also been utilized by Nomura et al. (2009),

who have demonstrated that inward radial transport enhances abundances of organic molecules (produced mainly on dust surfaces in cold outer regions). Woods & Willacy (2009) have elaborated a disk chemical model with improved heating and cooling balance and accurate modeling of the UV radiation field and found that the $^{12}\text{C}/^{13}\text{C}$ fractionation in the Solar system comets can be explained by the reprocessing of presolar materials in a warm nebular region. Hersant et al. (2009) have studied various mechanisms to retain gas-phase CO in very cold disk regions. They concluded that efficient photodesorption in moderately obscured disk regions ($A_V < 5^m$) greatly enhances gas-phase CO concentrations, while the role of vertical mixing is less important. Finally, Heinzeller et al. (2011) have investigated the disk chemical evolution with radial advection, vertical mixing, and vertical wind transport processes. They have found that the disk wind has a negligible effect on disk chemistry, whereas the radial accretion alters the molecular abundances in the cold midplane, and the vertical turbulent mixing affects the chemistry in the warm molecular layer. The abundances of NH₃, CH₃OH, C₂H₂ and sulfur-containing species are the most enhanced by the transport.

In this paper we continue our detailed study of chemo-dynamical interactions in protoplanetary disk started in Paper I with an intent to find out if chemistry can be used as a diagnostic of dynamical processes in a protoplanetary accretion disk. For the first time we utilize a large-scale disk physical model along with an extended gas-grain chemical network coupled to 2D turbulent transport. A wide range of temperatures, densities, and X-ray/UV radiation intensities encountered in this dynamical model allows us to follow formation and destruction of various molecules, possibly detectable with ALMA and *Herschel*. The primary aim of the present study is to characterize the importance of turbulent diffusion for the chemical evolution in various disk domains and for various chemical families. We argue that even though the overall efficiency of the diffusive transport in the outer disk is dominated by vertical mixing, one has to consider vertical and radial mixing simultaneously in the planet-forming region. Many complex ices and their gas-phase counterparts are enhanced by turbulent diffusion, in particular sulfur-bearing and other heavy (complex) species.

The organization of the paper is the following. In Section 2 we describe the adopted disk physical model and the chemical network. In Sect. 3.1 basic chemical and dynamical timescales in protoplanetary disks are outlined and discussed. A general scheme to estimate possible sensitivity of a given molecule to transport processes is presented in Sect. 3.2. Influence of the 2D-turbulent diffusion on the chemical evolution of dominant ions as well as C-, O-, N-, S-bearing species and complex organic molecules is studied in detail in Sects. 4.1-4.6. Detailed comparison with the previous studies and future improvements of chemo-dynamical models are discussed in Sect. 5.1. We discuss importance of turbulent diffusion for the presence of cold gases in disk midplanes in Sect. 5.2. We verify feasibility of our chemical and physical disk models by comparing the calculated and observed column densities in the DM Tau disk and abundances of cometary ices in the Solar system (Sect. 5.3). Finally, detected or potentially detectable molecular tracers of transport processes in protoplanetary disks are summarized in Sect. 5.4. Summary and conclusions follow.

2. MODEL

2.1. Disk structure

We focus on the DM Tau system because it is one of the most observationally studied and molecularly-rich protoplanetary disk around a T Tauri star. The adopted flaring disk structure is based on a 1+1D steady-state α -model similar to D'Alessio et al. (1999) model. The DM Tau is a single M0.5 dwarf ($T_{\text{eff}} = 3720$ K), with a mass of $0.65M_{\odot}$, and a radius of $1.2R_{\odot}$ (Mazzitelli 1989; Simon et al. 2000). The non-thermal FUV radiation field from DM Tau is represented by the scaled ISRF of Draine (1978), with the un-attenuated intensity at 100 AU of $\chi_*(100) = 410$ (e.g., Bergin et al. 2003). For the X-ray luminosity of the star we adopt a value of 10^{30} erg s⁻¹, which is constrained by recent measurements with Chandra and XMM in the range of 0.3-10 keV (M. Guedel, priv. comm.).

The disk has an inner radius $r_0 = 0.03$ AU (dust sublimation front, $T \approx 1500$ K), an outer radius $r_1 = 800$ AU, an accretion rate $\dot{M} = 4 \cdot 10^{-9} M_{\odot} \text{ yr}^{-1}$, a viscosity parameter $\alpha = 0.01$, and a mass of $M = 0.066M_{\odot}$ (Dutrey et al. 2007b; Henning et al. 2010). The DM Tau disk age is about 5–7 Myr (Simon et al. 2000), so we adopted 5 Myr as a limiting time in our chemical simulations. According to the *Spitzer* IRS observations (Calvet et al. 2005), the inner DM Tau disk is cleared of small dust ($\lesssim 3$ AU) and is in a pre-transitional phase already. Therefore, in the chemical simulations a disk region beyond 10 AU is considered, where dust grain evolution seems to be slow and grain growth is moderate (Birnstiel et al. 2010). In chemical modeling, the dust grains are assumed to be uniform $0.1 \mu\text{m}$ amorphous olivine particles (with density of $\rho_d = 3 \text{ g cm}^{-3}$). This is the size representing a mean radius in the dust size distribution. Equal gas and dust temperatures are assumed. Gas becomes hotter than dust only in an upper, tenuous and heavily irradiated disk layer, which often has negligible contribution to molecular column densities.

The turbulence in disks is likely driven by the magnetorotational instability (MRI), which is operative even in a weakly ionized medium, and is essentially a 3-D phenomenon (e.g., Balbus & Hawley 1991). This turbulence causes anomalous viscosity that enables efficient redistribution of the angular momentum and accretion of disk matter onto the star. However, inner disk midplane can be almost neutral and decoupled from magnetic fields, forming a region with reduced, inherited turbulence (“dead zone”), Gammie (see, e.g., 1996); Sano et al. (see, e.g., 2000); Semenov et al. (see, e.g., 2004); Wünsch et al. (see, e.g., 2006). With modern computational facilities coupled chemo-MHD 3-D models are only manageable for extremely limited chemical networks and a restricted disk domain (see, for example, Turner et al. 2007). We have followed the parametrization of Shakura & Sunyaev (1973), where turbulent viscosity ν is related to local disk properties such as the characteristic (vertical) spatial scale $H(r)$, the sound speed $c_s(r, z)$, and the dimensionless parameter α :

$$\nu(r, z) = \alpha c_s(r, z) H(r). \quad (1)$$

From observational constraints α is $\sim 0.001 - 0.1$ (Andrews & Williams 2007; Guilloteau et al. 2011), similar to values obtained from MHD modeling of the MRI (e.g., Dzyurkevich et al. 2010). However, the magnitude of MHD viscous stresses changes throughout the disk, and thus in this simplistic parametrization the α -parameter should also be variable. Unfortunately, without detailed MHD studies it is hard to characterize α , so we adopt the constant value of 0.01. Since only a disk region beyond 10 AU is studied, a “dead

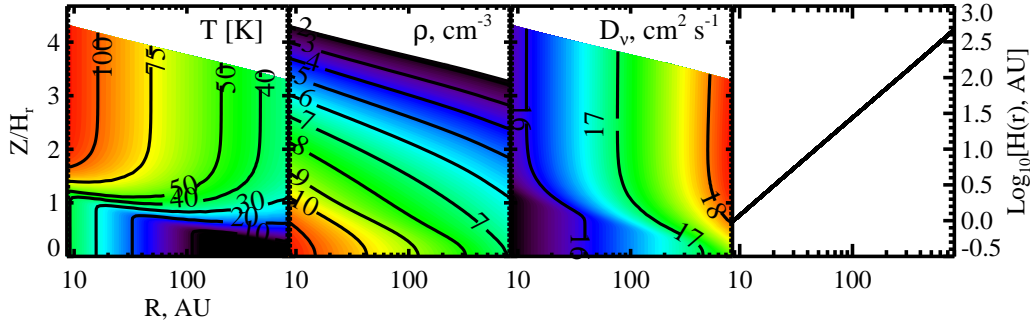


Figure 1. (Left to right) Distributions of the temperature, particle density (\log_{10} scale), diffusion coefficient in $\text{cm}^2 \text{s}^{-1}$ (\log_{10} scale), and pressure scale height in AU (\log_{10} scale) in the DM Tau disk model. In the first 3 panels the Y-axis is given in units of the pressure scale height.

zone” where effective α is very low, $\lesssim 10^{-4}$, is avoided.

Consequently, the diffusion coefficient is calculated as

$$D_{\text{turb}}(r, z) = \nu(r, z)/Sc, \quad (2)$$

where Sc is the Schmidt number describing efficiency of turbulent diffusivity (see e.g. Shakura & Sunyaev 1973; Schräpler & Henning 2004). In our simulations we assume that gas-phase species and dust grains are well mixed, and transported with the same diffusion coefficient. We treat diffusion of mantle materials similarly to gas-phase molecules, without relating it to individual grain dynamics. Hence two chemo-dynamical models are considered: (1) the high-efficiency mixing model with $Sc = 1$ and (2) the low-efficiency mixing model with $Sc = 100$. In the $Sc = 1$ model the diffusion coefficient in outer disk regions is $\sim 10^{18} \text{ cm}^2 \text{s}^{-1}$, similar to Willacy et al. (2006). The second model represents a hypothetical case when mixing of molecules occurs much slower than turbulent eddy turn-over speeds yet faster than in the pure laminar gas. The temperature and density structure, diffusion coefficient D_{turb} , and vertical pressure scale height $H(r)$ of the DM Tau-like disk model are shown in Fig. 1.

2.2. Chemical network

The adopted gas-grain chemical model is described in our recent papers on benchmarking of disk chemical models (Semenov et al. 2010b) and observations of CCH in DM Tau, LkCa 15, and MWC 480 (Henning et al. 2010). A brief summary is provided below. The chemical network is based on the osu.2007 ratefile with recent updates to reaction rates². (Note that in Paper I we used UMIST 95 ratefile.) A new class of X-ray-driven reactions leading to production of O^{++} , C^{++} , N^{++} , S^{++} , Fe^{++} , Si^{++} is added. Their neutralization reactions by electrons and charge transfer reactions with molecules are adopted from Stäuber et al. (2005). The photoionization cross sections are taken from Verner et al. (1993), as described in Maloney et al. (1996). Secondary electron impact ionization cross sections are taken from Meijerink & Spaans (2005).

To calculate UV ionization and dissociation rates, the mean FUV intensity at a given disk location is obtained by adding the stellar $\chi_*(r) = 410(r, \text{AU})/(100 \text{ AU})^2$ and interstellar χ_0 components that are scaled down by the visual extinction in the vertical direction and in the direction to the central star (1D plane-parallel approximation). Several tens of photoreaction rates are updated using the new calculations of van Dishoeck et al. (2006), which are publicly available³. The self-shielding of H_2 from photodissociation is calculated by

Eq. (37) from Draine & Bertoldi (1996). The shielding of CO by dust grains, H_2 , and its self-shielding is calculated using precomputed table of Lee et al. (1996, Table 11).

We model the attenuation of cosmic rays (CRP) by Eq. (3) from Semenov et al. (2004), using the standard CRP ionization rate $\zeta_{\text{CR}} = 1.3 \cdot 10^{-17} \text{ s}^{-1}$. Ionization due to the decay of short-living radionuclides is taken into account, $\zeta_{\text{RN}} = 6.5 \cdot 10^{-19} \text{ s}^{-1}$ (Finocchi et al. 1997). The stellar X-ray radiation is modeled using observational results of Glassgold et al. (2005) and the approximate expressions (7–9) from the 2D Monte Carlo simulations of Glassgold et al. (1997a,b). The typical X-ray photon energy is 3 keV, and the X-ray emitting source is located at 12 stellar radii above the midplane. The X-ray ionization rates exceed that of the CRPs in the disk regions above the midplane.

The gas-grain interactions include sticking of neutral species and electrons to uniformly-sized dust grains with 100% probability, release of frozen molecules by thermal, CRP-, and UV-induced desorption, dissociative recombination and radiative neutralization of ions on charged grains, and grain re-charging. We do not allow H_2 to stick to grains because the binding energy of H_2 to pure H_2 mantle is low, $\sim 100 \text{ K}$ (Lee 1972), and it freezes out in substantial quantities only at temperatures below $\approx 4 \text{ K}$. Chemisorption of surface molecules is not considered. We considered various UV photodesorption yields between 10^{-5} and 10^{-3} (e.g., Greenberg 1973; Öberg et al. 2009b,a) and found that in this range the exact yield value has a negligible impact on the modeling results. To allow synthesis of complex (organic) molecules, an extended list of surface reactions together with desorption energies and a list of photodissociation reactions of surface species is adopted from Garrod & Herbst (2006). Desorption energies for assorted molecules are listed in Table 1. We assume that each $0.1 \mu\text{m}$ spherical olivine grain provides $\approx 2 \cdot 10^6$ surface sites, and that surface recombination proceeds solely through the Langmuir-Hinshelwood formation mechanism. Upon a surface recombination, there is a 5% chance for the products to leave the grain. Following interpretations of experimental results on the formation of molecular hydrogen on dust grains (Katz et al. 1999), we employ the standard rate equation approach to the surface chemistry without H and H_2 tunneling either through the potential walls of the surface sites or through reaction barriers. As it has been shown by Vasyunin et al. (2009), when surface recombination rates are slow, the stochastic effects are of no importance for the surface chemistry.

Overall, the disk chemical network consists of 657 species made of 13 elements, and 7306 reactions. In contrast to the Paper I, we do not apply our “Automatic Reduction Tech-

² See: [http://www.physics.ohio-state.edu/\\$sim\\$eric/research/](http://www.physics.ohio-state.edu/simeric/research/)

³ <http://www.strw.leidenuniv.nl/~ewine/photo/>

Table 1
Desorption energies

Species	Energy, K
C	800
C ₂	1600
C ₂ H	2140
C ₂ H ₂	2590
C ₂ S	2700
C ₃	2400
C ₃ H ₂	3390
C ₆ H ₆	7590
C ₈ H ₂	7390
CH ₂ OH	5080
CH ₂ CO	2200
CH ₃ CHO	2870
CH ₃ OH	5530
CH ₄	1300
CN	1600
CO	1150
CO ₂	2580
CS	1900
H	624
H ₂	552
H ₂ S	2740
H ₂ CO	2050
H ₂ CS	2700
H ₂ O	5700
HCN	2050
HCOOH	5570
HNC	2050
HNCO	2850
HNO	2050
N	800
N ₂	1000
NH	2380
NH ₂	3960
NH ₃	5530
NO	1600
O	800
O ₂	1000
O-CN	2400
OH	2850
S	1100
SO	2600
SO ₂	3400

nique” (ART) to reduce the size of this network (thanks to increased performance of our chemo-dynamical code). The “low metals” initial abundances of Lee et al. (1998a) are utilized (Table 2). The choice of initial abundances does not affect the resulting molecular abundances and column densities due to relatively high densities in and long evolutionary timescales of protoplanetary disks, which essentially reset a chemical “clock” (e.g., Willacy et al. 2006).

2.3. Modeling chemistry with transport

The disk physical structure and the chemical model described above are used to solve chemical kinetics equations together with turbulent transport terms. Since a while such kind of models have been employed in atmospheric chemistry, planetary atmosphere chemistry, and chemistry of molecular clouds (e.g., Garcia & Solomon 1983; Xie et al. 1995; Yate & Millar 2003). We utilize the mixing approach of Xie et al. (1995), which is based on the Fickian’s diffusion laws:

$$\frac{dn_i}{dt}(r,z) = F_i(r,z) - L_i(r,z) - \nabla \cdot \left(D_{\text{turb}}(r,z) n_H(r,z) \nabla \frac{n_i(r,z)}{n_H(r,z)} \right). \quad (3)$$

Table 2
Initial abundances

Species	Relative abundance
H ₂	0.499
H	2.00(-3)
He	9.75(-2)
C	7.86(-5)
N	2.47(-5)
O	1.80(-4)
S	9.14(-8)
Si	9.74(-9)
Na	2.25(-9)
Mg	1.09(-8)
Fe	2.74(-9)
P	2.16(-10)
Cl	1.00(-9)

Table 3
Characteristic Timescales: Inner Disk (10 AU)

Processes	Midplane [yr]	Warm layer* [yr]	Atmosphere* [yr]
Mixing	3.4 (3)	3.4 (3)	1.3 (3)
Gas-phase	1.4 (-5)	1.3 (-4)	1.0 (-2)
UV	>1.0 (7)	3.3 (4)	5.9 (2)
Accretion	1.2 (-2)	1.1 (-1)	5.4 (0)
Desorption	5.8 (-7)	6.0 (-7)	<1.0 (-7)
Surface	>1.0 (7)	>1.0 (7)	<1.0 (-7)

* The warm layer and atmosphere are located at the $z/H_r = 0.8$ and 1.75, respectively.

Table 4
Characteristic Timescales: Outer Disk (250 AU)

Processes	Midplane [yr]	Warm layer* [yr]	Atmosphere* [yr]
Mixing	1.0 (6)	2.5 (5)	1.4 (5)
Gas-phase	2.0 (-2)	1.8 (-1)	2.9 (0)
UV	>1.0 (7)	1.2 (6)	3.1 (1)
Accretion	2.7 (1)	1.8 (2)	2.3 (3)
Desorption	1.0 (6)	4.3 (0)	<1.0 (-7)
Surface	>1.0 (7)	>1.0 (7)	1.4 (5)

* The warm layer and atmosphere are located at the $z/H_r = 0.8$ and 1.75, respectively.

Here n_i is concentrations of the i -th species (cm^{-3}), F_i and L_i are formation and destruction (loss) terms. In the following we will use relative abundances for considered species $X_i = n_i/n_H$ where n_H is the total hydrogen nucleus number density. In this formalism the turbulence mixing rate for a certain species depends on its chemical gradient.

The formation and destruction of molecules are governed by the chemical kinetics:

$$\frac{dn_i}{dt} = \sum_{l,m} k_{lm} n_l n_m - n_i \sum_{i \neq l} k_l n_l + k_i^{\text{des}} n_i^s - k_i^{\text{acc}} n_i \quad (4)$$

$$\frac{dn_i^s}{dt} = \sum_{l,m} k_{lm}^s n_l^s n_m^s - n_i^s \sum_{i \neq l} k_l^s n_l^s - k_i^{\text{des}} n_i^s + k_i^{\text{acc}} n_i \quad (5)$$

where n_i^s is the surface concentration of the i -th species

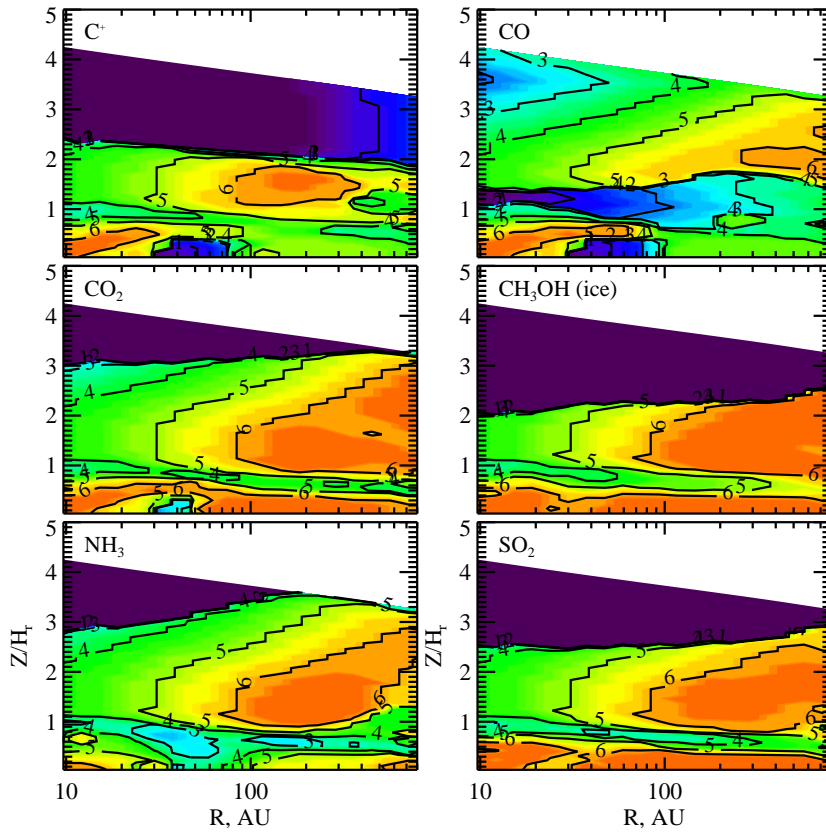


Figure 2. (Top to bottom) Distributions of timescales to reach a chemical steady-state during the 5 Myr of evolution for C^+ , CO , CO_2 , CH_3OH ice, NH_3 , and SO_2 . For relative abundances below 10^{-25} this timescale is assumed to be 1 year.

(cm^{-3}), k_{lm} and k_l are the gas-phase reaction rates (in units of s^{-1} for the first-order kinetics and $\text{cm}^3 \text{s}^{-1}$ for the second-order kinetics), k_i^{acc} and k_i^{des} denote the accretion and desorption rates (s^{-1}), and k_{lm}^s and k_l^s are surface reaction rates ($\text{cm}^3 \text{s}^{-1}$).

The stiff equations of chemical kinetics are integrated simultaneously with the diffusion terms in the Eulerian description, using a fully implicit 2D integration scheme. As boundary conditions for mixing, we assume that there is no inward and outward diffusion across boundaries of the disk domain, and that there is no flux through the midplane. We do not employ approximate, operator-splitting integration schemes, in which transport and chemical processes are treated separately, and instead integrate PDE system directly. Our “ALCHEMIC” FORTRAN77 code (Semenov et al. 2010b) is based on the Double-precision Variable-coefficient Ordinary Differential equation solver with the Preconditioned Krylov (DVODPK) method GMRES for the solution of linear systems⁴. The approximate Jacobi matrix is generated automatically from the supplied chemical network (without transport terms) and serves as a lefthand preconditioner. For astrochemical models dominated by hydrogen reactions the Jacobi matrix is sparse, with $\lesssim 1\%$ of non-zero elements. The corresponding linearized system of algebraic equations is solved using a high-performance sparse unsymmetric MA48 solver from the Harwell Mathematical Software Library⁵. All the equations are solved on a non-uniform staggered grid consisting of 41 radial points (from 10 to 800 AU) and 91 verti-

cal points. This resolution is found to be optimal for mixing problems in a protoplanetary accretion disk, keeping the computation tractable and still providing enough accuracy for the analysis. With a typical 10^{-6} relative and 10^{-15} absolute errors, the 2D-mixing model with high mixing efficiency has about 15 million non-zero Jacobi matrix elements and takes about 48 hours of CPU time (Xeon 3.0 GHz, 4 Gb RAM, gfortran 4.4-x64) to calculate the disk chemical structure within 5 Myr.

Our main set of chemical simulations consists of three runs: (1) the laminar disk chemical model (no transport processes are taken into account), (2) the fast 2D-mixing model ($Sc = 1$), and (3) the slow 2D-mixing transport model ($Sc = 100$). The chemical evolutionary time span is 5 Myr.

3. WHEN TURBULENCE AFFECTS DISK CHEMISTRY

Before drilling into complex numerics, it is reasonable to analyze general conditions at which turbulent diffusion may affect the chemical evolution in a protoplanetary disk.

3.1. Chemical and dynamical timescales

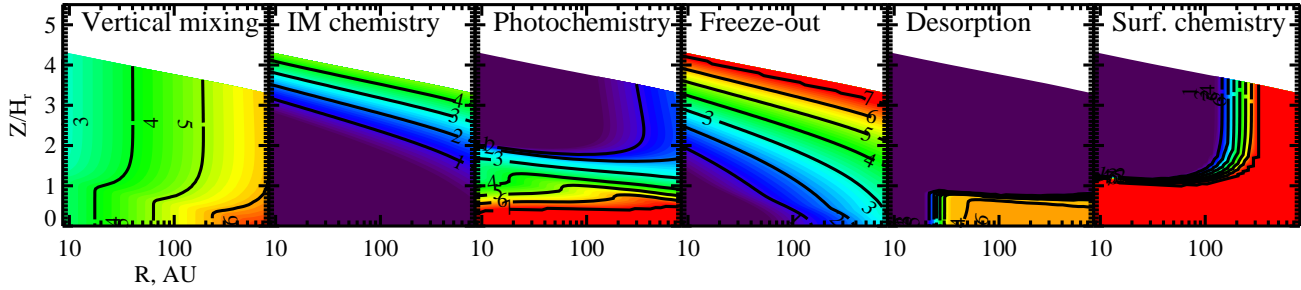
In computational fluid dynamics with reacting flows Damköhler number Da is often used as a measure of the influence of dynamical processes on the chemical evolution. This number is simply the ratio of a physical timescale to a chemical timescale:

$$Da = \tau_{\text{phys}} / \tau_{\text{chem}}. \quad (6)$$

When $Da \lesssim 1$, chemical evolution of a molecule is slow and therefore may be sensitive to changes in physical conditions due to the medium flow. In contrast, when $Da \gg 1$, chemical evolution is fast and is not affected by transport processes.

⁴ <http://www.netlib.org/ode/vodpk.f>

⁵ <http://www.hsl.rl.ac.uk/>



$$k_{\text{des}}^{\text{CRP}} = 2.4 \cdot 10^{-2} \zeta_{\text{CRP}} \nu_0 \exp^{-\gamma/T_{\text{CRP}}}, \quad (13)$$

and

$$k_{\text{des}}^{\text{th}} = \nu_0 \exp^{-\gamma/T}. \quad (14)$$

Here, $T_{\text{CRP}} = (4.36 \cdot 10^5 + T^3)^{1/3}$ is a peak grain temperature (K) reached upon a hit by relativistic iron nucleus (see Eq. 6 in Semenov et al. 2004), ν_0 is characteristic vibrational frequency (s^{-1}) of a molecule, and γ its desorption energy (K). In Fig. 3 (5th panel) we show distribution of the evaporation timescale for CO in the DM Tau disk model. In cold and dark outer midplane, where temperatures are below ≈ 20 K, desorption of CO is too slow, and τ_{des} exceeds about 1 Myr, whereas in upper disk layer and in the warm planet-forming zone desorption is a rapid process.

Finally, surface chemistry timescale in the absence of tunneling is controlled by thermal hopping rates of the reactants, and the reaction barrier (see Eqs. 12, 14 in Semenov et al. 2010b). As an example, we consider a slow first step in surface hydrogenation sequence of CO into CH_3OH , namely, $\text{H}(\text{ice}) + \text{CO}(\text{ice}) \rightarrow \text{HCO}(\text{ice})$, which has a barrier of about 2500 K caused by bond restructuring. In Fig. 3 (last panel) the timescale of the CO surface chemistry is presented. As can be clearly seen, surface chemistry has a long timescale of $\sim 10^6$ years around midplane and in cold outer disk region, which is similar to the turbulent mixing timescale. Therefore, chemical species produced mainly via surface processes (e.g., ices and complex organics) shall be sensitive to turbulent diffusion mixing in disks. The aforementioned characteristic timescales in the inner (10 AU) and outer (250 AU) disk regions are also compared in Tables 3-4.

In reality chemical evolution of a large multi-component mixture is controlled by both fast and slow processes, so it is hard to obtain a single characteristic evolutionary timescale as discussed above. Usually detailed analysis of eigenvalues and eigenvectors of Jacobi matrix or its diagonal and off-diagonal terms is used to isolate fast and slow evolving subsystems in the chemical network (e.g., Lovrics et al. 2006). However, for a tightly coupled, extended set of chemical reactions, like a typical hydrogen- and carbon-dominated astrochemical network, such an analysis is hard to perform. We elaborate a different approach and use the results of our non-mixing disk model to derive individual chemical timescales as the time needed to reach a chemical quasi steady-state for a given species. The steady-state time is the evolutionary moment when molecular abundances in the subsequent time-steps change by a factor of $\lesssim 3$ or assumed 5 Myr otherwise. In Fig. 2 the chemical steady-state times for a few assorted species in the DM Tau disk model are presented.

The steady-state timescale distributions exhibit a complex pattern that is not easily related to characteristic chemical timescales shown in Fig. 3. Noteworthy, this pattern is similar for many species in the network, with slow surface processes, $\tau_{\text{chem}} \sim 10^5 - 10^6$ years, determining the chemical timescales in the midplane, $z/H_r \lesssim 0.8$ (here H_r is the pressure scale height). In the warm inner midplane, $r \lesssim 20$ AU, the characteristic chemical timescales are large because not only H and H_2 but also heavy radicals become mobile at $T \sim 30 - 40$ K, leading to active surface chemistry (see, e.g., Garrod et al. 2008). Within $\sim 30 - 50$ AU temperatures in the midplane are between 15–25 K, and hydrogen evaporates too rapidly, while other radicals are too heavy to activate surface chemistry. This results in a dearth of rapid surface reactions. Therefore, chemical timescales are usually shorter,

$\tau_{\text{chem}} \sim 10^4 - 10^5$ years, in this region, and are governed by gas-grain interaction rates. Above the cold and dark midplane, at ≈ 1 pressure scale height, where a warm molecular layer is located, the characteristic chemical timescales are shorter, $\lesssim 10^5$ years, since thermal desorption and photodesorption start to prevail there over surface chemistry and accretion. Within the inner ~ 200 AU of the molecular layer lukewarm temperatures and elevated X-ray ionization enable slow photodestruction of well-bound ices. In the upper disk region, $\gtrsim 1.5$ pressure scale height, where molecules are effectively destroyed by high-energy UV and X-ray photons, photochemistry coupled to slow neutral-neutral reactions set chemical timescales that increase outward from $\sim 10^4$ years till $\gtrsim 1$ Myr. The outward decrease of the gas density in this region makes recombination rates slower (as these scale down as density squared), whereas the stellar UV and X-ray fluxes also decrease with the radial distance from the star. Note that chemical timescales are shorter in the CO molecular layer and, in particular, for C^+ , which is abundant in the disk atmosphere at $z/H_r \lesssim 1.8 - 2$, while τ_{chem} is long and comparable to the dynamical timescales in regions where CO_2 , CH_3OH ice, and SO_2 are produced (see Fig. 2). As we shall see later, indeed chemical evolution of these (and many others) species is affected by the turbulent diffusion.

3.2. Mixing Importance Measure

Considerations presented in the previous subsection provide some clues on the mixing sensitivity for various species. However, it would be instructive to find some general quantitative measure of this sensitivity. We suggest a new Mixing Importance Measure (MIM) to find necessary conditions for sensitivity of column densities of a given molecule to the turbulent mixing, based on results of the laminar model. This quantity comes in three varieties, namely, a local value

$$\text{MIM}_{r,z} = \frac{1}{Da(r,z)} \frac{n(r,z)}{N(r)}, \quad (15)$$

a vertically integrated value

$$\text{MIM}_r = \int_0^{z_{\text{max}}(r)} \text{MIM}_{r,z} dz, \quad (16)$$

and a global value

$$\text{MIM} = \frac{1}{(r_1 - r_0)} \int_{r_0}^{r_1} \text{MIM}_r dr, \quad (17)$$

where $Da(r,z)$ is the Damköhler number (Eq. 6), $N(r)$ is the total vertical column density (cm^{-2}) of a given species at the radius r , $n(r,z)$ (cm^{-3}) is its number density at the disk location (r,z) , $z_{\text{max}}(r)$ is the disk height at the radius r , and r_0 , r_1 are the disk inner and outer radii, respectively. The characteristic physical timescale is the diffusion timescale given by Eq. 7, and the characteristic chemical timescale of a molecule is its quasi steady-state timescale defined above (see Fig. 2). By definition, the MIM for a molecule allows localizing those disk regions where the chemical evolution is slow and which contribute most to the vertical column density (a typical observationally inferred quantity). Thus, the larger the MIM, the stronger possible changes in vertical column densities of a considered species due to turbulent transport. However, the straightforward expression (15) is not a sufficient criterion for making reliable estimates on a magnitude of such changes. For example, in the absence of relative abundance gradients

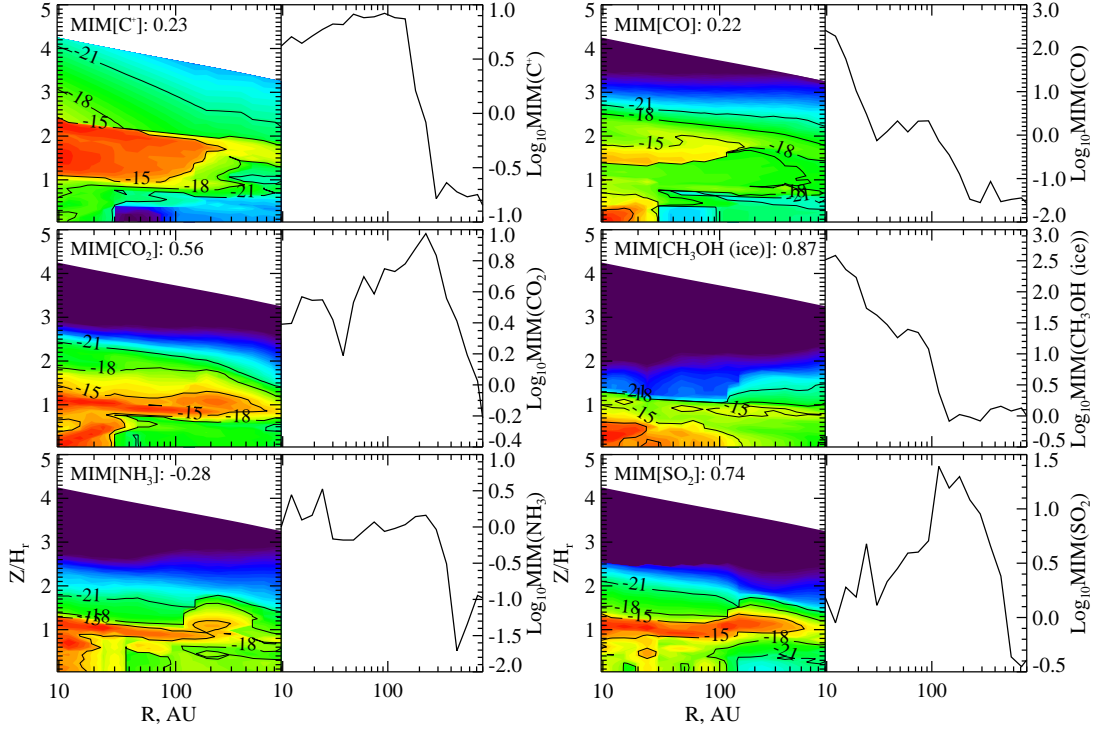


Figure 4. (Top to bottom) Distributions of the Mixing Importance Measure (MIM; left panel) and vertically-integrated MIM (right panel) for C^+ , CO, CO_2 , CH_3OH ice, NH_3 , and SO_2 . The higher the MIM, the more sensitive can be the chemical evolution of the given molecule to dynamical processes. Also given are globally integrated MIM values.

even very slow chemistry (resulting in large MIM) leads to the same column densities as the non-mixing (laminar) disk model. On the other hand, if MIM is small everywhere in the disk, the mixing will not alter resulting column densities. The local (Eq. 15), vertically-integrated (Eq. 16), and disk-averaged (Eq. 17) MIMs for several species are shown in Fig. 4 (\log_{10} scale).

The MIM distribution for C^+ peaks at elevated disk heights, $\sim 1 - 2H_r$, where the C^+ concentration is high, and photochemistry is relatively slow yet efficient, especially on ices (cf. Fig. 3). The importance of turbulent mixing to its chemical evolution is low ($\lg(MIM) = 0.23$) compared to the other species, particularly, in outer disk region at $r \gtrsim 300$ AU. Two other species with similarly low global MIM values of $\lg(MIM) = 0.22$ and $\lg(MIM) = -0.28$ are CO and NH_3 , respectively. The MIM distribution for CO has a distinct peak around inner disk midplane at $r \lesssim 30$ AU, where temperatures are appropriate to its surface conversion to CO_2 , and where the gas-phase CO concentration is high. Another region where the CO chemistry may be affected by the turbulent processes is located at the upper CO molecular layer, at $\sim 2H_r$, in the inner disk zone. There the UV photodissociation of CO is slow due to self-shielding and mutual-shielding by H_2 and dust, and X-ray ionization of He leads to slow destruction of CO by He^+ at late times, $t \sim 10^5 - 10^6$ years.

In contrast to CO and C^+ , the MIM for the CO_2 , NH_3 , and SO_2 chemistry exhibit a somewhat similar pattern (Fig. 4). The most likely dynamically-sensitive regions are the warm molecular layer, where photoprocessing is activated, and inner part of the disk midplane, where surface heavy C-, O- and N-bearing radicals become mobile. This is also probably true for S-bearing radicals as well, but our surface network includes only a very limited sulfur chemistry, therefore the MIM for SO_2 does not reach its maximum in the inner midplane,

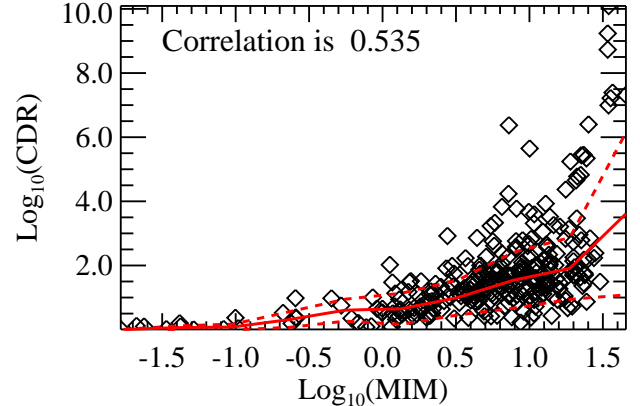


Figure 5. Dependence of the ratio of the molecular column densities integrated over the disk radius and computed with the 2D-mixing and laminar models ($t = 5$ Myr) versus MIM. Shown are the molecules with the maximum column densities in the laminar case that exceed 10^{11} cm^{-2} . The corresponding linear correlation coefficient is also shown (top left corner).

and peaks within the SO_2 molecular layer. Finally, the MIM for CH_3OH ice is the largest in the disk midplane where solid methanol is produced by surface hydrogenation of CO and by CH_3 reacting with OH. The disk-averaged MIM values are relatively high for CO_2 ($\lg(MIM) = 0.56$) and especially for SO_2 ($\lg(MIM) = 0.74$) and solid CH_3OH ($\lg(MIM) = 0.87$). Below we will reveal that their column densities are enhanced by the turbulent diffusion by more than an order of magnitude, unlike those of C^+ , CO, and NH_3 .

4. RESULTS OF NUMERICAL MODELING

Table 5
Species steadfast to turbulent mixing

Molecule*	$\lg(Se)$	$\lg(CDR)$	$\lg(N_{\text{stat}}^{\max})$
C^+	0.23	0.48	16.79
C_2	0.25	0.68	14.41
C_2H	0.40	0.64	14.29
C_2H_2^+	0.67	0.68	12.36
CH	0.30	0.37	12.91
CH_2	0.33	0.45	12.73
CH_3^+	0.69	0.57	12.22
CH_5^+	0.34	0.66	13.48
CL	-0.17	0.21	13.95
CN	0.12	0.56	14.41
CO	0.22	0.43	18.67
Fe	0.31	0.45	11.31
Fe^+	-0.62	0.19	13.69
FeH	0.22	0.68	12.16
grain(0)	-0.21	0.35	12.29
H_2	-1.08	0.02	24.30
H_2CN^+	0.13	0.49	13.06
H_2CO	0.32	0.44	13.91
H_2CO^+	0.78	0.44	11.23
H_2S	0.11	0.44	13.23
H_3^+	-0.68	0.52	14.81
H_3CO^+	0.58	0.37	11.62
H_3O^+	0.12	0.64	13.43
HCN	-0.00	0.65	14.50
HCS	0.27	0.61	11.28
He^+	0.07	0.51	15.07
HNC	-0.04	0.66	14.24
Mg	-1.67	0.12	12.06
Mg^+	-1.38	0.10	13.91
MgH_2	-1.38	0.20	13.27
N_2	0.19	0.43	17.61
Na	-1.62	0.10	11.84
NH_2	-0.59	0.35	14.18
NH_4^+	-0.00	0.53	12.17
OH	0.09	0.32	14.92
Si	0.69	0.42	13.06
SiH	0.49	0.35	11.21
SiH_3	-0.59	0.38	11.05
C ice	1.03	0.50	16.00
$\text{C}_2\text{H}_2 \text{ ice}$	0.18	0.62	13.91
$\text{CH}_3\text{N ice}$	1.26	0.67	15.54
FeH ice	-1.47	0.02	16.04
H ice	-1.00	0.37	18.55
$\text{H}_2 \text{ ice}$	1.15	0.43	17.08
$\text{H}_2\text{CS ice}$	0.34	0.52	16.29
$\text{H}_2\text{O ice}$	0.06	0.09	20.84
$\text{H}_2\text{S ice}$	-0.98	0.05	17.54
HCN ice	0.27	0.65	19.43
HCSi ice	-0.00	0.54	12.50
HS ice	1.01	0.38	15.54
$\text{MgH}_2 \text{ ice}$	-1.29	0.01	16.64
NaH ice	-1.78	0.01	15.96
$\text{NH}_3 \text{ ice}$	-0.08	0.11	19.84
S ice	0.96	0.57	15.50
$\text{S}_2 \text{ ice}$	0.74	0.42	11.45
SiC ice	0.88	0.39	13.85
$\text{SiCH}_2 \text{ ice}$	0.94	0.23	12.95
$\text{SiH}_4 \text{ ice}$	-0.11	0.08	16.59

Note. — Col.2 The Mixing Importance Measure (MIM) integrated over the disk (in log scale). Col.3 The ratio of the vertical column density at $t = 5$ Myr computed with the 2D-mixing and the laminar chemical models, averaged over the radius (in log scale). Col.4 The maximal vertical column density for a given molecule at 5 Myr in the laminar model.

* Listed are the molecules which vertical column densities in the disk exceed 10^{11} cm^{-2} .

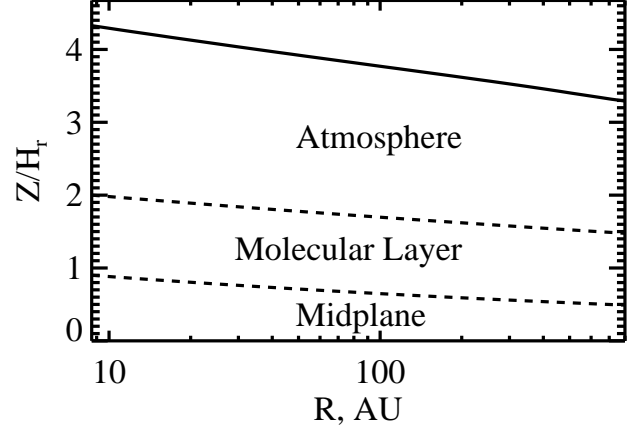


Figure 6. Major disk regions are designated by analyzing the distribution patterns of the C^+ and CO abundances. The atmosphere is the disk region dominated by C^+ in contrast to CO , whereas in the molecular layer carbon is mainly locked in the CO gas-phase molecules. The midplane is the disk region where depletion of gas-phase molecules occurs.

Table 6
Species sensitive to turbulent mixing

Molecule*	$\lg(Se)$	$\lg(CDR)$	$\lg(N_{\text{stat}}^{\max})$
C	0.79	1.80	17.89
C_2H_2	-0.07	1.01	14.35
C_2H_3^+	0.35	1.18	11.43
C_2H_4	0.93	1.75	11.82
C_2N	0.76	1.83	12.53
C_3	0.52	1.12	14.93
C_3H	0.64	1.18	13.42
C_3H^+	0.74	0.91	12.38
C_3H_2	0.60	1.24	13.95
C_3H_2^+	0.59	1.11	12.05
C_3H_3^+	0.86	1.04	11.83
C_3N	0.86	1.40	12.01
C_3O	0.96	1.25	11.17
C_4	0.73	1.17	13.13
C_4H	0.56	1.11	13.74
C_4H_2	0.32	1.09	13.89
C_4H_3	0.56	1.30	13.81
C_4H_3^+	0.59	1.13	11.81
C_4H_4	1.04	1.61	12.15
C_4H_4^+	0.86	0.84	11.59
C_4N	0.84	1.41	12.71
C_5	0.55	1.21	14.18
C_5H	0.72	1.40	12.98
C_5H^+	0.96	1.06	11.15
C_5H_2	0.69	1.23	13.29
C_5H_2^+	1.10	1.62	11.07
$\text{C}_5\text{H}_2\text{N}^+$	1.14	1.48	11.19
C_5N	0.81	1.63	12.39
C_6	0.62	1.51	13.85
C_6H	0.95	1.59	12.71
C_6H_2	0.91	1.07	13.25
C_6H_2^+	1.14	1.84	11.10
C_6H_6	1.18	1.59	11.39
C_7	0.74	1.39	13.44
C_7H	1.12	1.37	12.22
C_7H_2	1.08	1.31	12.36
C_8	1.03	1.47	13.41
C_8H	1.11	1.30	12.31
C_8H_2	1.02	0.96	12.93
C_9	1.09	1.41	13.33
C_9H	1.09	1.11	11.99
C_9H_2	1.11	1.46	12.49
C_9N	1.13	1.98	11.05
CH_2CN	0.75	1.12	11.80
CH_2CO	1.05	1.78	11.29
CH_2NH	0.53	1.05	11.56
CH_3	-0.35	0.98	15.34
CH_3CN	0.76	1.04	11.33
CH_4	0.60	0.91	17.69

Table 6 — Continued

Molecule*	$\lg(Se)$	$\lg(CDR)$	$\lg(N_{\text{stat}}^{\max})$
CH_5N	0.68	1.07	11.50
CNC^+	0.33	1.20	11.38
CS	0.43	1.91	12.15
e^-	0.42	0.89	17.25
H	0.93	1.81	22.69
H^+	0.88	1.66	17.07
H_2CS	0.28	0.93	12.33
H_2NO^+	0.19	1.52	11.20
H_2O	0.37	0.95	15.52
H_2S_2	0.98	1.67	11.21
H_2SiO	0.65	1.68	11.31
HC_3N	1.03	1.17	11.97
HC_5N	1.12	1.56	12.15
HCCN	0.82	1.52	11.25
HCL	0.83	1.62	11.16
HCO	0.66	1.25	11.28
HCO^+	0.48	1.35	13.98
HNCO	0.95	1.96	12.14
HNO	0.18	1.48	13.67
HNSi	0.47	1.99	11.29
HS	0.79	1.37	11.60
HS_2	0.97	1.67	11.21
N	0.52	0.84	17.78
N_2H^+	0.47	1.47	12.39
NH	0.09	1.13	13.36
NH_2CN	0.62	1.07	12.40
NH_3	-0.28	0.75	14.74
NH_3^+	0.34	0.89	11.43
NO	0.36	1.43	14.57
NO^+	0.66	0.89	11.23
O	0.08	0.73	18.65
O^+	0.80	1.52	12.24
O_2	0.58	1.98	16.91
O_2^+	0.86	1.10	13.41
OCN	0.18	1.18	13.69
OCS	0.49	1.75	11.98
P	0.26	0.73	12.53
P^+	0.73	1.56	12.89
S	0.60	1.23	14.73
S^+	0.68	1.13	15.52
Si^+	0.69	1.25	14.12
SiH_4	0.32	0.87	12.07
SO^+	0.59	1.11	12.00
C_{10} ice	1.04	1.19	15.00
C_2 ice	0.96	1.91	15.28
C_2H ice	0.94	1.91	15.22
C_2H_3 ice	1.34	1.89	12.79
C_3 ice	0.96	1.80	15.81
C_3H ice	0.78	1.77	16.39
C_3H_2 ice	0.70	1.29	19.66
C_3S ice	0.92	1.51	15.12
C_4 ice	1.30	1.70	12.84
C_4H ice	1.30	1.86	13.18
C_4H_2 ice	0.84	1.74	14.43
C_4H_3 ice	1.28	1.85	12.74
C_4H_4 ice	0.79	1.89	18.06
C_4N ice	0.67	1.75	14.78
C_4S ice	1.16	1.01	12.84
C_5H_2 ice	0.77	1.54	18.73
C_6H_2 ice	0.61	1.34	18.59
C_6H_6 ice	1.06	1.99	13.81
C_7H_2 ice	0.67	1.62	17.95
C_8H_2 ice	0.70	1.82	18.44
C_9H_2 ice	0.58	1.04	18.06
CCL ice	1.06	0.98	11.76
CH ice	0.93	1.20	16.16
CH_2 ice	0.79	1.37	17.73
CH_2CO ice	1.36	1.37	15.26
CH_2NH ice	1.37	1.45	13.37
CH_2NH_2 ice	1.37	1.76	12.95
CH_3 ice	0.40	1.34	17.77
CH_3CN ice	0.71	1.78	14.65
CH_3NH ice	1.38	1.70	12.95
CH_3OH ice	0.87	1.70	16.08
CH_4 ice	0.26	1.51	19.95
CL ice	0.63	0.88	15.20

Table 6 — Continued

Molecule*	$\lg(Se)$	$\lg(CDR)$	$\lg(N_{\text{stat}}^{\max})$
CN ice	0.58	1.00	15.53
CO ice	0.92	0.85	19.51
CS ice	0.66	1.87	14.93
H_2CN ice	1.33	1.71	13.25
H_2CO ice	1.03	0.93	16.73
H_2S_2 ice	0.63	1.16	12.84
H_2SiO ice	1.20	1.46	12.60
HC_2NC ice	0.93	1.47	12.99
HC_3N ice	1.31	1.95	15.57
HC_5N ice	0.71	1.47	14.82
HC_7N ice	0.99	0.94	14.49
HC_9N ice	1.04	0.72	14.42
HCS ice	1.29	0.72	11.06
HNC ice	0.60	1.41	18.32
HNCO ice	0.24	1.10	14.80
HNSi ice	0.81	1.14	12.52
HS_2 ice	0.64	1.17	12.84
N ice	1.20	1.27	16.13
N_2O ice	1.30	1.70	14.13
NaOH ice	1.39	0.87	11.13
NH ice	0.46	1.01	17.17
NH_2 ice	0.07	1.47	17.59
NH_2CHO ice	1.12	1.44	13.23
NH_2CN ice	0.45	1.26	13.54
NO ice	1.04	1.56	15.55
O ice	1.04	1.53	16.49
OCN ice	1.35	1.63	12.55
OH ice	-0.59	0.98	18.05
P ice	0.11	0.94	14.65
PH ice	1.02	1.93	13.69
PH_2 ice	0.86	1.65	13.75
Si ice	1.48	1.49	12.29
SiC_2 ice	1.25	0.91	12.76
SiC_2H ice	1.19	0.93	12.22
SiH_2 ice	1.24	1.57	14.06
SiH_3 ice	1.24	1.05	14.03
SiN ice	0.83	0.74	13.40
SiO ice	1.28	0.78	14.99
SO ice	0.72	1.72	14.86

Note. — Col.2 The Mixing Importance Measure (MIM) integrated over the disk (in log scale). Col.3 The ratio of the vertical column density at $t = 5$ Myr computed with the 2D-mixing and the laminar chemical models, averaged over the radius (in log scale). Col.4 The maximal vertical column density for a given molecule at 5 Myr in the laminar model.

* Listed are the molecules which vertical column densities in the disk exceed 10^{11} cm^{-2} .

Table 7
Species hypersensitive to turbulent mixing

Molecule*	$\lg(Se)$	$\lg(CDR)$	$\lg(N_{\text{stat}}^{\max})$
C_{10}	1.18	2.01	12.09
C_2S	0.71	2.27	11.80
C_3H_3	1.12	2.64	11.39
C_3H_4	1.03	3.31	11.89
C_3S	1.00	2.31	11.35
C_7N	1.12	2.57	11.58
$\text{CH}_3\text{C}_4\text{H}$	1.10	2.18	11.21
CO_2	0.56	2.23	14.94
H_2O^+	0.95	2.09	12.53
H_2O_2	0.91	2.53	13.54
HC_7N	1.13	2.34	11.34
HCOOH	0.81	2.07	12.36
HSiO^+	0.75	2.75	11.38
N^+	0.67	2.00	11.51
N_2O	0.44	2.92	12.30
NO_2	0.85	2.26	12.06
O_3	0.05	2.02	15.06
OH^+	1.00	2.68	12.86
SiO	0.76	3.33	13.17
SO	0.74	3.23	13.33
SO_2	0.81	3.83	12.45

Table 7 — *Continued*

Molecule*	$\lg(Se)$	$\lg(CDR)$	$\lg(N_{\text{stat}}^{\max})$
C ₂ H ₄ ice	0.99	2.61	16.71
C ₂ H ₆ ice	0.86	6.37	18.21
C ₂ S ice	0.95	2.79	12.86
C ₃ H ₃ N ice	1.14	2.04	11.92
C ₃ H ₄ ice	1.00	5.65	19.05
C ₅ ice	1.28	5.24	12.63
C ₅ H ice	1.00	3.67	13.38
C ₅ H ₄ ice	1.57	7.39	14.81
C ₆ ice	1.33	4.78	12.51
C ₆ H ice	0.91	3.77	13.08
C ₆ H ₄ ice	1.10	2.21	14.51
C ₇ ice	1.39	5.34	12.22
C ₇ H ice	1.11	3.93	12.65
C ₇ H ₄ ice	1.53	8.73	13.81
C ₈ ice	1.32	4.65	12.72
C ₈ H ice	1.01	2.83	13.24
C ₈ H ₄ ice	1.53	9.24	14.19
C ₉ ice	1.35	4.83	12.79
C ₉ H ice	1.14	3.52	13.60
C ₉ H ₄ ice	1.54	10.09	13.83
CCP ice	1.30	2.74	11.47
CH ₂ PH ice	1.54	6.99	12.26
CH ₃ C ₃ N ice	1.37	2.18	13.23
CH ₃ C ₄ H ice	1.04	2.01	14.79
CH ₃ C ₆ H ice	1.14	2.13	13.66
CH ₃ CHO ice	1.17	3.26	13.15
CO ₂ ice	1.03	3.60	19.62
CP ice	1.12	2.66	14.68
Fe ice	1.27	3.14	13.35
H ₂ C ₃ O ice	1.34	2.96	15.94
H ₂ O ₂ ice	1.40	2.20	16.97
H ₅ C ₃ N ice	1.55	7.22	13.16
HCCP ice	1.41	2.85	11.08
HCL ice	0.64	2.86	15.60
HCOOH ice	1.32	3.47	16.71
HCP ice	1.21	3.21	14.22
HNC ₃ ice	0.91	2.76	11.09
HNO ice	0.81	2.38	17.90
HPO ice	1.37	5.45	13.28
Mg ice	1.66	7.32	12.74
MgH ice	1.25	4.37	14.39
N ₂ ice	0.86	4.24	18.37
N ₂ H ₂ ice	0.76	2.62	16.65
Na ice	1.35	5.44	12.99
NO ₂ ice	1.25	2.84	13.20
NS ice	1.19	2.37	14.27
O ₂ ice	0.99	2.25	17.31
O ₂ H ice	1.35	2.79	11.28
O ₃ ice	0.91	2.58	18.07
PN ice	1.30	2.25	13.69
PO ice	1.09	3.05	14.17
SiH ice	1.44	2.24	12.99
SiS ice	1.30	2.14	11.63
C ₃ H ₃ ice	1.40	6.40	11.31

*

Note. — Col.2 The Mixing Importance Measure (MIM) integrated over the disk (in log scale). Col.3 The ratio of the vertical column density at $t = 5$ Myr computed with the 2D-mixing and the laminar chemical models, averaged over the radius (in log scale). Col.4 The maximal vertical column density for a given molecule at 5 Myr in the laminar model.

* Listed are the molecules which vertical column densities in the disk exceed 10^{11} cm^{-2} .

As we have already mentioned, we present results for three models. In the laminar model no diffusion is taken into account. In the fast diffusion model $Sc = 1$ is assumed, while in the slow diffusion model we use $Sc = 100$. In Fig. 5 the disk-averaged MIMs (Eqs. 15–17) are plotted versus the Column Density Ratios (CDRs) for fast mixing and laminar cases and for all species potentially observable with ALMA (with maximum column densities above 10^{11} cm^{-2}). The CDR is defined as:

$$\lg(CDR) = \max(|\lg(N_{2D}(r)) - \lg(N_{\text{laminar}}(r))|) \quad (18)$$

As we have mentioned in Sect. 3.2, high MIM value is only the necessary condition for molecular concentrations to be altered by the turbulence. This is clearly demonstrated in the Figure 5, where for species with the low MIM values of $\lesssim 0.25$ the maximum ratio between the vertical column densities calculated with the efficient 2D-mixing and the laminar models does not exceed an order of magnitude. For example, C⁺, CO, and NH₃ belong to this group of species. For larger MIMs the scatter in CDR values rapidly increases, reaching 10 orders of magnitude. The CH₃OH ice, SO₂, and CO₂ falls into this MIM range, with the CDRs in the range of 1.7–3.8 dex. The most extreme group of species populating the right top corner in Fig. 5 are carbon chains sitting in dust grain mantles (e.g., C₉H₄ ice). The linear Pearson correlation coefficient calculated for the MIM-CDR distribution is ≈ 0.5 – a medium/large confidence correlation. Thus our straightforwardly-defined MIM, which is easy to calculate as it only requires a non-mixing chemical model, can be useful in *a priori* analysis of a sensitivity of a given chemical species to the effects of transport.

To facilitate further interpretation of our results for the reader, we divide the disk into 3 chemically distinct regions (e.g., Aikawa et al. 2002; Semenov et al. 2004), using the abundance distributions of C⁺ and CO as a proxy (see Fig. 6). The hot and UV-irradiated atmosphere at $z \gtrsim 1.5 - 2H_{\text{r}}$ is molecularly poor, with ionized carbon being the primal C-bearing species. Deeper in the disk, in the warm molecular layer, C⁺ is converted into CO and a multitude of other molecules that remain in the gas phase (located between ~ 0.7 and ~ 2 pressure scale heights). The dense and cold disk midplane region is marked by the onset of molecular depletion from the gas phase ($\lesssim 0.5 - 0.9$ scale heights). Also, in what follows we refer to the regions located at radii $\lesssim 100$ AU as to the “inner” disk regions, and the “outer” disk regions otherwise.

The individual families of primal ions, C-, O-, N-, S-bearing and complex (organic) species are depicted in Figs. 7–12 and discussed in detail below. The major influence of turbulent transport on the disk chemical evolution can be summarized as follows. First, two-dimensional mixing behaves as a combination of vertical and radial mixing processes, that have to be considered simultaneously. Vertical mixing is more important as it affects the evolution of gas-phase and surface species of any kind, whereas the effect of radial mixing is pronounced mostly for the evolution of ices (e.g. the CO₂ ice from the OH and CO ices). The reason is that radial temperature gradient is weaker, and thus is only relevant for the evolution of polyatomic ices formed via surface reactions of heavy radicals. On the other hand, steep vertical gradients of temperature and high-energy radiation intensity cause much sharper transition from the ice-dominated chemistry in the disk midplane to the oasis of the gas-phase chemistry in the warm molecular layer.

Second, the inefficient diffusion in the slow mixing model leads to molecular abundances and column densities that almost coincide with those calculated with the laminar (non-mixing) model, but not always. The large Schmidt number $Sc = 100$ assumed for this model makes its characteristic dynamical timescale too long, $\sim 1 - 100$ Myr, to be competitive with most of the slowest chemical timescales determined by surface processes.

Third, diffusion in the fast mixing model enhances abundances and column densities of many species by several orders of magnitude (Tables 5–7). We divide all the consid-

ered species into three groups. Species with fast chemistry (faster than the diffusion timescale of $\sim 10^5 - 10^6$ years) are rather insensitive to turbulent transport. Further we call them “steadfast” species (Table 5). These include simple radicals and ions (e.g., C⁺, Mg⁺, CO, OH, C₂H, H₃O⁺, HCN, N₂) and few abundant ices (e.g., water and ammonia ices). Their column densities calculated with the laminar model and the fast mixing model differ by no more than a factor of 3-5, which is comparable to intrinsic uncertainties in molecular concentrations caused by uncertainties in the reaction rates (e.g., Vasyunin et al. 2008).

On the other hand, turbulent diffusion alters abundances of many polyatomic species, in particular complex (organic) molecules and their ices produced (at least partially) on dust grain surfaces (e.g., CO₂, HCOOH, CH₃CHO ice, carbon chain and cyanopolyyne ices, O₂ ice, SO, SO₂). These species are included in “sensitive” and “hypersensitive” groups. Col-

umn densities of “sensitive” species (Tables 6) are altered by diffusion by up to 2 orders of magnitude, and even stronger for a “hypersensitive” group (Table 7). Mixing steadily transports ice-coated grains in warmer regions, allowing more efficient surface processing due to enhanced hopping rates of heavy radicals. In warm intermediate layer these “rich” ices eventually evaporate, and in the inner disk they can also be photodissociated by CRP/X-ray-induced UV photons. The importance of mixing is higher in an inner, planet-forming disk zone, where thermal, density, and high-energy radiation gradients are stronger than in the outer region. Finally, even efficient 2D transport in the fast mixing model cannot completely erase the layered chemical structure in the disk, leaving the midplane a gas-phase molecular “desert”.

4.1. Major atomic and molecular ions and the ionization degree

Table 8
Key chemical processes: ionization degree

Reaction	α [(cm ³) s ⁻¹]	β	γ [K]	t _{min} [yr]	t _{max} [yr]
H ₂ + X-rays \rightarrow e ⁻ + H ₂ ⁺	0.93 ζ_X	0	0	1.00	1.20(4)
H ₂ + C.R.P. \rightarrow e ⁻ + H ₂ ⁺	0.93 ζ_{CR}	0	0	1.00	5.00(6)
H + X-rays \rightarrow H ⁺ + e ⁻	0.46 ζ_X	0	0	1.00	5.00(6)
C ⁺ + X-rays \rightarrow C ⁺⁺ + e ⁻	0.5 ζ_X	0	0	1.00	5.00(6)
S ⁺ + X-rays \rightarrow S ⁺⁺ + e ⁻	ζ_X	0	0	1.00	5.00(6)
H ₂ + X-rays \rightarrow e ⁻ + H + H ⁺	0.02 ζ_X	0	0	1.00	5.00(6)
C + UV \rightarrow e ⁻ + C ⁺	0.31(-9)	0	3.33	1.00	5.00(6)
H ₂ CO + UV \rightarrow HCO ⁺ + H + e ⁻	0.48(-9)	0	3.21	4.18(2)	1.20(4)
H ₂ ⁺ + UV \rightarrow H ⁺ + H	0.57(-9)	0	2.37	1.00	55.90
H ₃ ⁺ + UV \rightarrow H ⁺ + H ₂	0.20(-7)	0	1.80	1.00	5.00(6)
H ⁺ + O \rightarrow O ⁺ + H	0.70(-9)	0	2.32(2)	1.00	5.00(6)
H ⁺ + O ₂ \rightarrow O ₂ ⁺ + H	0.12(-8)	0	0	1.00	5.00(6)
H ⁺ + S \rightarrow S ⁺ + H	0.13(-8)	0	0	1.00	5.00(6)
He ⁺ + CO \rightarrow C ⁺ + O + He	0.16(-8)	0	0	1.00	5.00(6)
C ⁺ + H ₂ \rightarrow CH ₂ ⁺	0.40(-15)	-0.20	0	1.00	5.00(6)
S ⁺ + H ₂ \rightarrow H ₂ ⁺	1.00(-17)	-0.20	0	1.00	5.00(6)
H ₂ ⁺ + H ₂ \rightarrow H ₃ ⁺ + H	0.21(-8)	0	0	1.00	5.00(6)
H ₂ O ⁺ + H ₂ \rightarrow H ₃ O ⁺ + H	0.61(-9)	0	0	1.00	5.00(6)
N ₂ ⁺ + H ₂ \rightarrow N ₂ H ⁺ + H	0.17(-8)	0	0	1.00	5.00(6)
NH ⁺ + H ₂ \rightarrow H ₃ ⁺ + N	0.23(-9)	0	0	1.96	5.00(6)
C ⁺ + S \rightarrow S ⁺ + C	0.15(-8)	0	0	1.00	5.00(6)
H ₃ ⁺ + CO \rightarrow HCO ⁺ + H ₂	0.16(-8)	0	0	1.00	5.00(6)
H ₃ ⁺ + N ₂ \rightarrow N ₂ H ⁺ + H ₂	0.17(-8)	0	0	1.00	5.00(6)
HS ⁺ + H \rightarrow S ⁺ + H ₂	0.11(-9)	0	0	1.00	5.00(6)
N ₂ H ⁺ + CO \rightarrow HCO ⁺ + N ₂	0.88(-9)	0	0	1.00	5.00(6)
NH ₂ ⁺ + N \rightarrow N ₂ H ⁺ + H	0.91(-10)	0	0	1.00	5.00(6)
O ⁺ + H \rightarrow H ⁺ + O	0.70(-9)	0	0	7.48	5.00(6)
OH ⁺ + N ₂ \rightarrow N ₂ H ⁺ + O	0.36(-9)	0	0	2.34(4)	5.00(6)
S ⁺ + O ₂ \rightarrow SO ⁺ + O	0.20(-10)	0	0	1.00	5.00(6)
S ⁺ + OH \rightarrow SO ⁺ + H	0.46(-8)	-0.50	0	1.00	5.00(6)
S ⁺ + NH ₃ \rightarrow NH ₃ ⁺ + S	0.16(-8)	-0.50	0	1.00	5.00(6)
S ⁺ + e ⁻ \rightarrow S	0.39(-11)	-0.63	0	4.18(2)	5.00(6)
HCO ⁺ + e ⁻ \rightarrow CO + H	0.24(-6)	-0.69	0	1.00	5.00(6)
N ₂ H ⁺ + e ⁻ \rightarrow NH + N	0.64(-7)	-0.51	0	1.00	5.00(6)
H ₃ O ⁺ + e ⁻ \rightarrow OH + H + H	0.26(-6)	-0.50	0	1.00	5.00(6)
e ⁻ + grain(0) \rightarrow grain(-)	1.00	0	0	1.00	5.00(6)
HCO ⁺ + grain(-) \rightarrow CO + H + grain(0)	1.00	0	0	1.00	5.00(6)

The magnetorotational instability has been shown to be the most promising mechanism in driving turbulence in weakly ionized PPDs (Balbus & Hawley 1991). However, even high-energy cosmic ray particles cannot penetrate in cold and dense disk interiors (Umebayashi & Nakano 1981), and the ionization degree drops so low that MRI may not be oper-

ational at all (“dead zone”, e.g., Gammie 1996; Sano et al. 2000; Armitage et al. 2003; Ilgner & Nelson 2008). At these conditions slow radiative recombination of metallic ions becomes important for the evolution of ionization fraction, if these are still present in the gas (e.g., Fromang et al. 2002; Semenov et al. 2004; Ilgner & Nelson 2006a). On the other hand, the viscous stresses can be transported to the “dead zone” from above MRI-active accretion layers by

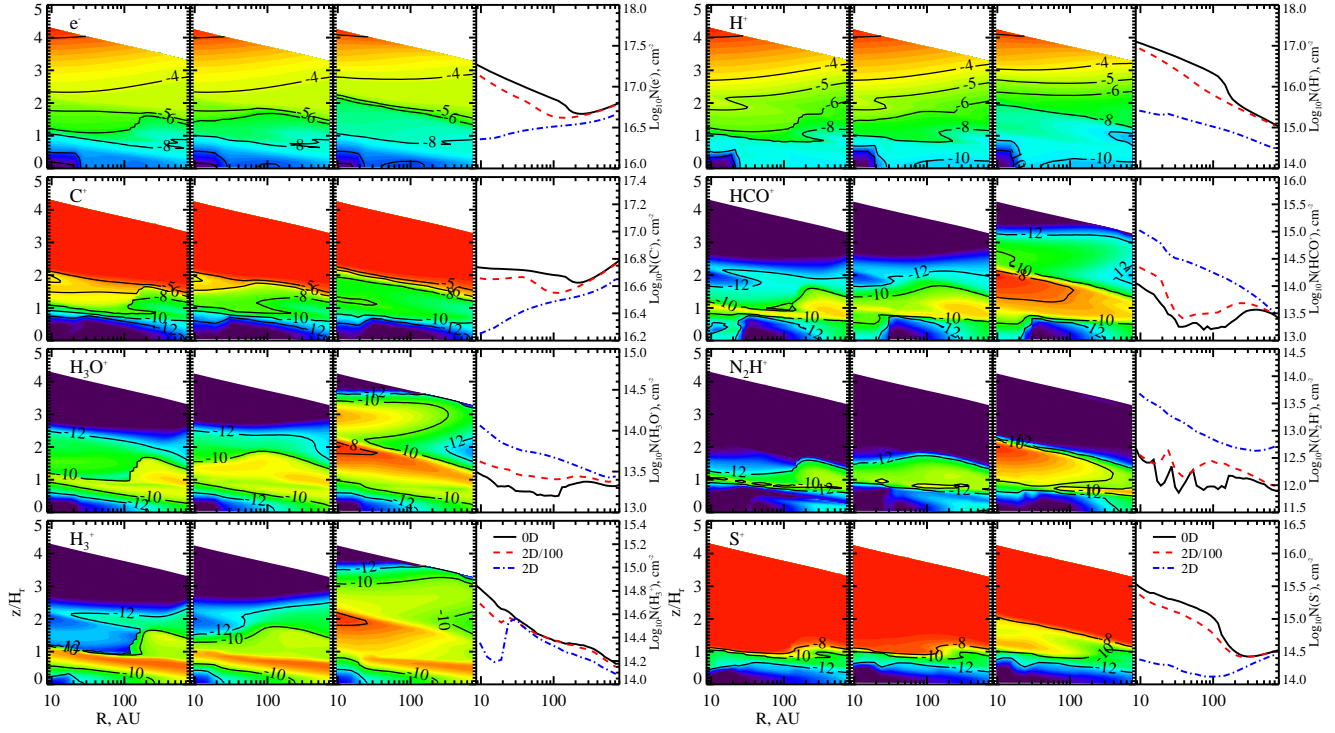


Figure 7. Abundances and column densities of electrons and selected ions in the DM Tau disk at 5 Myr. (Top to bottom) The log of relative abundances (with respect to the total number of hydrogen nuclei) and vertical column densities of electrons, H^+ , C^+ , HCO^+ , H_3O^+ , N_2H^+ , H_3^+ , and S^+ . (Left to right) Results for the three disk models are shown: (1) laminar chemistry, 2) the 2D-mixing chemistry ($Sc = 100$), and (3) the 2D-mixing chemistry with $Sc = 1$.

diffusive mixing, maintaining a low level of accretion in this region (e.g., Fleming & Stone 2003; Wünsch et al. 2006; Turner et al. 2007). In this Section we analyze in detail chemical processes responsible for the evolution of the ionization state of protoplanetary disks and how these are altered by turbulence.

Turbulent diffusion does not affect column densities of many atomic ions and a few simple molecular ions, e.g. C^+ , Mg^+ , Fe^+ , He^+ , H_3^+ , CH_3^+ , NH_4^+ (by less than a factor of 3, see Table 5). The charged species sensitive to mixing include, e.g., hydrocarbons, electrons, H^+ , O^+ , S^+ , N_2H^+ , and HCO^+ (their column densities are altered by factors of $\sim 3\text{--}50$; Table 6). Only a few ions are hypersensitive to mixing, e.g. N^+ , OH^+ , H_2O^+ (CDRs are ~ 100 ; Table 7). This is a manifestation of the fact that the global evolution of the ionization degree is partly affected by slow surface chemistry (recombination, dissociation) (see also Semenov et al. 2004).

In Fig. 7 the distributions of molecular abundances and column densities at 5 Myr of several major ions and the disk ionization degree calculated with the laminar and the mixing models are shown. The global ionization structure of the disk shows a layered structure similar to that of Photon-Dominated Regions (see also, e.g., Semenov et al. 2004; Bergin et al. 2007; Röllig et al. 2007): (1) heavily irradiated and ionized, hot atmosphere where the key ions are C^+ and H^+ , (2) partly UV-shielded, warm molecular layer where carbon is locked in CO and major charged species are X-ray-produced H^+ and polyatomic ions like HCO^+ and H_3^+ , and (3) dark, dense and cold midplane where most of molecules are frozen out onto dust grains and H_3^+ .

Turbulent diffusion lowers abundances of electrons and atomic ions such as C^+ , S^+ , and H^+ by up to 3 orders of

magnitude, mainly in the inner molecular layer ($r \lesssim 100$ AU, $\sim 1 - 2H_r$), see Fig. 7. Consequently, their column densities within ~ 100 AU are decreased by factors $3 - \gtrsim 100$, and much less in the outer disk. The effect is exactly opposite for H_3O^+ , HCO^+ , and N_2H^+ , which column densities and abundances are enhanced by the mixing in this region, albeit only up to an order of magnitude (Fig. 7). The mixing remarkably expands their inner molecular layers that are rather confined in the laminar case (particularly, for N_2H^+). The abundance distribution of H_3^+ shows similar expansion due to the mixing as the other polyatomic ions, while its column density is slightly decreased at $r \lesssim 30$ AU. Overall, turbulent stirring makes chemical gradients of key ionized species stronger compared to the laminar disk model. On the other hand, the slow mixing model does not differ significantly from the laminar model (compare 1st and 2nd panels in Fig. 7).

To better understand these results, we performed detailed analysis of the chemical evolution of the dominant ions and the ionization degree shown in Fig. 7 in two disk vertical slices at $r = 10$ and 250 AU (the laminar chemical model). The most important reactions responsible for the time-dependent net change of the electron, H^+ , C^+ , HCO^+ , H_3O^+ , N_2H^+ , H_3^+ , and S^+ concentrations in the midplane, molecular layer, and atmosphere are presented in Table 8, both for the inner and outer disk regions. Time interval when these processes are active is also shown. Note that our list contains only top 15 reactions for the selected species per region (midplane, molecular layer, atmosphere) for the entire 5 Myr time span, with all repetitions removed.

The energy deposition into the disk matter leads to ionization of molecular and atomic hydrogen by high-energy cosmic ray particles and the stellar X-ray radiation. Typical X-ray ionization rates in the inner and outer disk atmosphere

are $\zeta_X \approx 10^{-12} \text{ s}^{-1}$ and $\approx 2 10^{-13} \text{ s}^{-1}$, respectively. The H_2^+ is rapidly converted to H_3^+ by collisions with H_2 , while in the disk atmosphere both H_2^+ and H_3^+ can be dissociated by UV, producing H^+ . The line UV-photodissociation of molecular hydrogen is hindered by strong self-shielding of this molecule (Solomon & Wickramasinghe 1969; van Dishoeck 1988). In the atmosphere, the X-rays ionize other neutral atoms (e.g., He), and atomic ions such as C^+ and S^+ , leading to abundant doubly-charged atomic ions in the very inner region (see, e.g. Meijerink et al. 2008; Najita et al. 2010). The heavy atomic ions are also produced by charge transfer reactions with H^+ and C^+ . The atomic ions further slowly radiatively recombine with electrons (e.g., $\text{S}^+ + \text{e}^- \rightarrow \text{S}$) or converted to polyatomic ions by radiative recombination reactions (e.g., $\text{C}^+ + \text{H}_2 \rightarrow \text{CH}_2^+$) or via fast ion-molecule pathways involving simple radicals (e.g., $\text{S}^+ + \text{OH} \rightarrow \text{SO}^+ + \text{H}$). As a result, the disk fractional ionization in the atmosphere is high, $X(\text{e}^-) \approx 10^{-4}$, and dominant charged species are C^+ (with the abundance $\lesssim 10^{-4}$) and H^+ ($\sim 10^{-5} - 10^{-3}$). The pace of their chemical evolution is restricted to slow radiative recombination and association processes (e.g., Wakelam et al. 2010b), $\tau_{\text{chem}} \sim 10^3 - 10^4$ yrs. These timescales are comparable to the vertical mixing timescales ($\tau_{\text{phys}} \sim 10^3$ yrs) only in the inner disk region (see Figs. 3, 2, and Table 3).

In molecular layer located beneath the disk atmosphere the ionization chemistry is mostly regulated by fast ion-molecule reactions (see Fig. 3, 2nd panel), e.g. $\text{H}_3^+ + \text{N}_2 \rightarrow \text{N}_2\text{H}^+ + \text{H}_2$. Typical X-ray ionization rates in the inner and outer molecular layer are $\zeta_X \approx 10^{-12} \text{ s}^{-1}$ and $\approx 3 10^{-14} \text{ s}^{-1}$, respectively. The partly absorbed X-rays ionize H_2 , producing H_2^+ and H^+ . In the inner disk molecular layer, the X-ray-driven chemistry destroys 99% of molecular hydrogen ($r \lesssim 100$ AU). There H_2 is converted to atomic hydrogen via fast ion-molecule reactions involving OH^+ and H_2O^+ (e.g., $\text{H}_2\text{O}^+ + \text{H}_2 \rightarrow \text{H}_3\text{O}^+ + \text{H}$; Table 8). In turn, these ions become abundant due to steady release of elemental oxygen from water, which begins from photodissociation of the water ice. The H_2^+ is rapidly converted to H_3^+ that protonates abundant radicals (e.g., CO, N₂), forming various polyatomic ions (e.g., HCO⁺, N₂H⁺). Thus, the abundance distributions of the polyatomic ions are peaked along a rather narrow stripe, $0.5H_r$, where both H_3^+ and progenitor molecules are abundant. The molecular ion layers are vertically expanded in the outer disk at $r \gtrsim 200$ AU, where the surface density drops so low that the disk becomes partly transparent to the interstellar UV radiation. The N₂H⁺ is destroyed by reactions with abundant CO and, thence, the N₂H⁺ layer is particularly thin (see Fig. 7). The N₂H⁺, HCO⁺, and H₃O⁺ layers are rather sharp-edged from below where their parental molecules are locked in dust icy mantles (e.g., Öberg et al. 2007, 2009b,a), whereas the H₃⁺ layer extends more toward the cold region as H₂ does not deplete (e.g., Sandford et al. 1993; Buch & Devlin 1994; Kristensen et al. 2011). The formation of polyatomic ions is balanced out by dissociative recombination with e⁻ (Florescu-Mitchell & Mitchell 2006), and within $\approx 10^4$ years (inner disk) and $\approx 10^5$ years (outer disk) a chemical quasi steady-state is reached. This equilibrium timescale is mainly set by slow X-ray-driven destruction of H₂ that is needed to produce H₃⁺, $\tau_X \sim 2 10^3 - 10^5$ years. Thus the characteristic chemical timescales exceed those due to the mixing,

making the ionization state of the inner molecular layer to be vulnerable to the turbulent transport. The dominant charged species in the warm molecular layer are H⁺ as well HCO⁺, H₃O⁺ and C⁺, with abundances of $10^{-10} - 10^{-5}$. The resulting ionization fraction is $X\text{e}^- \sim 10^{-8} - 10^{-5}$, which is sufficient for MRI to be operational (e.g., Fromang et al. 2002).

Finally, in the cold, dark midplane the X-ray ionization rates further decrease ($\zeta_X \sim 10^{-19} - 10^{-15} \text{ s}^{-1}$), and the cosmic ray ionization becomes important ($\zeta_{\text{CR}} = 1.3 10^{-17} \text{ s}^{-1}$). Except of H₂, majority of molecules severely deplete within $\lesssim 10^3$ years, leaving only a tiny fraction in the gas (see Fig. 3, 4th panel, and Fig. 8). Electron sticking to grains is efficient, and negatively charged grains start playing important role as charge carriers (e.g., Umebayashi & Nakano 1980; Okuzumi 2009; Perez-Becker & Chiang 2011) and sites of dissociative recombination (e.g., HCO⁺ + grain(-) \rightarrow CO + H + grain(0); see Table 8). Consequently, the dominant charged species in the midplane are dust grains and H₃⁺, with H⁺ being important in the upper midplane layer (Fig. 7).

The fractional ionization drops to as low values as $\lesssim 10^{-12} - 10^{-9}$, and a “dead” zone for the MRI-driven accretion may develop (e.g., Gammie 1996; Turner et al. 2007; Dzyurkevich et al. 2010). Characteristic timescales of the evolution of the fraction ionization in the disk midplane are $\sim 5 10^3 - 10^5$ years, after which a quasi steady-state is reached. These values are shorter than the mixing timescale in the midplane (Fig. 3), and influence of turbulent transport on ionization chemistry shall be negligible.

Indeed, as can be clearly seen in Fig. 7 (compare 1st and 3rd panels), turbulent diffusion most strongly affects abundances of ions in the inner warm molecular layer, at $r \lesssim 200$ AU, $H_r \approx 1 - 2$, where the characteristic diffusive mixing timescale ($\sim 10^3$ years) is shorter than the chemical timescale ($\sim 10^4$ years) regulated by the slow X-ray-driven destruction of H₂ and radiative recombination and association processes involving C⁺. The diffusion timescale is relatively short in the inner disk because of stronger gradients of density and ionization rates, elevated temperatures, and short distances for transport (see Figs. 1 and 3). The vertical uptake of molecular hydrogen from the inner midplane to the inner intermediate layer allows to produce more H₃⁺, while simultaneously lowering ionization fraction and abundances of H⁺ and C⁺ due to their enhanced neutralization in via radiative association, charge exchange, and ion-molecule reactions (e.g., C⁺ + H₂ \rightarrow CH₂⁺; Table 8). The increased abundances of H₃⁺ in the inner molecular layer leads to more efficient production of polyatomic ions through protonation reactions, which lead to remarkable peaks in the relative abundances of HCO⁺, N₂H⁺, H₃O⁺, and other molecular ions. The chemistry of OH⁺, H₂O⁺, and N⁺ ions is most sensitive to the X-ray-driven, partly surface, processes (similar results were obtained by Aresu et al. 2011). Naturally, OH⁺, H₂O⁺, and N⁺ are most sensitive to the mixing in our model.

To summarize, turbulent mixing lowers the disk ionization fraction and the abundances of atomic ions in the inner disk region at intermediate heights ($r \lesssim 200$ AU, $\sim 1 - 2H_r$) by up to 3 orders of magnitude, whereas the concentrations of polyatomic ions are enhanced there.

4.2. Carbon-containing molecules

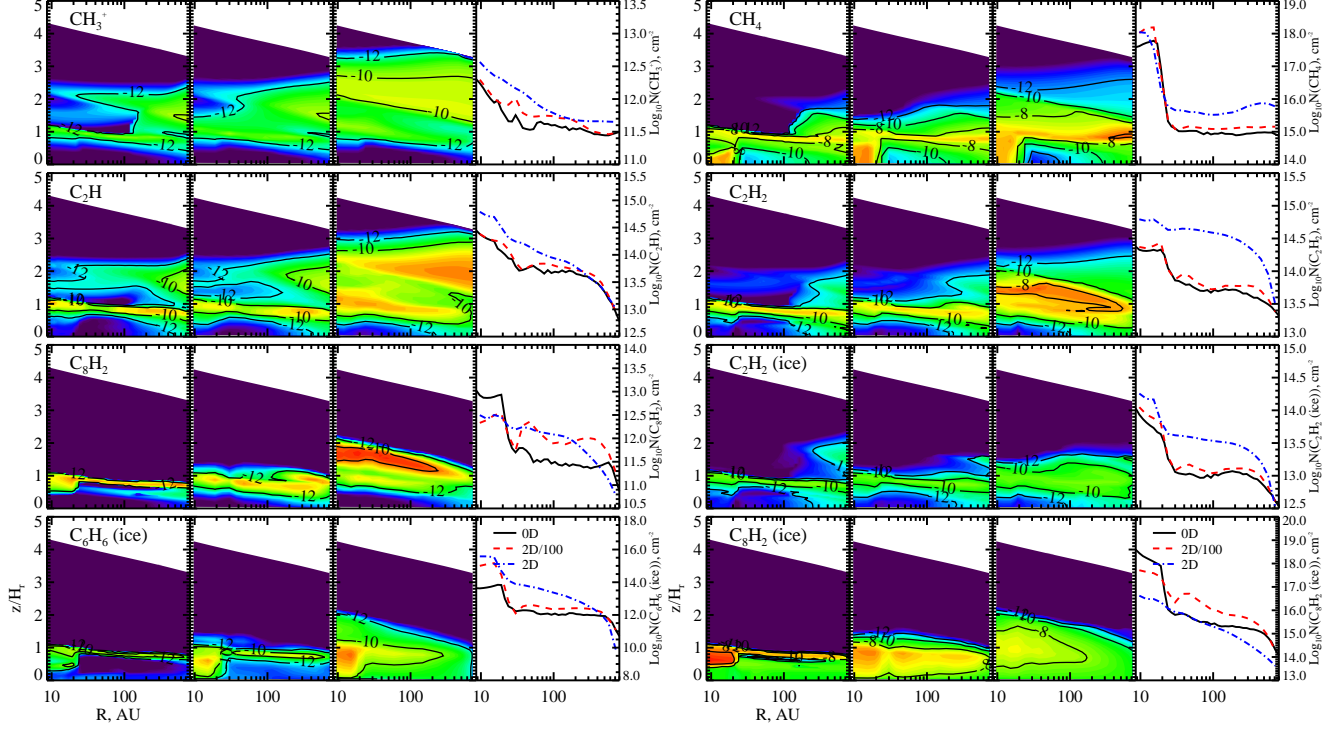


Figure 8. The same as in Fig. 7 but for the C-containing species. Results are shown for CH_3^+ , CH_4 , C_2H , C_2H_2 , C_8H_2 , C_2H_2 ice, C_6H_6 ice, and C_8H_2 ice. Abundance distribution patterns of many of the carbon chains look similar to that of C_8H_2 .

Table 9
Key chemical processes: C-bearing species

Reaction	α [(cm^3) s^{-1}]	β	γ [K]	t_{\min} [yr]	t_{\max} [yr]
C_6H_6 ice + $\text{h}\nu_{\text{CRP}}$ $\rightarrow \text{C}_6\text{H}_4$ ice + H_2 ice	3.00(3)	0	0	1.00	5.00(6)
C_8H_2 ice + $\text{h}\nu_{\text{CRP}}$ $\rightarrow \text{C}_8\text{H}$ ice + H ice	1.75(3)	0	0	1.00	5.00(6)
C_8H_4 ice + $\text{h}\nu_{\text{CRP}}$ $\rightarrow \text{C}_8\text{H}_2$ ice + H_2 ice	7.50(3)	0	0	1.00	5.00(6)
$\text{H}_2\text{C}_3\text{O}$ ice + $\text{h}\nu_{\text{CRP}}$ $\rightarrow \text{C}_2\text{H}_2$ ice + CO ice	1.80(3)	0	0	1.00	8.18(2)
C_2H_2 ice + UV $\rightarrow \text{C}_2$ ice + H ice + H ice	0.66(-10)	0	0	1.00	5.00(6)
C_6H_6 ice + UV $\rightarrow \text{C}_6\text{H}_4$ ice + H_2 ice	1.00(-9)	0	1.70	1.00	5.00(6)
C_8H_2 ice + UV $\rightarrow \text{C}_8\text{H}$ ice + H ice	1.00(-9)	0	1.70	1.00	5.00(6)
$\text{CH}_3 + \text{UV} \rightarrow \text{CH}_3^+ + e^-$	1.00(-10)	0	2.10	1.00	5.00(6)
$\text{C}_2\text{H} + \text{UV} \rightarrow \text{C}_2 + \text{H}$	0.52(-9)	0	2.30	1.00	5.00(6)
$\text{C}_2\text{H}_2 + \text{UV} \rightarrow \text{C}_2\text{H}_2 + \text{H}$	0.33(-8)	0	2.27	1.00	5.00(6)
$\text{C}_2\text{H}_3 + \text{UV} \rightarrow \text{C}_2\text{H}_2 + \text{H}$	1.00(-9)	0	1.70	1.00	1.75(5)
$\text{C}_2\text{H}_4 + \text{UV} \rightarrow \text{C}_2\text{H}_2 + \text{H}_2$	0.30(-8)	0	2.10	2.14(2)	1.75(5)
$\text{C}_8\text{H}_2 + \text{UV} \rightarrow \text{C}_8\text{H} + \text{H}$	1.00(-9)	0	1.70	1.00	5.00(6)
$\text{CH}_4 + \text{UV} \rightarrow \text{CH}_2 + \text{H}_2$	0.84(-10)	0	2.59	1.00	5.00(6)
$\text{C}_2\text{H} + \text{grain} \rightarrow \text{C}_2\text{H}$ ice	1.00	0	0	1.00	5.00(6)
$\text{C}_6\text{H}_6 + \text{grain} \rightarrow \text{C}_6\text{H}_6$ ice	1.00	0	0	1.00	5.00(6)
$\text{C}_2\text{H}_2 + \text{grain} \rightarrow \text{C}_2\text{H}_2$ ice	1.00	0	0	1.00	5.00(6)
$\text{C}_8\text{H}_2 + \text{grain} \rightarrow \text{C}_8\text{H}_2$ ice	1.00	0	0	1.00	5.00(6)
$\text{CH}_4 + \text{grain} \rightarrow \text{CH}_4$ ice	1.00	0	0	1.00	5.00(6)
C_2H_2 ice $\rightarrow \text{C}_2\text{H}_2$	1.00	0	2.59(3)	1.00	5.00(6)
C_8H_2 ice $\rightarrow \text{C}_8\text{H}_2$	1.00	0	7.39(3)	1.00	5.00(6)
CH_4 ice $\rightarrow \text{CH}_4$	1.00	0	1.30(3)	1.00	5.00(6)
H ice + CH_3 ice $\rightarrow \text{CH}_4$ ice	1.00	0	0	1.00	5.00(6)
H ice + CH_3^+ ice $\rightarrow \text{CH}_4$	1.00	0	0	1.00	5.00(6)
H ice + C_2 ice $\rightarrow \text{C}_2\text{H}$	1.00	0	0	1.00	5.00(6)
H ice + C_2H ice $\rightarrow \text{C}_2\text{H}_2$ ice	1.00	0	0	1.00	5.00(6)
H ice + C_2H ice $\rightarrow \text{C}_2\text{H}_2$	1.00	0	0	1.00	5.00(6)
H ice + C_8H_2 ice $\rightarrow \text{C}_8\text{H}_2$	1.00	0	0	1.00	5.00(6)
C_8H_2 ice + H ice $\rightarrow \text{C}_8\text{H}_3$ ice	1.00	0	1.21(3)	1.00	5.00(6)
$\text{CH}_3^+ + \text{H}_2 \rightarrow \text{CH}_3^+$	0.13(-13)	-1.00	0	1.00	5.00(6)
$\text{CH}_2^+ + \text{H}_2 \rightarrow \text{CH}_3^+ + \text{H}$	0.12(-8)	0	0	1.00	5.00(6)
$\text{CH}_3^+ + \text{C} \rightarrow \text{CH}_4 + \text{CH}^+$	1.00(-9)	0	0	1.00	5.00(6)
$\text{C}^+ + \text{C}_2\text{H}_6 \rightarrow \text{CH}_4 + \text{C}_2\text{H}_2^+$	0.17(-9)	0	0	4.18(2)	5.00(6)
$\text{CH}_3^+ + \text{CO} \rightarrow \text{CH}_4 + \text{HCO}^+$	0.32(-9)	-0.50	0	1.00	5.00(6)
$\text{CH}_4 + \text{H}^+ \rightarrow \text{CH}_3^+ + \text{H}_2$	0.23(-8)	0	0	1.00	5.00(6)
$\text{H}^- + \text{CH}_3 \rightarrow \text{CH}_4 + e^-$	1.00(-9)	0	0	1.09(2)	5.00(6)
$\text{C} + \text{C}_8\text{H}_2 \rightarrow \text{C}_9\text{H} + \text{H}$	0.90(-9)	0	0	1.00	5.00(6)

Table 9
Key chemical processes: C-bearing species

$C + CH_3 \rightarrow C_2H_2 + H$	1.00(-10)	0	0	1.00	5.00(6)
$C + CH_3C_6H \rightarrow C_8H_2 + H_2$	0.74(-9)	0	0	1.00	1.31(6)
$C_2H + O \rightarrow CO + CH$	0.17(-10)	0	0	1.00	5.00(6)
$C_3H + O \rightarrow C_2H + CO$	0.17(-10)	0	0	1.00	3.82
$C_3H_2 + O \rightarrow C_2H_2 + CO$	0.50(-10)	0.50	0	1.00	5.00(6)
$C_2H_2^+ + C \rightarrow C_2H_2 + C^+$	0.11(-8)	0	0	1.00	5.00(6)
$C_9H_3^+ + O \rightarrow C_8H_2 + HCO^+$	0.20(-9)	0	0	1.00	2.34(4)
$C_2H_2^+ + e^- \rightarrow C_2H + H$	0.29(-6)	-0.50	0	1.00	5.00(6)
$C_2H_3^+ + e^- \rightarrow C_2H_2 + H$	0.14(-6)	-0.84	0	1.00	5.00(6)
$C_2H_3^+ + e^- \rightarrow C_2H + H + H$	0.30(-6)	-0.84	0	1.00	5.00(6)
$C_3H_2^+ + e^- \rightarrow C_2H_2 + C$	0.30(-7)	-0.50	0	1.00	1.20(4)
$C_3H_2N^+ + e^- \rightarrow C_2H_2 + CN$	0.23(-6)	-0.50	0	1.00	5.00(6)
$C_3H_2N^+ + e^- \rightarrow C_2H + HNC$	0.75(-7)	-0.50	0	55.90	5.00(6)
$C_8H_3^+ + e^- \rightarrow C_8H_2 + H$	1.00(-6)	-0.30	0	1.00	5.00(6)
$C_8H_4^+ + e^- \rightarrow C_8H_2 + H_2$	1.00(-6)	-0.30	0	1.00	5.00(6)
$CH_2CO^+ + e^- \rightarrow C_2H_2 + O$	0.20(-6)	-0.50	0	1.00	5.00(6)
$CH_3^+ + e^- \rightarrow CH_4 + H$	0.14(-7)	-0.52	0	1.00	5.00(6)
$C_2H_3^+ + grain(-) \rightarrow C_2H + H + H + grain(0)$	0.59	0	0	7.48	5.00(6)

In this subsection we analyze in detail chemical and mixing processes responsible for the evolution of the hydrocarbons in protoplanetary disks.

There are only several steadfast light hydrocarbons, including 4 neutral diatomic and triatomic species (e.g., CH , CH_2 , C_2H), 4 ions (e.g., CH_3^+ , CH_5^+), and the C_2H_2 ice. Their column densities in the laminar model and the fast mixing model differ by a factor of $\lesssim 3$. In contrast, majority of hydrocarbons are sensitive to the turbulent transport that alters their column densities by up to 2 orders of magnitude. The turbulence-sensitive hydrocarbons include 28 neutral molecules (e.g., CH_3 , CH_4 , C_2H_2 , C_3H_2 , C_6H_6 , ..., C_9H_2), 8 ions (e.g., $C_2H_3^+$, $C_3H_2^+$, $C_6H_2^+$), and 22 ices (CH_4 , C_2 , C_2H , C_2H_3 , ..., C_9H_2 ; 58 species in total). Diffusive mixing modifies their column densities by up to 2 orders of magnitude. Finally, for 25 hypersensitive hydrocarbons the turbulent diffusion changes the column densities by more than 2 orders of magnitude (up to a factor of 10^{10} for the C_9H_4 ice). These species include no ions, 4 neutral hydrocarbons (e.g., C_{10} , C_3H_3 , CH_3C_4H), and 21 ices (C_2H_6 , C_3H_4 , C_5 , C_5H_4 , ..., C_9H , C_9H_4). A rough trend is that heavier and more saturated hydrocarbons are stronger affected by the turbulent transport than lighter species, and that abundances and column densities of hydrocarbon ices are stronger altered compared to their gas-phase counterparts. Overall, frozen hydrocarbons are among the most sensitive species to the mixing in our chemical model. Unlike the chemistry of the primal ions and the ionization degree discussed in the previous subsection, the chemical evolution of hydrocarbons should be dominated by slow surface hydrogenation and radical-radical growth processes, and slow evaporation.

In Fig. 8 distributions of relative abundances and column densities at 5 Myr of CH_3^+ , CH_4 , C_2H , C_2H_2 , C_8H_2 , C_2H_2 ice, C_6H_6 ice and C_8H_2 ice calculated with the laminar and mixing models are presented. The hydrocarbon abundances show a 3-layered structure similar to that of the polyatomic ions, with rather narrow molecular layers of $0.2\text{--}0.5H_r$ at $z \approx 1H_r$ and typical values of $\sim 10^{-10}\text{--}10^{-7}$. Note that relative abundances of hydrocarbon ices are also high in the warm molecular layer ($X \sim 10^{-10}\text{--}10^{-7}$). The hydrocarbons are fragile to the UV and X-ray irradiation and thus are absent in the disk atmosphere, apart from the photostable ethynyl rad-

ical (C_2H) and CH_3^+ ion that are abundant in the lower disk atmosphere, at $z \sim 2H_r$. In the midplane the gas-phase hydrocarbons are depleted, whereas their ices are moderately abundant. Turbulent mixing expands and enhances molecular layers of gas-phase hydrocarbons at almost all radii. For the ices there is no such a clear trend. As a rule, abundances of carbon chains that serve as intermediate products to surface hydrogenation are lowered by the turbulent transport, e.g. the C_8H_2 ice, whereas more saturated hydrocarbons show increased abundances, e.g. the C_6H_6 ice (Fig. 8). Note that the turbulent transport affects gas-phase and solid abundances of heavy hydrocarbons (like C_8H_2) in an opposite way, enhancing concentration of a gas-phase species and reducing its solid-state abundances. We attribute such a behavior to particularly slow evaporation of frozen heavy carbon chains that is comparable or longer than the dynamical timescale, $\lesssim 1$ Myr, even in the warm molecular layer.

To better understand these results, we performed detailed analysis of the chemical evolution of the hydrocarbons, shown in Fig. 8, in two disk vertical slices at $r = 10$ and 250 AU (the laminar chemical model). The most important reactions responsible for the time-dependent evolution of their abundances in the midplane, the molecular layer, and the atmosphere are presented in Table 9, both for the inner and outer disk regions. The final list contains only top 25 reactions for CH_3^+ , CH_4 , C_2H , C_2H_2 , C_8H_2 , C_2H_2 ice, C_6H_6 ice and C_8H_2 ice per region (midplane, molecular layer, atmosphere) for the entire 5 Myr time span, with all repetitions removed.

The chemical evolution starts with production of light hydrocarbons in the gas phase by radiative association of C^+ with H_2 , followed by hydrogen addition reactions: $C^+ \rightarrow CH_2 \rightarrow CH_3^+ \rightarrow CH_4$. An alternative route is the radiative association reaction between C and H_2 , leading to CH_2 , that can be further converted to C_2H by addition of C . The protonated methane reacts with electrons, O , CO , C , OH , etc., forming CH_4 . Methane undergoes reactive collisions with C^+ , producing $C_2H_2^+$ and $C_2H_3^+$. All these primal hydrocarbons dissociatively recombine on electrons or negatively charged grains (in the inner dark midplane), which leads to simple neutral species like CH , CH_3 , C_2H , and C_2H_2 . The neutral hydrocarbons readily react with ionized and neutral atomic carbon, forming other, heavier hydrocarbons, e.g. $C_8H_2 + C \rightarrow C_9H + H$ and $C_9H_3^+ + O \rightarrow C_8H_2 + HCO^+$. The growth rate of chemical complexity of carbon chains is regulated by ion-molecule

and neutral-neutral exothermic reactions with atomic oxygen that lead to formation of CO, e.g. $O + C_3H_2 \rightarrow C_2H_2 + CO$ (see also Fig. 7 in Henning et al. (2010) and Fig. 4 in Turner et al. (2000)). The associated chemical timescales are $\lesssim 10^3 - 10^4$ years, see Fig. 3 and Tables 3 and 4, but not everywhere in the disk. In the disk atmosphere, at $z \approx 2H$, the chemical evolution of CH_2 and its daughter species, C_2H and CH_3 , is subject to the evolution of H_2 and O. As we discussed in the previous subsection, at these high altitudes slow destruction of molecular hydrogen, water, and CO by He^+ locally sets long evolutionary timescales ($\lesssim 10^5$ years) for many species, e.g. ethynyl, CH_2 , and CH_3 radicals.

To enhance further production of hydrocarbons in the gas, particular physical conditions have to be reached. The heavy carbon-bearing compounds can be produced at high densities and $T \gtrsim 800$ K by pyrolysis of precursor hydrocarbons (e.g., Morgan et al. 1991) or in a Fischer-Tropsch-like process involving CO, H_2 , and catalytic surfaces (Tscharnutter & Gail 2007). These conditions are met at sub-AU radii in the very inner disk midplane that is not examined in the present study. Another possibility for the gas-phase production of hydrocarbons is to bring elemental carbon locked in CO back to the gas, while simultaneously maintaining low oxygen abundances. Due to self-shielding and mutual-shielding by H_2 , the UV photodissociation of CO is only important in dilute disk atmosphere (e.g., van Dishoeck 1988; Visser et al. 2009a). However, in the lower part of the inner warm molecular layer ($r \lesssim 200$ AU, $z \approx 1H$) the He^+ ions produced by the X-ray ionization slowly destroy CO, restoring gas-phase concentrations of C^+ and O ($\tau_X \sim 5 \cdot 10^3$ years). Relatively high densities ($n(H) \sim 10^8 - 10^9 \text{ cm}^{-3}$) and lukewarm temperatures ($T \sim 30 - 75$ K) in this region (Fig. 1) allow rapid conversion of released oxygen into water. Thus, locally in the inner regions of the X-ray-irradiated disks the gas-phase C/O ratio may revert from the Solar value of ≈ 0.43 to a $\gtrsim 1$ value typical of carbon-rich AGB shells (D. Hollenbach, priv. comm.), which facilitates gas-phase formation of heavy hydrocarbons.

An alternative efficient route to accumulate complex hydrocarbons in disks is surface chemistry coupled to the destruction of hydrocarbon ices and other C-bearing species. In cold disk regions ($T \lesssim 20$ K) it is mainly hydrogenation of precursor species like C_nH_m ($n = 2 - 9$, $m \leq 2$). At low dust temperatures only hydrogen is mobile to scan the grain surface (e.g., d'Hendecourt et al. 1985; Hasegawa & Herbst 1993; Katz et al. 1999). Ultimately, this process leads to formation of saturated ices, e.g. CH_4 and C_2H_6 , which have 5% chance to escape directly to the gas upon surface recombination (Sect. 2.2). Our model has a restricted set of hydrocarbon chemistry involving species with ≤ 10 carbon atoms and mostly having up to 4 hydrogen atoms only, and thus these processes do not appear in Table 9. In the inner disk midplane ($r \lesssim 20$ AU) warmed up by the accretion to the temperatures of $\sim 40 - 50$ K, desorption of CH_4 dominates over its sticking to grains, forming an oasis of abundant gas-phase methane. At these elevated temperatures heavier radicals like C, O, OH, etc. become partly mobile (e.g., Garrod & Herbst 2006; Garrod et al. 2008; Herbst & van Dishoeck 2009). However, the surface growth of hydrocarbons by addition of atomic carbon is still not as efficient as the surface hydrogenation and the gas-phase chemistry, and accounts for only a few percent of the total surface production rate. The most favorable condi-

tions for active surface hydrocarbon chemistry are met in the warm molecular layer, where atomic hydrogen is plentiful in the gas, and its accretion rate is fast even in comparison with rapid desorption. More importantly, complex ices are slowly destroyed by X-ray/CRP-driven photons as well as by partly absorbed stellar (inner disk) and interstellar UV (outer disk) photons, producing various reactive radicals. For example, C_8H is produced by photodestruction of C_8H_2 ice, followed by evaporation (Table 9). In the outer disk partly transparent to the IS UV radiation these surface photoprocesses become important even in the midplane (see C_2H_2 in Fig. 8).

Note that our chemical network lacks the surface formation of benzene apart from its accretion from the gas. The major production pathway for C_6H_6 is via ion-molecule reactions of C_3H_4 and $C_3H_4^+$ ($\alpha = 7.5 \cdot 10^{-10} \text{ cm}^3 \text{ s}^{-1}$) as well as C_2H_4 and $C_6H_5^+$ ($\alpha = 5.5 \cdot 10^{-11} \text{ cm}^3 \text{ s}^{-1}$), followed by the dissociative recombination, and freeze-out at $T \lesssim 150$ K. In turn, $C_3H_4^+$ and $C_6H_5^+$ are synthesized from neutral hydrocarbons by rapid charge transfer with ionized hydrogen and carbon or via protonation by H_3^+ , H_3O^+ , HCO^+ , etc. The benzene building blocks, C_3H_3 and C_3H_4 , are produced effectively via a number gas-phase and surface reactions as described above. The characteristic chemical timescale for benzene is thus mainly determined by the evolution of C_3H_3 and C_3H_4 , which involves slow surface routes.

As we already discussed in Sect. 3.1, the surface chemistry timescales are the longest in the disk chemistry, typically exceeding several Myr (see also Tables 3 and 4). Photoprocessing of ices on dust grains has similar timescale in the molecular layer and the disk midplane, $\tau_{\text{chem}} \lesssim 10^6$ years (Fig. 3). The overall pace of the surface chemistry is also dependent on the amount of involved surface processes. Thus, the characteristic chemical timescales for hydrocarbons are beyond 1 Myr, particularly for the heaviest and most saturated ones in the network (e.g., C_8H_4 , etc.). Not surprisingly, the 2D-turbulent mixing strongly affects the hydrocarbon chemistry in disks. The evolution of heaviest carbon chains with more than 6 carbon atoms is so far from a steady-state that it becomes sensitive to transport processes even in the slow mixing model (see, e.g., the C_8H_2 ice in Fig. 8). The vertical transport brings up dust grains from the midplane to the upper, more irradiated and warmer disk regions, allowing more efficient photoprocessing of ices, photodesorption of frozen hydrocarbons, and their photodissociation. These processes increase relative abundances of gas-phase hydrocarbons by up to several orders of magnitude. In turn, vertical transport downward allows to retain newly formed hydrocarbon radicals in the icy mantles and facilitates their slow hydrogenation. The radial mixing does not play a major role in the hydrocarbon chemistry. Consequently, abundances of the most saturated hydrocarbon ices in the network are increased by vertical mixing, in particular in the inner disk with the shortest dynamical timescales (e.g., benzene ice), whereas the intermediate products become less abundant (e.g., C_8H_2 ice). Note also that the mixing allows CH_2 and C_2H to be more efficiently formed in the outer disk atmosphere, where their second layers of high relative abundances are developed. This is caused by the turbulent transport upward of the molecular hydrogen from the molecular layer, which is otherwise slowly destroyed in the atmosphere by the X-rays and the cosmic ray particles.

4.3. Oxygen-containing molecules

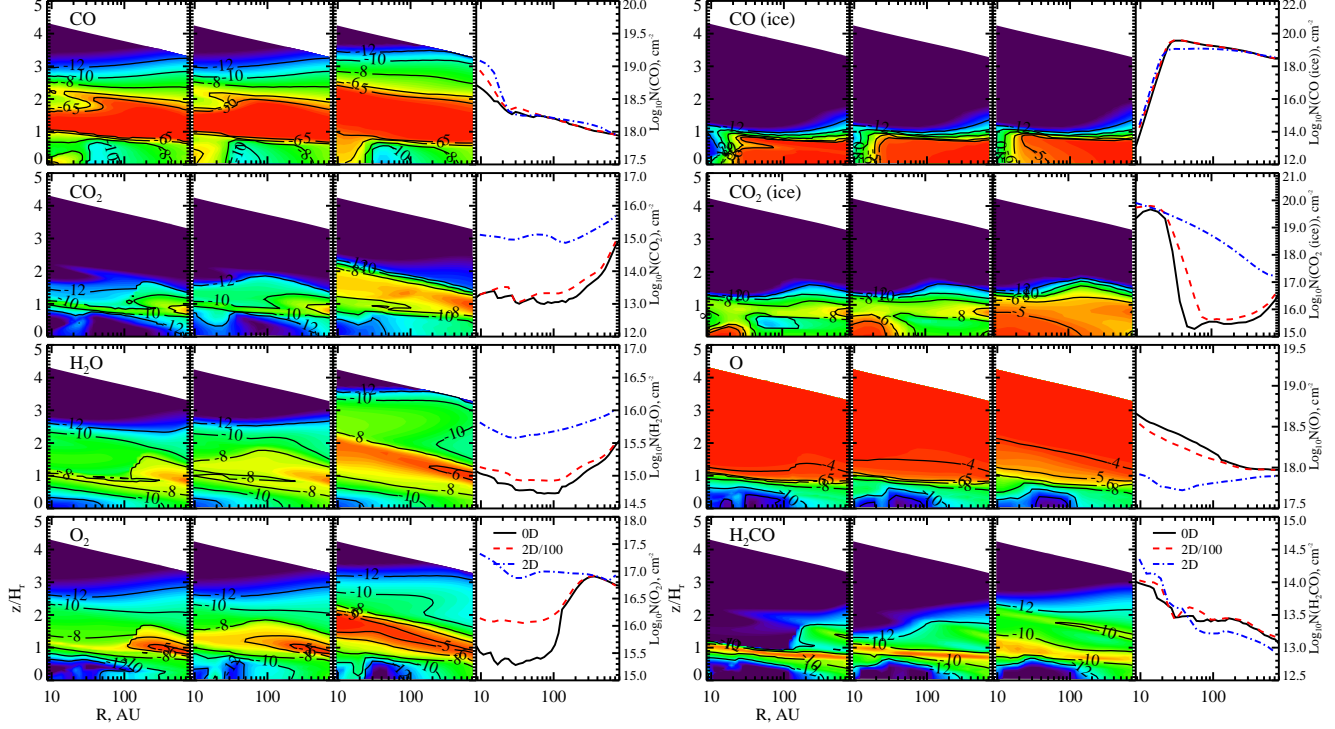


Figure 9. The same as in Fig. 7 but for the O-containing species. Results are shown for CO, CO ice, CO₂, CO₂ ice, H₂O, O, O₂, and H₂CO.

Table 10
Key chemical processes: O-bearing species

Reaction	α [(cm ³) s ⁻¹]	β	γ [K]	t _{min} [yr]	t _{max} [yr]
CO ₂ ice + hν _{CRP} → CO ice + O ice	1.71(3)	0	0	1.00	5.00(6)
CO + UV → O + C	0.20(-9)	0	3.53	1.00	5.00(6)
CO ₂ + UV → CO + O	0.89(-9)	0	3.00	1.00	5.00(6)
H ₂ O + UV → OH + H	0.80(-9)	0	2.20	1.00	5.00(6)
O + grain → O ice	1.00	0	0	1.00	5.00(6)
O ₂ + grain → O ₂ ice	1.00	0	0	1.00	5.00(6)
CO + grain → CO ice	1.00	0	0	1.00	5.00(6)
CO ₂ + grain → CO ₂ ice	1.00	0	0	1.00	5.00(6)
H ₂ CO + grain → H ₂ CO ice	1.00	0	0	1.00	5.00(6)
H ₂ O + grain → H ₂ O ice	1.00	0	0	1.00	5.00(6)
O ice → O	1.00	0	8.00(2)	1.00	5.00(6)
O ₂ ice → O ₂	1.00	0	1.00(3)	1.00	5.00(6)
CO ice → CO	1.00	0	1.15(3)	1.00	5.00(6)
CO ₂ ice → CO ₂	1.00	0	2.58(3)	1.00	5.00(6)
H ₂ CO ice → H ₂ CO	1.00	0	2.05(3)	1.00	5.00(6)
H ice + OH ice → H ₂ O	1.00	0	0	1.00	5.00(6)
H ice + HCO ice → H ₂ CO	1.00	0	0	1.00	5.00(6)
OH ice + CO ice → CO ₂ ice + H ice	1.00	0	80.00	1.00	5.00(6)
OH ice + CO ice → CO ₂ + H	1.00	0	80.00	1.00	5.00(6)
CH ₂ ice + O ₂ ice → H ₂ CO + O	1.00	0	0	1.96	5.00(6)
CO ⁺ + H → CO + H ⁺	0.40(-9)	0	0	1.00	5.00(6)
CO ₂ + H ⁺ → HCO ⁺ + O	0.30(-8)	0	0	1.00	5.00(6)
H ₂ O + H ⁺ → H ₂ O ⁺ + H	0.73(-8)	-0.50	0	1.00	5.00(6)
O + H ⁺ → O ⁺ + H	0.70(-9)	0	2.32(2)	1.00	5.00(6)
O ₂ + H ⁺ → O ₂ ⁺ + H	0.12(-8)	0	0	3.82	5.00(6)
HCO ₂ ⁺ + CO → CO ₂ + HCO ⁺	0.25(-9)	-0.50	0	1.00	5.00(6)
O ⁺ + H → O + H ⁺	0.70(-9)	0	0	1.00	5.00(6)
O ⁻ + CO → CO ₂ + e ⁻	0.65(-9)	0	0	7.48	5.00(6)
CO + He ⁺ → O + C ⁺ + He	0.16(-8)	0	0	1.00	5.00(6)
H ₂ CO + H ₃ ⁺ → H ₃ CO ⁺ + H ₂	0.55(-8)	-0.50	0	1.96	5.00(6)
H + OH → H ₂ O	0.40(-17)	-2.00	0	7.48	5.00(6)
CO + OH → CO ₂ + H	0.28(-12)	0	1.76(2)	1.00	5.00(6)
O + C ₂ → CO + C	1.00(-10)	0	0	1.00	6.11(3)
O + CH ₃ → H ₂ CO + H	0.14(-9)	0	0	1.00	5.00(6)
O + HCO → CO ₂ + H	0.50(-10)	0	0	1.00	5.00(6)
O + OH → O ₂ + H	0.75(-10)	-0.25	0	1.00	5.00(6)
O + H ₂ CO → CO + OH + H	1.00(-10)	0	0	1.00	5.00(6)
O ₂ + C ₃ → CO ₂ + C ₂	1.00(-12)	0	0	1.00	5.00(6)
O ₂ + C → O + CO	0.47(-10)	-0.34	0	1.00	5.00(6)

Table 10
Key chemical processes: O-bearing species

$\text{H}_3\text{O}^+ + \text{e}^- \rightarrow \text{H}_2\text{O} + \text{H}$	0.11(–6)	–0.50	0	1.00	5.00(6)
$\text{HCO}_2^+ + \text{e}^- \rightarrow \text{CO}_2 + \text{H}$	0.60(–7)	–0.64	0	1.00	5.00(6)
$\text{H}_2\text{CO}^+ + \text{e}^- \rightarrow \text{H}_2\text{CO}$	0.11(–9)	–0.70	0	14.60	5.00(6)
$\text{H}_3\text{O}^+ + \text{e}^- \rightarrow \text{O} + \text{H} + \text{H}_2$	0.56(–8)	–0.50	0	3.82	5.00(6)
$\text{O}_2^+ + \text{e}^- \rightarrow \text{O} + \text{O}$	0.19(–6)	–0.70	0	1.96	1.75(5)
$\text{H}_3\text{O}^+ + \text{grain}(-) \rightarrow \text{H}_2\text{O} + \text{H} + \text{grain}(0)$	0.25	0	0	1.00	5.00(6)
$\text{CH}_3\text{O}_2^+ + \text{grain}(-) \rightarrow \text{CO}_2 + \text{H}_2 + \text{H} + \text{grain}(0)$	0.50	0	0	28.60	3.42(5)
$\text{O}_2^+ + \text{grain}(-) \rightarrow \text{O} + \text{O} + \text{grain}(0)$	1.00	0	0	1.96	1.75(5)

The chemical evolution of O, O₂, CO, CO₂ and water is of particular attention in astrophysics since the recent puzzling results obtained with *Spitzer*, *Herschel*, *SWAS*, and *Odin* satellites (e.g., Larsson et al. 2007; Carr & Najita 2008; Bergin et al. 2010; Jørgensen & van Dishoeck 2010), and their potential relevance for astrobiology (e.g., Selsis et al. 2002; Kaltenegger et al. 2007; Segura et al. 2007). In this subsection we analyze in detail chemical and mixing processes responsible for the evolution of oxygen-bearing species in protoplanetary disks. We focus on simple neutral molecules that are composed of O, C, H only, and consider complex organics in separate subsection.

There are 4 steadfast neutral O-bearing molecules (CO, OH, H₂CO, and the water ice), and 3 steadfast ions (H₂CO⁺, H₃CO⁺, and H₃O⁺) (Table 5). Their column densities in the laminar model and the fast mixing model differ by a factor of 3. Among the species sensitive to the turbulent transport (Table 6) there are 5 molecules (C₃O, H₂O, HCO, O, O₂), 3 ions (HCO⁺, O⁺, O₂⁺), and 4 solid species (CO, H₂CO, O, OH ices). Their column densities are changed by up to 2 orders of magnitude by the turbulent transport. The hypersensitive O-bearing species (Table 7) include 3 molecules (CO₂, H₂O₂, O₃), 2 ions (OH⁺, H₂O⁺) and 5 ices (CO₂, H₂O₂, O₂, O₂H, O₃). The turbulent diffusion alters their column densities by up to a factor of 4 000 (CO₂ ice). Apparently, neutral species with a large number of oxygen atoms (e.g., ozone) affected more strongly by the turbulent mixing than the molecules containing a single O (e.g., CO). Similar to the hydrocarbon chemistry, abundances and column densities of O-bearing ices are stronger altered by the turbulent diffusion compared to the gas-phase molecules. Once again this is an indicator that the chemical evolution of the multi-oxygen molecules in protoplanetary disks is at least partly governed by slow chemical processes (surface recombination, photodissociation of ices, etc.).

In Fig. 9 the distributions of the relative molecular abundances and column densities at 5 Myr of CO, CO ice, CO₂, CO₂ ice, H₂O, O, O₂, and H₂CO calculated with the laminar and the 2D-mixing models are presented. The abundance distribution of atomic oxygen shows a 2-layered structure, with a maximum of relative concentrations ($X(\text{O}) \approx 1.5 \cdot 10^{-4}$) in the disk atmosphere and an upper part of the molecular layer, and strong depletion in the midplane ($X(\text{O}) \lesssim 10^{-11}$). On the other hand, CO and CO₂ ices are concentrated in the midplane and a lower part of the molecular layer (at $z \approx 1H_r$), with typical relative abundances of $\lesssim 10^{-5}$. The CO₂ ice abundance is particularly high in the inner warm midplane ($r \leq 20$ AU). Its distribution is also 2-layered. The rest of considered O-molecules show a 3-layered abundance structure similar to that of the polyatomic ions and hydrocarbons.

The carbon monoxide spreads over a wide vertical heights in the disk due to self-shielding (e.g., van Dishoeck 1988; Lyons & Young 2005; Visser et al. 2009a) and low desorption energy of ~ 1000 K (e.g., Bisschop et al. 2006), $z \approx 1 - 2.5$ at $r = 10$ AU and $z \approx 0.8 - 2$ at $r = 800$ AU, with a typical abundance of $7.6 \cdot 10^{-5}$. The tip of low CO abundances in the inner low atmosphere at $2H_r$ is due to enhanced X-ray-driven dissociation in this region (see also Sect. 3.1). Note that gas-phase CO in the laminar model is partially produced in the very inner disk midplane ($r < 20$ AU). The H₂O is also wide-spread throughout the disk, though due to photodissociation and rapid freeze-out at $T \lesssim 120$ K its peak abundances of $10^{-8} - 10^{-7}$ are confined to the bottom of the molecular layer, with a maximum in the outer disk region at $r \gtrsim 200$ AU (Fig. 9). Gas-phase water comprises less than 0.01% of the total water abundance that are locked in dust mantles in the midplane. The O₂ abundance distribution has almost the same pattern as that of gas-phase water, with maximum values of $X(\text{O}_2) \approx 10^{-7} - 3 \cdot 10^{-5}$. The peak CO₂ relative abundances are narrow and rather low, $\sim 10^{-10} - 10^{-8}$, and restricted to the very outer disk ($r \gtrsim 400$ AU). In contrast, the H₂CO has a radially-uniform, narrow ($\approx 0.3H_r$) molecular layer, with maximum abundances of $\sim 10^{-10} - 10^{-9}$ at $z \approx 0.8 - 1H_r$.

Turbulent mixing does not considerably affect column densities of H₂CO and CO in gas and solid phases, although it populates the viscously-heated inner midplane with carbon monoxide, and slightly widens their molecular layers upward (Fig. 9). Unlike atomic ions, the mixing softens the vertical gradient of the atomic oxygen abundances, and lowers its column density. Turbulent diffusion transports solid CO₂ from the inner midplane radially and vertically outward, enhancing its column densities and abundances by more than 3 orders of magnitude at $r \gtrsim 30$ AU. Finally, column densities of gas-phase CO₂, H₂O, and O₂ are increased by the turbulence by factors of 10-1 000, with their molecular layers enriched and vertically expanded up to $\sim 1.2 - 2H_r$ and more homogeneously distributed in the radial direction.

To better understand these results, we performed detailed analysis of the chemical evolution of CO, CO ice, CO₂, CO₂ ice, H₂O, O, O₂, and H₂CO in two disk vertical slices at $r = 10$ and 250 AU (the laminar chemical model). The most important reactions responsible for the evolution of their abundances in the midplane, the molecular layer, and the atmosphere are presented in Table 10, both for the inner and outer disk regions. The final list contains only top 25 reactions per region (midplane, molecular layer, atmosphere) for the entire 5 Myr time span, with all repetitions removed.

The chemical evolution of the selected O-bearing species is governed by a limited set of reactions. Atomic oxygen is present in the disk atmosphere and converted to CO, CO₂ and H₂O in the midplane and the molecular layer. The rate

of its conversion in the molecular layer is partly regulated by the evolution of H_3^+ and hydrocarbons, which is in turn determined by the slow X-ray irradiation of H_2 (Sect. 4.1) and the slow release of O from CO by the X-ray-ionized helium atoms in the inner disk (Sect. 4.2), and the surface chemistry of O-bearing species. The resulting chemical timescale of $\gtrsim 1$ Myr exceeds the transport timescale in the molecular layer (Tables 3 and 4).

The water ice forms on the dust surfaces via accretion of the gas-phase water in disk regions with $T \lesssim 120$ K, and via surface hydrogenation of frozen atomic oxygen and hydroxyle (minor route). The destruction pathways for water ice are thermal or photoevaporation (major route), and further hydrogenation to hydrogen peroxide ice (very minor route). In the gas, water formation begins by production of OH^+ from O and H_3^+ , followed by subsequent hydrogen abstraction reactions with H_2 till H_3O^+ is created. The protonated water dissociatively recombines with electrons or negatively charged grains into H_2O (25%) or OH (74%) or O (1%), or de-protonates by ion-molecule reactions with other abundant neutral molecules (CH_4 , CO, etc.). The gas-phase formation of water is assisted by slow radiative recombination reaction between H and OH, and photoevaporation of water ice in the warm molecular layer. The gas-phase removal channels for H_2O include photodissociation, charge transfer reactions with H^+ followed by dissociative recombination, freeze-out, and reactions with He^+ (minor route). The solid water is a terminal species that serves as one of the sinks of the elemental oxygen in the disks. Thus, the key chemical processes leading to the evolution of water are fast, $\tau_{\text{chem}} \lesssim 1 - 10^2$ years, in the atmosphere and the midplane, whereas in the molecular layer it is regulated by the late-time evolution of H_3^+ due to the X-ray ionization ($\tau_{\text{chem}} \gtrsim 10^4$ years; see Sect. 4.1).

The molecular oxygen is produced in the gas by neutral-neutral exothermic reactions of OH and O, and destroyed in ion-molecule and neutral-neutral combustion reactions with various radicals (mostly dehydrogenated hydrocarbons, e.g., C, C_3 , etc.), by photodissociation, and via ion-molecule reactions of O_2 with H_3^+ and ionized C and H, followed by dissociative recombination of O_2^+ into atomic oxygen. On dust surfaces molecular oxygen is produced either directly from the recombination of oxygen atoms at conditions when surface O becomes mobile ($T \gtrsim 30$ K; the inner disk midplane and the warm molecular layer), or via surface oxidation reactions: O (ice) + OH (ice) \rightarrow O_2H (ice) and O (ice) + O_2H (ice) \rightarrow O_2 (ice) + OH (ice). The surface O_2 can be further converted to O_3 ice. The characteristic chemical timescale for O_2 is set by the slow surface chemistry timescale ($\tau_{\text{chem}} \gtrsim 10^6$ years).

CO molecules serve as a sink of almost all elemental carbon and about a half of elemental oxygen in disks. Carbon monoxide is formed essentially in the gas-phase via reactions of atomic oxygen with CH , CH_2 , and C_2 , and other abundant hydrocarbons (see previous subsection and Table 9). The removal pathway of CO in the gas include freeze-out onto the grain surfaces (major channel), and the slow ion-molecule reaction with He^+ (minor channel). In the upper, heavily UV-irradiated and dilute disk atmosphere CO is also UV-photodissociated ($z \gtrsim 2.5 H_r$). At $T \lesssim 30$ K, in the outer midplane CO sticks to the grains and partly converted to H_2CO and CH_3OH ices via hydrogenation reactions, whereas in the warm midplane ($r \lesssim 30$ AU, $T \gtrsim 30 - 40$ K) CO is transformed into CO_2 in a slightly endothermic reaction between the CO and OH ices (with a barrier of 80 K). The chemistry

of CO gas reaches a steady-state in the molecular layer and the cold outer midplane within less than $10^2 - 10^4$ years (see Fig. 2). The quasi-equilibrium CO chemistry in the molecular layer is restricted to protonation of CO molecules by H_3^+ into HCO^+ , balanced by dissociative recombination. In the disk atmosphere CO chemistry is controlled by the photodissociation slowed down by self- and mutual-shielding by H_2 , and $\tau_{\text{chem}} \lesssim 10^4 - 10^6$ years. Finally, in the inner warm midplane the surface conversion of CO into CO_2 leads to a very long timescale of $\lesssim 1$ Myr.

The carbon dioxide is a daughter molecule of CO, and is mainly produced in the gas phase via oxidation of HCO ($\text{O} + \text{HCO} \rightarrow \text{CO}_2 + \text{H}$), slow combustion of C_3 and C_2H , slow endothermic reaction of CO and OH with a barrier of 176 K (Table 10), and desorption of CO_2 ice at $T \gtrsim 60$ K or UV-photodesorption. The main removal gas-phase pathways include photodissociation, ion-molecule reactions with C^+ and H^+ (forming CO^+ and HCO^+ , respectively), and accretion to dust grains. The solid CO_2 is mainly produced via endothermic reaction of surface CO and OH in the disk inner midplane and the low part of the entire molecular layer, and through accretion of the gas-phase carbon dioxide. The CO_2 ice is destroyed by the X-ray/CRP-induced UV photons in the inner midplane, and via thermal and UV-desorption. Thus, the CO_2 chemistry has particularly long timescale associated with surface reaction of CO and OH, and slow photoprocessing of the CO_2 ice ($\tau_{\text{chem}} \gtrsim 1$ Myr).

Finally, the H_2CO molecule is mostly produced in the gas-phase through reaction of CH_3 with oxygen atoms, and desorption of formaldehyde ice. The major gas-phase removal routes are sticking to dust in the disk regions with $T \lesssim 40 - 50$ K, photodissociation, reactions with ionized atomic C and H, oxidation by O (into CO, OH, and H), and protonation by H_3^+ followed by dissociative recombination back to H_2CO (33%), or CO (33%), or HCO (33%). The surface evolution of H_2CO is governed by accretion and desorption processes, and a sequence of surface hydrogenation of CO into CH_3OH where formaldehyde ice is an intermediate product. The timescale of key evolutionary processes for formaldehyde, namely, oxidation of CH_3 and H_2CO , as well as accretion and evaporation, is fast, $\lesssim 10^2 - 10^3$ years (Tables 3–4).

As a result, the column densities of formaldehyde are only slightly affected by the turbulent transport (see Fig. 9). The same holds true for very abundant gas-phase CO and the H_2O ice. Their global chemical evolution is only slightly controlled by the surface chemistry, and the CRP/X-ray-irradiation becomes important only in the upper regions that do not contribute to the resulting vertical column densities. The 2D-mixing enables more efficient production of formaldehyde in the atmosphere (at $\approx 1 - 2 H_r$) thanks to enhanced abundances of CH_3 (see Sect. 4.2). The turbulent diffusion lowers the column densities of atomic oxygen, and increases the column densities of gas-phase water, carbon dioxide in all phases, and molecular oxygen. The pace of the conversion of atomic oxygen into other O-bearing species is partly governed by H_3^+ , which is sensitive to transport (see discussion in Sect. 4.1). The gas-phase water production involves this slow process and slow desorption, and thus gas-phase water becomes sensitive to the mixing. Finally, CO_2 and O_2 (and other multi-O species in the model) are the molecules which chemical evolution is at least partly determined by the slow surface reactions. This makes them sensitive to the turbulent mixing. Note also that the chemical

evolution of the CO₂ ice and, to a less degree, the CO ice, is influenced strongly by the radial mixing.

4.4. Nitrogen-containing molecules

Table 11
Key chemical processes: N-bearing species

Reaction	α [(cm ³) s ⁻¹]	β	γ [K]	t _{min} [yr]	t _{max} [yr]
HC ₅ N ice + hν _{CRP} → C ₄ H ice + CN ice	1.75(3)	0	0	1.00	5.00(6)
HCN + UV → CN + H	0.16(-8)	0	2.69	1.00	5.00(6)
HNC + UV → CN + H	0.55(-9)	0	2.00	1.00	5.00(6)
HNO + UV → NO + H	0.17(-9)	0	0.53	1.00	5.00(6)
OCN + UV → O + CN	1.00(-11)	0	2.00	1.00	5.00(6)
CN + grain → CN ice	1.00	0	0	1.00	5.00(6)
HCN + grain → HCN ice	1.00	0	0	1.00	5.00(6)
HNC + grain → HNC ice	1.00	0	0	1.00	5.00(6)
HNO + grain → HNO ice	1.00	0	0	1.00	5.00(6)
NO + grain → NO ice	1.00	0	0	1.00	5.00(6)
OCN + grain → OCN ice	1.00	0	0	1.00	5.00(6)
HC ₅ N + grain → HC ₅ N ice	1.00	0	0	1.00	5.00(6)
HCN ice → HCN	1.00	0	2.05(3)	1.00	5.00(6)
HNC ice → HNC	1.00	0	2.05(3)	1.00	5.00(6)
HC ₅ N ice → HC ₅ N	1.00	0	6.18(3)	1.00	5.00(6)
H ice + CN ice → HCN	1.00	0	0	1.00	5.00(6)
H ice + C ₅ N ice → HC ₅ N ice	1.00	0	0	1.00	5.00(6)
H ice + C ₅ N ice → HC ₅ N	1.00	0	0	28.60	5.00(6)
H ice + HC ₅ N ice → H ₂ C ₅ N ice	1.00	0	1.21(3)	1.00	5.00(6)
H ice + NO ice → HNO	1.00	0	0	1.00	5.00(6)
N ice + C ₅ H ice → HC ₅ N ice	1.00	0	0	1.00	5.00(6)
O ice + CN ice → OCN	1.00	0	0	4.18(2)	5.00(6)
O ice + HNO ice → NO + OH	1.00	0	0	1.00	5.00(6)
CH ₃ C ₅ N + H ⁺ → HC ₅ N + CH ₃ ⁺	0.20(-7)	-0.50	0	3.82	5.00(6)
HC ₅ N + H ⁺ → C ₅ HN ⁺ + H	0.40(-7)	-0.50	0	1.00	5.00(6)
HCN + H ⁺ → HCN ⁺ + H	0.28(-7)	-0.50	0	1.00	5.00(6)
HNC + H ⁺ → HCN + H ⁺	0.25(-7)	-0.50	0	1.00	5.00(6)
HCN ⁺ + H → HCN + H ⁺	0.37(-10)	0	0	1.00	5.00(6)
NO + C → CN + O	0.60(-10)	-0.16	0	1.00	5.00(6)
OCN + C → CN + CO	1.00(-10)	0	0	1.00	5.00(6)
CN + O ₂ → OCN + O	0.24(-10)	-0.60	0	1.00	5.00(6)
HNO + O → NO + OH	0.38(-10)	0	0	1.00	5.00(6)
NH ₂ + O → HNO + H	0.80(-10)	0	0	1.00	5.00(6)
C ₇ N + O → OCN + C ₆	0.40(-10)	0	0	1.00	5.00(6)
CN + OH → OCN + H	0.70(-10)	0	0	1.00	5.00(6)
HNO + H → NO + H ₂	0.45(-10)	0.72	3.29(2)	1.00	5.00(6)
N + CH → CN + H	0.17(-9)	-0.09	0	1.00	2.56(6)
N + CH ₂ → HNC + H	0.40(-10)	0.17	0	1.00	5.00(6)
N + HCO → OCN + H	1.00(-10)	0	0	1.00	5.00(6)
N + NO → N ₂ + O	0.30(-10)	-0.60	0	1.00	5.00(6)
N + OH → NO + H	0.75(-10)	-0.18	0	1.00	5.00(6)
C ₃ H ₂ N ⁺ + e ⁻ → HNC + C ₂ H	0.75(-7)	-0.50	0	1.00	5.00(6)
C ₃ HN ⁺ + e ⁻ → HCN + C ₂	0.30(-6)	-0.50	0	1.00	5.00(6)
C ₅ H ₂ N ⁺ + e ⁻ → HC ₅ N + H	0.15(-6)	-0.50	0	1.00	5.00(6)
C ₅ H ₃ N ⁺ + e ⁻ → HC ₅ N + H ₂	1.00(-6)	-0.30	0	7.48	5.00(6)
C ₆ H ₄ N ⁺ + e ⁻ → HC ₅ N + CH ₃	1.00(-6)	-0.30	0	1.00	5.00(6)
CH ₂ CN ⁺ + e ⁻ → HCN + CH	0.30(-6)	-0.50	0	1.00	5.00(6)
H ₂ CN ⁺ + e ⁻ → HCN + H	0.19(-6)	-0.65	0	1.00	5.00(6)
H ₂ CN ⁺ + e ⁻ → HNC + H	0.19(-6)	-0.65	0	1.00	5.00(6)
H ₂ NO ⁺ + e ⁻ → HNO + H	0.15(-6)	-0.50	0	1.00	5.00(6)
H ₂ CN ⁺ + e ⁻ → CN + H + H	0.92(-7)	-0.65	0	1.00	5.00(6)

Similar to the oxygen-bearing molecules, the observations of the N-bearing species provide useful diagnostics on the physical conditions and chemical state of the cosmic objects. The ammonia doublet lines are used to measure kinetic temperatures (e.g., Walmsley & Ungerechts 1983; Churchwell et al. 1990; Jijina et al. 1999), while the CN and HCN relative line strengths are sensitive to the UV flux (e.g., Bergin et al. 2003). The linear HC₃N and heavier cyanopolyyynes with large dipole moments serve as densitometers (e.g., Pratap et al. 1997), whereas OCN⁻ has been proposed as a carrier of the 4.62 μm absorption feature in inter-

stellar ices (Raunier et al. 2003; Bennett et al. 2010). In this Section we analyze in detail chemical and mixing processes responsible for the evolution of the neutral nitrogen-bearing species in protoplanetary disks.

There are 4 steadfast neutral N-bearing molecules (CN, HCN, HNC, NH₂), 2 ions (H₂CN⁺ and NH₄⁺) (Table 5). Their column densities in the laminar and fast mixing models differ by a factor of 3. The sensitive nitrogen species include 19 molecules (e.g., C₂N, C₃N,..., C₉N, HC₃N), 6 ions (e.g., NO⁺, N₂H⁺, CNC⁺), and 22 solid species (e.g., CH₂NH, HC₃N,..., HC₉N, CN, NO; Table 6). Their column densities are changed by up to 2 orders of magnitude by the tur-

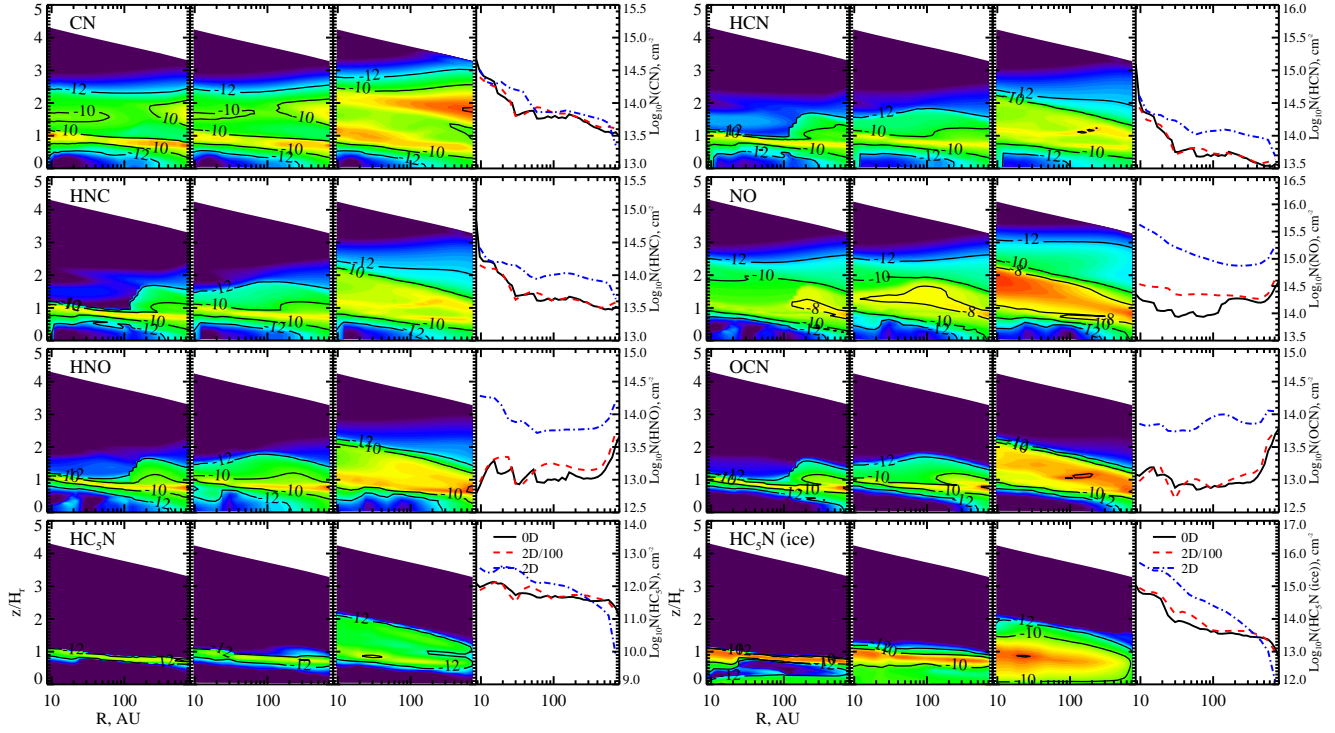


Figure 10. The same as in Fig. 7 but for the N-containing species. Results are shown for CN, HCN, HNC, NO, HNO, OCN, HC₅N, and HC₅N ice.

bulent transport. The N-bearing hypersensitive species are 4 molecules (C₇N, HC₇N, N₂O, and NO₂), N⁺, and 8 ices (e.g., CH₃C₃N, HNO, N₂, NO₂, etc.), see Table 7. The turbulent diffusion alters their column densities by up to 7 orders of magnitude (H₅C₃N ice). Similarly to hydrocarbons and oxygen-containing molecules, complex chains with multiple N, C, or H atoms are more strongly affected by the turbulent transport than chemically simpler species, though the trend is not that clear (e.g., NO₂, HNCO, N⁺, N₂O are the outliers). As Vasyunin et al. (2008) have found, nitrogen chemistry in disks involves a larger number of key reactions, including many exothermic neutral-neutral reactions, surface processes, compared to the chemistries of the O- and C-containing species. We have selected several most interesting nitrogen species for detailed chemical analysis.

In Fig. 10 the distributions of the relative molecular abundances and column densities at 5 Myr of CN, HCN, HNC, NO, HNO, OCN, HC₅N, and HC₅N ice calculated with the laminar and the 2D-mixing models are presented. The relative abundance distributions of the all considered species show a 3-layered structure, with peak concentrations in the molecular layers at $\approx 0.8 - 1 H_r$, with typical values of $10^{-10} - 10^{-8}$ (with respect to the total amount of hydrogen nuclei). The molecular layers of N-bearing molecules are narrow, $\approx 0.2 - 0.5 H_r$, similar to those of hydrocarbons, HCO⁺ and H₂CO (see Figs. 8 and 9). The photostable CN radical has a second molecular layer in the outer disk atmosphere, at $z \approx 1.8$ ($r \gtrsim 200$ AU), though it does not contribute much to the total CN column density. Note that HC₅N ice is also concentrated in the molecular layer, at ~ 1 pressure scale height.

Turbulent mixing does not affect column densities of steadfast CN, HCN, and HNC species (see 4th panels in Fig. 10). Nonetheless, their molecular layers are broadened by diffusion, and the second, upper molecular layer of CN becomes more prominent (compare 1st and 3rd panels in the Figure).

NO, HNO, OCN, HC₅N, and HC₅N ices are sensitive to the mixing, with their column densities increased by 2D-turbulent diffusion by up to a factor of 40 (cyanodiacetylene; Table 6). The corresponding abundance distributions are vertically extended up to the thicknesses of $\sim 0.5 - 1.5 H_r$, and enhanced by the transport by up to several orders of magnitude.

To better understand these result, we investigate the evolution of CN, HCN, HNC, NO, HNO, OCN, HC₅N, and the surface HC₅N in the two disk vertical slices at $r = 10$ and 250 AU (the laminar chemical model). The most important reactions responsible for the time-dependent evolution of their abundances in the midplane, the molecular layer, and the atmosphere are presented in Table 11, both for the inner and outer disk regions. The final list contains only top 20 reactions per region (midplane, molecular layer, atmosphere) for the entire 5 Myr time span, with all repetitions removed.

The evolution of cyanopolyyynes is tightly connected with the evolution of carbon chains discussed in Section 4.2. Their major production pathways in the gas include evaporation from icy mantles, neutral-neutral reaction of N with Renner-Teller hydrocarbons (C_nH), slow or slightly endothermic reaction of CN with C_{n-1}H₂ (e.g., CN + C₄H₂ \rightarrow HC₅N), and at later times dissociative recombination of their protonated analogs formed by the ion-molecule reactions with H₃⁺ (Table 11). The main removal pathways are the freeze-out at temperatures $\lesssim 70 - 170$ K, UV-photodissociation, reactive collisions with the ionized C, H, and He atoms. On dust surfaces, cyanopolyynne ices form either via addition of N to the frozen Renner-Teller hydrocarbons or through hydrogenation of the C_nN ices. The major destruction routes for the cyanopolyynne ices are photoevaporation, photoprocessing by the X-ray- or CRP-driven UV photons (e.g., HC₅N ice + hν_{CRP} \rightarrow C₄H ice + CN ice), and surface conversion to even more complex species (e.g., HC₅N ice + H ice \rightarrow H₂C₅N ice). In turn, dehydrogenated carbon chains with attached nitrogen atom are

produced in the gas and on the dust surfaces by rapid neutral-neutral reactions of N with the C_nH species, and dissociation of complex molecules with multiple C and N atoms (e.g., CH_3C_5N ice + $h\nu_{CRP} \rightarrow C_5N$ ice + CH_3 ice). Obviously, as in the case of complex carbon chains, characteristic timescales of the cyanopolyyne chemical evolution are regulated by the slow surface processes with τ_{chem} exceeding million years.

In contrast, chemical histories of CN, HCN, and HNC are closely related and governed by a small set of reactions. The production and destruction of CN proceeds entirely in the gas phase. The primal formation pathways are photodissociation of hydrogen cyanide and isocyanide, rapid barrierless neutral-neutral reactions of N with CH , C_2 , and C_2N , and NO with C (rate coefficients are $\sim 10^{-11} - 6 \cdot 10^{-10} \text{ cm}^3 \text{ s}^{-1}$), and dissociative recombination of $HCNH^+$ at later times ($t \gtrsim 10^2 - 10^4$ years), see Table 11. Another, less important formation pathway for CN is the neutral-neutral reaction between C and OCN leading to CN and CO. The destruction of CN is mostly caused by photodissociation, fast neutral-neutral reactions with N, O, OH, and O_2 , and freeze-out in the disk midplane at $T \lesssim 35 - 40$ K. In the atmosphere CN reacts with H^+ , forming CN^+ , which is converted back to CN by the charge transfer with atomic hydrogen. The fact that the CN chemistry involves only gas-phase routes implies its relatively short characteristic timescale, $\sim 10^3$ years (Tables 3–4). Only in the outer atmosphere $\tau_{chem}(CN) \gtrsim 10^5$ years, because the CN evolution there depends on the slow evolution of C_2H (see Fig. 8 and discussion in Sect. 4.2).

The key production route for gas-phase HCN and HNC are the neutral-neutral reaction of nitrogen atoms with CH_2 and dissociative recombination of $HCNH^+$ (Table 11). More energetically favorable isomer, HCN, is produced upon reactive collisions of ionized hydrogen with hydrogen isocyanide. The minor formation channels in the disk midplane are direct surface recombination of atomic hydrogen and cyanogen radical that leads to gas-phase HCN and H (with 5% probability), and the charge transfer reaction of H and HCN^+ . Due to their relatively large binding energies, thermal desorption of HCN and HNC does not occur until temperatures of $T \gtrsim 40$ K are reached. The major destruction routes for the gas-phase HCN and HNC include accretion onto the dust grains, the charge transfer reaction with H^+ , the ion-molecule reaction with C^+ leading to CNC^+ or C_2N^+ , and protonation reaction with H_3^+ , HCO^+ , and H_3O^+ (e.g., $HCN + HCO^+ \rightarrow HCNH^+ + CO$). Another important destruction channel for hydrogen (iso)cyanide in the upper disk layers at $\sim 1.5 - 2$ scale heights is photodissociation. The characteristic timescales of the HCN and HNC evolution are $\lesssim 10^3 - 10^4$ years in the molecular layer. Their chemical timescales exceed $10^5 - 10^6$ years in the midplane, where their evolution is partly controlled by the slow surface formation, and in the inner upper molecular layer/low atmosphere subject to the slow X-ray-driven dissociation of H_2 and release of oxygen from water and CO.

The evolution of NO, HNO, and OCN, similarly to that of CN, HCN, and HNC, is also governed by a set of rapid exothermic neutral-neutral reactions. The major formation pathways for nitrogen monoxide comprise reactive collisions of atomic nitrogen with hydroxyle, reactive collisions of atomic oxygen with nitrogen monohydride, gas-phase destruction of HNO by atomic oxygen, and, in the inner midplane, surface destruction of HNO by O, CH_2 and CH_3 , with products (NO and OH, CH_3 , or CH_4) directly injected into the gas. In the disk atmosphere NO is produced by the photo-

photodissociation of HNO. In the inner disk midplane a source of the NO gas is thermal desorption of the NO ice. The major removal processes for NO include photodissociation in the atmosphere, accretion onto the dust grains in the disk regions with $T \lesssim 30 - 35$ K, neutral-neutral reactions with atomic carbon and nitrogen (leading to CO and N_2), and charge transfer reactions with H^+ and C^+ . The characteristic timescale for NO is $\lesssim 10^3 - 10^4$ years in the molecular layer, and $\gtrsim 10^5 - 10^6$ years in the midplane, where its evolution is partly controlled by the surface processes. In the upper molecular layer at $r \sim 100$ AU the NO chemical timescale is again long, ~ 1 Myr, since it is related with the evolution of atomic oxygen that is slow at those disk heights.

The chemical evolution of nitric acid (HNO) is very similar to the evolution of NO. The major production terms for HNO are neutral-neutral reaction of atomic oxygen with nitrogen dihydride, and, in the warm molecular layer and the inner midplane, via surface hydrogenation of NO directly to the gas-phase. The evaporation of the solid HNO plays only a minor role for production of gas-phase HNO (in the laminar model). The major destruction terms for HNO include photodissociation in the atmosphere, accretion onto the dust grains in the disk regions with $T \lesssim 40 - 50$ K, neutral-neutral reactions with atomic hydrogen and oxygen (leading to NO), and ion-molecule reaction with H^+ (forming ionized NO and H_2). The distribution of the characteristic timescale for HNO over the disk is close to that of NO.

Finally, the chemical evolution of cyanate (OCN) is more diverse than that of NO and HNO. The key formation routes comprise of neutral-neutral reactions of CN with OH and O_2 , N and HNO, and oxidation reactions with abundant cyanopolyyynes, e.g. $C_7N + O \rightarrow OCN + C_6$. It can also be produced by direct surface recombination in O and CN ices. Similar to HNO, desorption of the solid OCN is not a key formation process for gas-phase cyanate (in the laminar model). The key removal routes include photodissociation in the atmosphere, sticking to the dust grains in the disk regions with $T \lesssim 50 - 60$ K, neutral-neutral reactions with atomic oxygen and carbon (leading to NO or CO), slow combustion reaction with O_2 (producing CO_2 and NO), and ion-molecule reaction with C^+ (forming ionized CO and CN). The characteristic timescale of the OCN evolution is $\lesssim 10^3 - 10^4$ years in the molecular layer, and $\gtrsim 10^5 - 10^6$ years in the inner and outer midplane, where its evolution is partly controlled by the surface processes. In the atmosphere the OCN chemical timescale increases from 10^4 till 10^6 years, similar to the CO_2 timescale shown in Fig. 2.

Consequently, column densities of CN, HCN, and HNC are not much affected by diffusion as their key evolutionary processes in their molecular layers proceed rapidly in the gas-phase (Fig. 10). As for many molecules in the model, the turbulent transport expands their molecular layers in vertical direction. Since the chemistry of CN involves C_2H , which abundances are increased by the mixing in the atmosphere at $z \gtrsim 2H_r$ (see Fig. 8 and discussion in Sect. 4.2), in the 2D-mixing case ($Sc = 1$) the second molecular layer of CN is formed. Similarly, the hydrogen cyanide and isocyanide evolution is related to the evolution of CH_2 , which is sensitive to the transport in the same upper disk region, though not as strong as ethynyl radical. The chemistry of the NO-containing species (e.g., NO, HNO, OCN) is sensitive to mixing as it depends on the evolution of O and O_2 that is in turn influenced by the transport, and since their production involves

minor slow surface routes. Moreover, thermal evaporation of these heavy species is inefficient, and thus photoevaporation of their ices becomes an important production pathways for the gas-phase counterparts. Vertical diffusive mixing allows more proficient evaporation of NO, HNO, and OCN ices in the warm molecular layer, enhancing their gas-phase abundances.

Finally, due to extreme importance of surface chemistry for the chemical evolution of cyanopolyynes, their abundances and column densities are increased by the turbulent mixing, albeit not as strongly as for some heavy hydrocarbons.

4.5. Sulfur-containing molecules

Table 12
Key chemical processes: S-bearing species

Reaction	α [(cm ³) s ⁻¹]	β	γ [K]	t _{min} [yr]	t _{max} [yr]
C ₃ S ice + hν _{CRP} → C ₂ ice + CS ice	1.50(3)	0	0	1.00	5.00(6)
CS + UV → C + S	0.98(−9)	0	2.43	1.00	5.00(6)
C ₂ S + UV → C ₂ + S	1.00(−10)	0	2.00	1.00	5.00(6)
H ₂ CS + UV → CS + H ₂	1.00(−9)	0	1.70	1.00	5.00(6)
H ₂ S + UV → HS + H	0.31(−8)	0	2.27	1.00	5.00(6)
OCS + UV → CO + S	0.37(−8)	0	2.07	1.00	5.00(6)
SO ₂ + UV → SO + O	0.19(−8)	0	2.38	1.00	5.00(6)
CS + grain → CS ice	1.00	0	0	1.00	5.00(6)
C ₂ S + grain → C ₂ S ice	1.00	0	0	1.00	5.00(6)
C ₃ S + grain → C ₃ S ice	1.00	0	0	1.00	5.00(6)
OCS + grain → OCS ice	1.00	0	0	1.00	5.00(6)
SO ₂ + grain → SO ₂ ice	1.00	0	0	1.00	5.00(6)
H ₂ S + grain → H ₂ S ice	1.00	0	0	1.00	5.00(6)
H ₂ CS + grain → H ₂ CS ice	1.00	0	0	1.00	5.00(6)
CS ice → CS	1.00	0	1.90(3)	28.60	5.00(6)
C ₂ S ice → C ₂ S	1.00	0	2.70(3)	1.00	5.00(6)
C ₃ S ice → C ₃ S	1.00	0	3.50(3)	1.00	5.00(6)
C ₂ S ice + C ice → C ₃ S ice	1.00	0	0	1.00	5.00(6)
H ice + HS ice → H ₂ S	1.00	0	0	1.00	5.00(6)
O ice + CS ice → OCS	1.00	0	0	1.00	5.00(6)
O ice + SO ice → SO ₂	1.00	0	0	1.00	5.00(6)
S ice + CO ice → OCS	1.00	0	0	1.00	5.00(6)
CS + H ⁺ → CS ⁺ + H	0.18(−7)	−0.50	0	1.00	5.00(6)
C ₂ S + H ⁺ → C ₂ S ⁺ + H	0.11(−7)	−0.50	0	1.00	5.00(6)
H ₂ S + H ⁺ → H ₂ S ⁺ + H	0.38(−8)	−0.50	0	1.00	5.00(6)
H ₂ CS + H ⁺ → H ₂ CS ⁺ + H	0.64(−8)	−0.50	0	1.00	5.00(6)
OCS + H ⁺ → HS ⁺ + CO	0.65(−8)	−0.50	0	1.00	5.00(6)
SO ₂ + C ⁺ → SO ⁺ + CO	0.20(−8)	−0.50	0	1.00	5.00(6)
SO ₂ + H ₃ ⁺ → HSO ₂ ⁺ + H ₂	0.37(−8)	−0.50	0	1.96	5.00(6)
O + SO → SO ₂	0.32(−15)	−1.60	0	1.00	5.00(6)
O + HCS → OCS + H	0.50(−10)	0	0	1.00	5.00(6)
S + CO → OCS	0.16(−16)	−1.50	0	1.00	5.00(6)
S + CH ₃ → H ₂ CS + H	0.14(−9)	0	0	1.00	5.00(6)
SO ₂ + C → CO + SO	0.70(−10)	0	0	1.00	5.00(6)
OH + SO → SO ₂ + H	0.86(−10)	0	0	1.00	5.00(6)
C ₃ S ⁺ + e [−] → C ₂ S + C	1.00(−7)	−0.50	0	1.00	5.00(6)
C ₃ S ⁺ + e [−] → CS + C ₂	1.00(−7)	−0.50	0	1.00	1.20(4)
C ₄ S ⁺ + e [−] → C ₂ S + C ₂	1.00(−7)	−0.50	0	1.00	5.00(6)
H ₃ CS ⁺ + e [−] → H ₂ CS + H	0.30(−6)	−0.50	0	1.00	5.00(6)
H ₃ S ⁺ + e [−] → H ₂ S + H	0.30(−6)	−0.50	0	1.00	5.00(6)
HC ₂ S ⁺ + e [−] → C ₂ S + H	0.15(−6)	−0.50	0	1.00	5.00(6)
HCS ⁺ + e [−] → CS + H	0.18(−6)	−0.57	0	1.00	5.00(6)
HOCS ⁺ + e [−] → CS + OH	0.20(−6)	−0.50	0	1.00	5.00(6)
OCS ⁺ + e [−] → CS + O	0.48(−7)	−0.62	0	1.00	1.20(4)
H ₂ CS ⁺ + e [−] → H ₂ CS	0.11(−9)	−0.70	0	14.60	5.00(6)
H ₂ S ⁺ + e [−] → H ₂ S	0.11(−9)	−0.70	0	1.00	5.00(6)
H ₃ CS ⁺ + e [−] → CS + H + H ₂	0.30(−6)	−0.50	0	1.00	5.00(6)
C ₃ S ⁺ + grain(−) → C ₂ S + C + grain(0)	0.33	0	0	3.82	5.00(6)
HOCS ⁺ + grain(−) → CS + OH + grain(0)	0.50	0	0	3.82	5.00(6)
H ₃ CS ⁺ + grain(−) → H ₂ CS + H + grain(0)	0.50	0	0	3.82	5.00(6)
HC ₂ S ⁺ + grain(−) → C ₂ S + H + grain(0)	0.50	0	0	1.96	5.00(6)

In this Section we analyze in detail chemical and mixing processes responsible for the evolution of sulfur-bearing species in protoplanetary disks. The chemistry of sulfur-bearing molecules is the least understood in astrochemistry. As other heavy elements, sulfur is depleted from the gas, but the magnitude of the effect and in which form sulfur is bound

is not yet clearly determined (e.g., Lodders 2003; Flynn et al. 2006; Goicoechea et al. 2006). Moreover, many processes and reaction rate data for the S-bearing species are lacking accurate laboratory measurements or theoretical foundations, leading to considerable uncertainties in modeled abundances (e.g., Vasyunin et al. 2008; Wakelam et al. 2010b). Thus, results in this subsection should be taken with special care. So far there are only two sulfur-containing molecules detected in

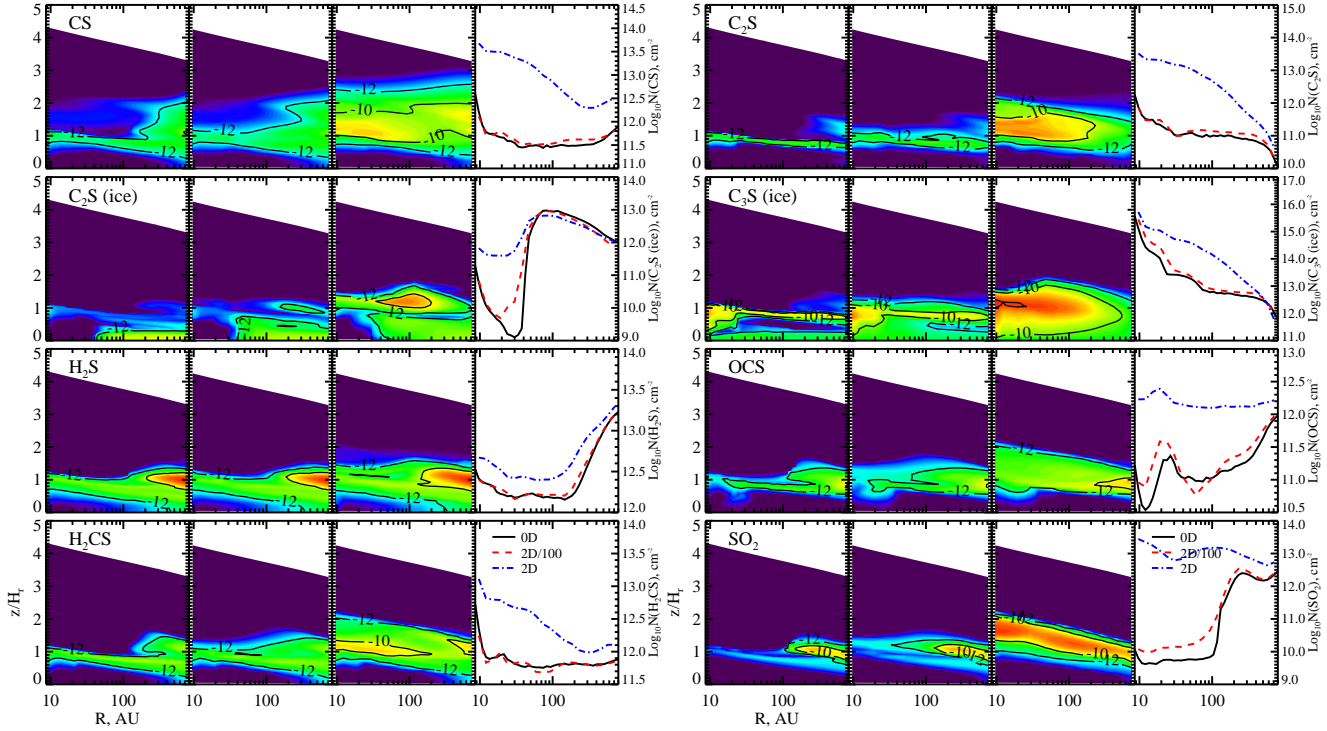


Figure 11. The same as in Fig. 7 but for the S-containing species. Results are shown for CS, C_2S , C_2S ice, C_3S ice, H_2S , OCS, H_2CS , and SO_2 .

disks, namely, CS (e.g., Dutrey et al. 1997) and, recently, SO (Fuente et al. 2010). In the interstellar medium and the shells of AGB stars other species have been discovered, e.g. C_2S , C_3S , and H_2CS (e.g., Cernicharo et al. 1987; Yamamoto et al. 1987; Irvine et al. 1989). So, here we restrict ourselves with discussion of neutral species only.

There are 2 steadfast neutral S-bearing molecules (H_2S and HCS), 5 ices (HS , H_2S , H_2CS , S , and S_2), and no ions (Table 5). Their column densities in the laminar and the fast 2D-mixing model differ by a factor of ≤ 3 . The sensitive sulfur-bearing species include 7 gas-phase molecules (e.g., CS, H_2CS , H_2S_2 , HS, S), 2 ions (S^+ and SO^+), and 7 ices (e.g., CS, C_3S , C_4S , H_2S_2 , SO ; Table 6). Their column densities are changed by up to 2 orders of magnitude by the turbulent transport. Among hypersensitive species (Table 7) are 4 gas-phase molecules (C_2S , C_3S , SO , and SO_2), no ions, and 3 ices (C_2S , NS , and SiS). The turbulent diffusion alters their column densities by up to a factor of 7 000 (SO_2 ice). Similarly to hydrocarbons and oxygen-containing molecules, complex S-chains with multiple carbon atoms or oxygen are more strongly affected by the turbulent transport than chemically simpler species. Unlike the case of C- and N-bearing species, there is no trend that the concentrations of the sulfur-bearing ices are stronger altered by the transport than the abundances of their gas-phase analogs.

In Fig. 11 the distributions of the relative molecular abundances and column densities at 5 Myr of CS, C_2S , C_2S ice, C_3S ice, H_2S , OCS, H_2CS , and SO_2 calculated with the laminar and the 2D-mixing models are shown. In the laminar model the relative abundance distributions of the gas-phase species show a 3-layered structure, with peak concentrations in the molecular layers at $\approx 0.8 - 1 H_r$. In contrast, the C_2S and C_3S ices are more concentrated toward the disk midplane and the bottom of the molecular layer, with typical abundances of $10^{-12} - 10^{-10}$. The molecular layers of gas-phase sulfur-

bearing molecules have various thicknesses, from $\approx 0.05 H_r$ for C_2S and up to $\sim 2 H_r$ for CS, and are not as pronounced as for carbon-, oxygen- and nitrogen-bearing species (see Figs. 8–10). Their typical peak relative abundances are only $10^{-12} - 10^{-10}$, though in the outer molecular layer the H_2S abundances are as high as $\sim 10^{-8}$.

Among the above molecules, only H_2S is steadfast (see 4th panels in Fig. 11). The mixing enhances the H_2S concentration in the upper molecular layer at $z \gtrsim 1.3 H_r$ that does not contribute to the total column density (compare 1st and 3rd panels in the Figure). The CS, C_2S , C_2S ice, C_3S ice, OCS, H_2CS , and SO_2 are sensitive and hypersensitive to the mixing. The corresponding molecular layers are vertically broadened up to $\approx 2 H_r$, and strongly molecularly enriched by several orders of magnitude.

To better understand these results, we investigate the evolution of CS, C_2S , C_2S ice, C_3S ice, H_2S , OCS, H_2CS , and SO_2 in the two disk vertical slices at $r = 10$ and 250 AU (the laminar chemical model). The most important reactions responsible for the time-dependent evolution of their abundances in the midplane, the molecular layer, and the atmosphere are presented in Table 12, both for the inner and outer disk regions. The final list contains top 20 reactions per region (midplane, molecular layer, atmosphere) for the entire 5 Myr time span, with all repetitions removed.

The chemical evolution of hydrogen sulfide in the atmosphere begins with radiative association of ionized sulfur and H_2 , leading to H_2S^+ that slowly radiatively recombines into H_2S . The major destruction reactions in the atmosphere is photodissociation and rapid ion-molecule reaction with C^+ forming protonated CS and H (75%) or H_2S^+ and C (25%), and charge transfer reaction with H^+ . In the molecular layer and midplane hydrogen sulfide is initially produced as in the atmosphere, but after 1–100 years the top formation pathway for gas-phase H_2S is a direct surface recombination of HS and

H ices. This is caused by a relatively large binding energy of H₂S that prevents H₂S ice to return to the gas phase unless temperatures exceed about 45–50 K. The HS radical is formed via neutral-neutral reaction of S with OH, and also via direct surface recombination of H and S. The major destruction pathways for H₂S in the molecular layer and midplane are accretion onto dust grain surfaces, ion-molecule reactions with HCO⁺ and H₃⁺ (leading to H₃S⁺), and charge transfer reaction with atomic hydrogen. The characteristic timescale of the H₂S evolution is short in the midplane and molecular layer, $\lesssim 10 - 10^4$ years since its initial production and freeze-out are relatively fast. Later, accretion is balanced out by the direct surface recombination, while desorption of the H₂S is not significant. In the atmosphere the H₂S reaches a quasi steady-state within $10^4 - 10^6$ years, which is determined by the slow evolution of H₂, H₃⁺, and H₃⁺ (see discussion in Sect. 4.1).

The chemical evolution of CS proceeds entirely in the gas phase. The carbon monosulfide is synthesized by dissociative recombination of HCS⁺, C₂S⁺, C₃S⁺, HOCS⁺, and H₃CS⁺ on electrons or negatively charged grains in the inner midplane, and via desorption of the CS ice at $T \gtrsim 35 - 40$ K. The major destruction pathways are photodissociation in the atmosphere, depletion in the molecular layer and the midplane, slow endothermic oxidation reaction (CS + O → CO + S), charge transfer with ionized hydrogen atoms, and ion-molecule reactions with primal ions, e.g. HCO⁺, H₃O⁺, and H₃⁺, leading to HCS⁺ (Table 12). In turn, the protonated carbon monosulfide is initially synthesized through an ion-molecule destruction of H₂ by C⁺. The C₂S⁺ is produced either by an ion-molecule reaction of ethynyl radical with ionized atomic sulfur or via charge transfer reactions of C₂S with H⁺ and C⁺. The C₃S⁺ chemistry is similar to that of C₂S⁺, with the production pathway that involves C₃H instead of ethynyl. The HOCS⁺ is protonated OCS, and is formed via ion-molecule reactions of OCS with dominant polyatomic ions (H₃⁺, HCO⁺, etc.). Finally, H₃CS⁺ is synthesized via protonation of H₂CS and via ion-molecule reactions of ionized sulfur or HS⁺ with methane. The steady-state for CS is attained at about $10^2 - 10^4$ years in the lower molecular layer/upper midplane, and later in other disk parts. While the CS chemistry does not include surface processes directly, it is related with the evolution of C₂S⁺, C₃S⁺, and HOCS⁺, and, thus, their chemical “parents”, namely C₂S, C₃S, and OCS. The latter molecules are partly synthesized via surface reactions, making their evolution slow in the cold midplane.

The chemical evolution of all the C_nS species in the model ($n \leq 4$) is well coupled. For example, like in the case of CS, major formation channels for gas-phase C₂S include dissociative recombination of C₃S⁺, C₄S⁺, HC₂S⁺, and HC₃S⁺ on negatively charged grains in the inner midplane and electrons. The HC₂S⁺ and HC₃S⁺ ions are formed later in the disk by protonation of C₂S and C₃S. The binding energy adopted for C₂S is 2 700 K, and higher for more massive carbon chain sulfides, which precludes effective thermal desorption of their ices in the disk midplane and the molecular layer beyond 10 AU. The major destruction channels for C₂S are photodissociation, accretion onto dust grains, charge transfer reactions with H⁺ and C⁺, and protonation by abundant polyatomic ions (leading to HC₂S⁺). The evolution of the C₂S ice is significantly simpler. It involves only 3 major processes: accretion of the gas-phase C₂S, surface reaction of frozen atomic carbon with the C₂S ice producing the C₃S ice, and photodissociation of the C₂S ice by the CRP/X-ray-induced UV photons (lead-

ing to C and CS ices). The evolution of the C₃S ice includes its surface synthesis from C₂ and C, accretion of gas-phase C₃S, and photodestruction to the C₂ and CS ices. Consequently, the characteristic chemical timescales for gas-phase and, particularly, for surface C_nS molecules are long, $\tau_{\text{chem}} \gtrsim 10^6$ years.

Thioformaldehyde, H₂CS, like CS and H₂CO, is synthesized in the gas. Its major production routes consist of neutral-neutral reaction between S and CH₃, and dissociative recombination of protonated H₂CS at later times. The key destruction routes are photodissociation, accretion onto dust grains at $T \lesssim 45 - 50$ K, charge transfer reaction with ionized atomic hydrogen, ion-molecule reaction with ionized atomic carbon, and proton addition in reactive collisions with HCO⁺, H₃⁺, etc. The distribution of the H₂CS characteristic timescale over the disk closely resembles $\tau_{\text{chem}}(\text{CS})$.

The chemical evolution of carbonyl sulfide (OCS) begins with its formation upon oxidation of HCS and via radiative association of S and CO. At later times OCS is also produced by the direct surface recombination of the S and CO ices, and the CS and O ices. The destruction of OCS involves photodissociation in the disk atmosphere, accretion onto dust in the molecular layer and the midplane, and ion-molecule reactions with ionized C and H (leading to either CS⁺ and CO or HS⁺ and CO). The protonation of OCS by the polyatomic ions leads to HOCS⁺, which dissociatively recombines into OCS and H (50%) or CS and H (50%). The characteristic timescale for carbonyl sulfide is $\lesssim 10^2 - 10^6$ years in the disk midplane, $\sim 10^3 - 10^4$ years in the lower molecular layer, and $\gtrsim 10^4 - 10^6$ elsewhere in the disk.

Finally, sulfur dioxide (SO₂) is synthesized by exothermic neutral-neutral reaction between SO and OH, slow radiative association of SO and O, and the same reaction catalyzed by dust grains, with SO₂ directly desorbed back to the gas (with 5% probability). Its major removal channels are photodissociation, freeze-out in disk regions with $T \lesssim 60 - 80$ K, neutral-neutral reaction with atomic carbon (leading to SO and CO), and ion-molecule reaction with C⁺ (producing SO⁺ and CO). Later a quasi-equilibrium cycling of SO₂ prevails, which includes protonation of sulfur dioxide by abundant polyatomic ions (H₃⁺, HCO⁺) followed by dissociation recombination back to SO₂ with the 66% probability. In turn, sulfur monoxide (SO) is produced by slow combustion of S, neutral-neutral reactions between S and OH and O with HS, and direct surface reaction of the HS and O ices. Consequently, the characteristic chemical timescale of SO₂ is governed by the slow evolution of molecular oxygen due to surface processes (see Section 4.3), and exceeds 1 Myr in the disk midplane, and $10^4 - 10^5$ years in the molecular layer.

Since chemical network for S-bearing species, especially complex chains, in our model is more limited than that for the N- and C-containing molecules, the turbulent transport enhances abundances and column densities even for transient S-species. All species considered above either formed via surface reactions or their synthesis involves surface-produced radicals, and their chemical evolution proceed slower than the mixing (see Fig. 11). As for many molecules in the model, the turbulent transport expands their molecular layers in vertical direction. Complex S-ices are more readily produced in the mixing case as their formation is based on heavy radicals, which become mobile at $T \gtrsim 20 - 40$ K. Also, in the mixing model photodissociation of these ices is more effective (see a peak in the relative abundances of C₂S ice at $r \sim 100$ AU, $z \sim 1.5H_r$). The diffusive transport most strongly increases

concentration of SO_2 molecules by producing more molecular oxygen needed for its synthesis. For SO_2 , its radial distribution becomes sensitive to the transport. The least affected species is H_2S (as well as HCS, and ices of S, HS, and H_2S)

as its characteristic evolutionary timescale is shorter than the mixing timescale in the disk region where it is most abundant (see Tables 3–4).

4.6. Complex organic molecules

Table 13
Key chemical processes: organic species

Reaction	α [(cm^3) s^{-1}]	β	γ [K]	t_{\min} [yr]	t_{\max} [yr]
CH_2CO ice + $\text{h}\nu_{\text{CRP}}$ \rightarrow CH_2 ice + CO ice	9.15(2)	0	0	1.00	5.00(6)
CH_2CO ice + $\text{h}\nu_{\text{CRP}}$ \rightarrow C_2 ice + H_2O ice	4.07(2)	0	0	1.96	5.00(6)
CH_3CHO ice + $\text{h}\nu_{\text{CRP}}$ \rightarrow CH_3 ice + HCO ice	5.25(2)	0	0	1.96	5.00(6)
CH_3CHO ice + $\text{h}\nu_{\text{CRP}}$ \rightarrow CH_4 ice + CO ice	5.25(2)	0	0	1.96	5.00(6)
CH_3OH ice + $\text{h}\nu_{\text{CRP}}$ \rightarrow CH_3 ice + OH ice	1.50(3)	0	0	1.00	5.00(6)
CH_3OH ice + $\text{h}\nu_{\text{CRP}}$ \rightarrow H_2CO ice + H_2 ice	3.17(3)	0	0	1.00	5.00(6)
$\text{C}_2\text{H}_5\text{OH}$ ice + $\text{h}\nu_{\text{CRP}}$ \rightarrow CH_3CHO ice + H_2 ice	6.85(2)	0	0	2.34(4)	5.00(6)
HCOOH ice + $\text{h}\nu_{\text{CRP}}$ \rightarrow CO_2 ice + H ice + H ice	6.50(2)	0	0	1.00	5.00(6)
HCOOH ice + $\text{h}\nu_{\text{CRP}}$ \rightarrow HCO ice + OH ice	2.49(2)	0	0	3.82	5.00(6)
HNCO ice + $\text{h}\nu_{\text{CRP}}$ \rightarrow NH ice + CO ice	6.00(3)	0	0	1.00	5.00(6)
CH_3OH ice + UV \rightarrow H_2CO ice + H_2 ice	0.72(−9)	0	1.72	1.00	5.00(6)
$\text{C}_2\text{H}_5\text{OH}$ ice + UV \rightarrow CH_3CHO ice + H_2 ice	0.13(−9)	0	2.35	4.18(2)	5.00(6)
HCOOH ice + UV \rightarrow HCO ice + OH ice	0.28(−9)	0	1.80	1.00	5.00(6)
HNCO + $\text{h}\nu_{\text{CRP}}$ \rightarrow NH + CO	6.00(3)	0	0	1.00	5.00(6)
CH_3CHO + UV \rightarrow CH_3CHO^+ + e^-	0.26(−9)	0	2.28	1.00	5.00(6)
CH_3CHO + UV \rightarrow CH_4 + CO	0.34(−9)	0	1.52	1.00	5.00(6)
CH_3CHO + UV \rightarrow CH_3 + HCO	0.34(−9)	0	1.52	1.00	5.00(6)
HCOOH + UV \rightarrow HCOOH^+ + e^-	0.17(−9)	0	2.59	1.00	5.00(6)
HCOOH + UV \rightarrow HCO + OH	0.28(−9)	0	1.80	1.00	5.00(6)
CH_2CO + grain \rightarrow CH_2CO ice	1.00	0	0	1.00	5.00(6)
HCOOH + grain \rightarrow HCOOH ice	1.00	0	0	1.00	5.00(6)
HNCO + grain \rightarrow HNCO ice	1.00	0	0	1.00	5.00(6)
CH_2CO ice \rightarrow CH_2CO	1.00	0	2.20(3)	1.00	5.00(6)
CH_3CHO ice \rightarrow CH_3CHO	1.00	0	2.87(3)	1.00	5.00(6)
HNCO ice \rightarrow HNCO	1.00	0	2.85(3)	1.00	5.00(6)
H ice + CH_2OH ice \rightarrow CH_3OH ice	1.00	0	0	1.00	5.00(6)
H ice + HC_2O ice \rightarrow CH_2CO ice	1.00	0	0	1.00	5.00(6)
H ice + OCN ice \rightarrow HNCO ice	1.00	0	0	1.00	5.00(6)
H ice + OCN ice \rightarrow HNCO	1.00	0	0	1.00	5.00(6)
OH ice + CH_3 ice \rightarrow CH_3OH ice	1.00	0	0	1.00	5.00(6)
OH ice + HCO ice \rightarrow HCOOH ice	1.00	0	0	1.09(2)	5.00(6)
HCOOH + H^+ \rightarrow HCOOH^+ + H	0.28(−8)	-0.50	0	1.00	5.00(6)
HNCO + H^+ \rightarrow NH_2^+ + CO	0.15(−7)	-0.50	0	1.00	5.00(6)
CH_3CHO + H_3^+ \rightarrow $\text{CH}_3\text{CH}_2\text{O}^+$ + H_2	0.62(−8)	-0.50	0	1.00	5.00(6)
CH_3CHO + HCO^+ \rightarrow $\text{CH}_3\text{CH}_2\text{O}^+$ + CO	0.25(−8)	-0.50	0	1.00	5.00(6)
HCOOH + H_3^+ \rightarrow HCO^+ + H_2O + H ₂	0.23(−8)	-0.50	0	1.00	5.00(6)
HCOOH + HCO^+ \rightarrow CH_3O_2^+ + CO	0.13(−8)	-0.50	0	1.00	5.00(6)
O + C_2H_5 \rightarrow CH_3CHO + H	0.13(−9)	0	0	1.00	5.00(6)
OH + H_2CO \rightarrow HCOOH + H	0.20(−12)	0	0	1.00	5.00(6)
$\text{CH}_3\text{CH}_2\text{O}^+$ + e^- \rightarrow CH_3CHO + H	0.15(−6)	-0.50	0	1.00	5.00(6)
CH_3O_2^+ + e^- \rightarrow HCOOH + H	0.15(−6)	-0.50	0	1.00	5.00(6)
$\text{CH}_3\text{CH}_2\text{O}^+$ + grain(−) \rightarrow CH_3CHO + H + grain(0)	0.20	0	0	55.90	5.00(6)
CH_3O_2^+ + grain(−) \rightarrow HCOOH + H + grain(0)	0.50	0	0	1.00	5.00(6)
CH_3CHO + grain \rightarrow CH_3CHO ice	1.00	0	0	1.00	5.00(6)
CH_3OH + grain \rightarrow CH_3OH ice	1.00	0	0	1.00	5.00(6)

The presence of amino acids and other complex organics in the early Solar system is a well-established through detailed mass-spectrometry of carbonaceous meteorites (e.g., Glavin et al. 2010), via analysis of the cometary dust sampled by the *Giotto* spacecraft in the Halley comet (e.g., Jessberger et al. 1988), and the recent identification of glycine in the *Stardust* cometary dust samples (Elsila et al. 2009). The ground-based search for simple gas-phase organic species, such as methanol and formic acid, in nearby protoplanetary disks with radiotelescopes have so far been fruitless, though formaldehyde has been detected in DM Tau (e.g., Dutrey et al. 2007a) and LkCa 15 (Aikawa et al. 2003). The simple organic

ices, e.g. HCOOH ice, has been identified in the *Spitzer* spectra of several low-mass Class I/II objects (e.g., Zasowski et al. 2009). In contrast, rich organic gas-phase molecules have been detected in hot massive cores and corinos, where conditions are appropriate for steady sublimation and production of heavy complex ices (e.g., Belloche et al. 2008; Garrod et al. 2008). Nowadays synthesis of complex organics in cosmic objects is thought to proceed solely via surface processes, such as photoproduction of reactive radicals by high-energy irradiation of complex precursors and their surface recombination at elevated temperatures, (e.g., Herbst & van Dishoeck 2009). In this Section we analyze in detail chemical processes responsible for the formation and destruction of the complex organic species in protoplanetary disks. These are meant to

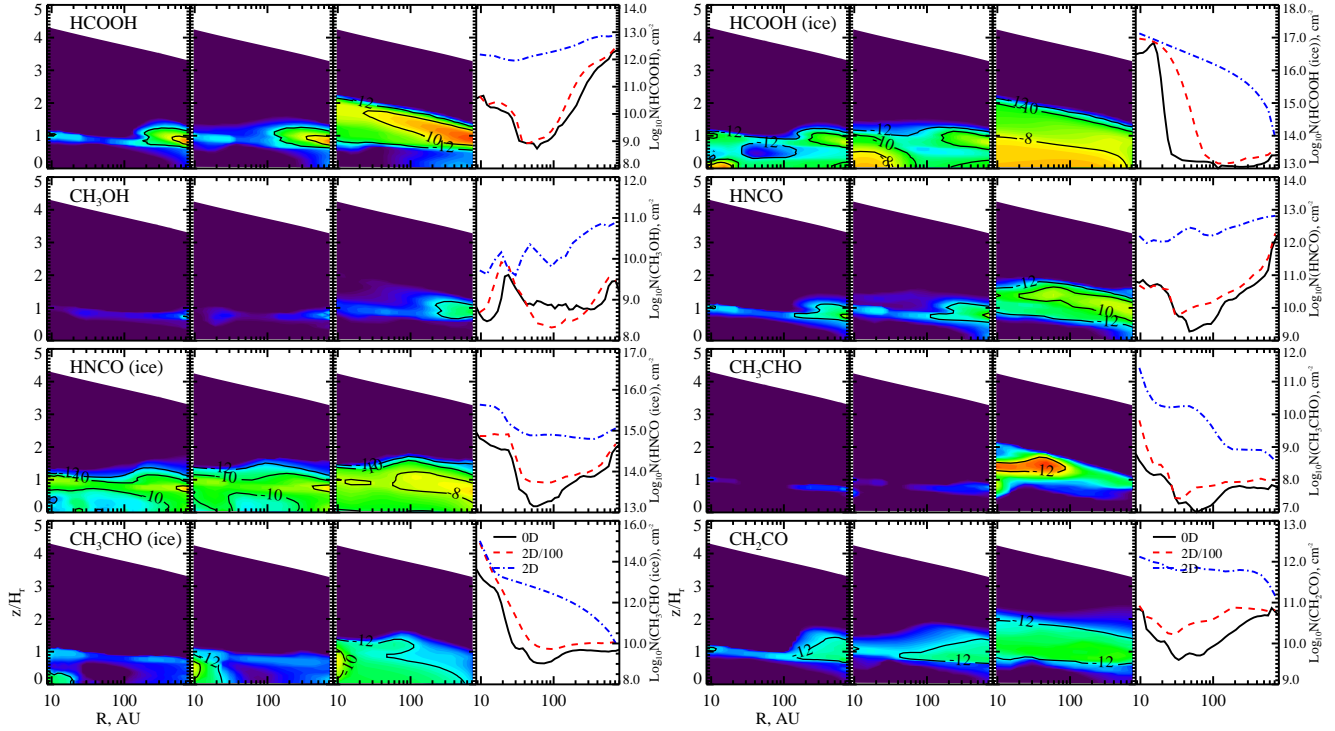


Figure 12. The same as in Fig. 7 but for the complex (organic) molecules. Results are shown for HCOOH, HCOOH ice, CH₃OH, HNCO, HNCO ice, CH₃CHO, CH₃CHO ice, and CH₂CO.

be polyatomic neutral molecules consisting of at least several H, C, and O atoms, and heavier elements.

There is a single organic species insensitive to the turbulent diffusion, namely, formaldehyde (see Sect. 4.3). The transport-sensitive organic species include 2 gas-phase molecules (CH₂CO and HNCO) and 5 ices (CH₂CO, HNCO, CH₃OH, H₂CO, NH₂CHO; Table 6). Their column densities are changed by up to 2 orders of magnitude. One gas-phase molecule (HCOOH) and 3 ices (HCOOH, H₂C₃O, and CH₃CHO) are among hypersensitive species in Table 7. The turbulent diffusion alters their column densities by up to a factor of 3 000 (solid formic acid). The chemical evolution of all the considered organic species is influenced by the transport as their major production and removal routes require surface processes.

In Fig. 12 the distributions of the relative molecular abundances and column densities at 5 Myr of HCOOH, HCOOH ice, CH₃OH, HNCO, HNCO ice, CH₃CHO, CH₃CHO ice, and CH₂CO calculated with the laminar and the 2D-mixing models are presented. In the laminar model the relative abundance distributions of the gas-phase species show a 3-layered structure, with very narrow molecular layers located at $\approx 0.8 - 1 H_r$. Note that their abundances and column densities are substantially lower than those of simpler C- or O-bearing species considered above, so that some heavy organic species are not included in Tables 5–7. The HCOOH, HNCO, and CH₂CO molecular layers are wider beyond ~ 200 AU, and have higher abundances. Remarkably, abundance distributions of complex ices are maximum either at the bottom of the molecular layer (HNCO ice, HCOOH ice) or in the inner warm midplane (CH₃CHO ice, HCOOH ice). The overall tendency can be easily explained as heavy ices are hard to evaporate thermally, so photoevaporation is necessary, while gas-phase organic molecules are rather photofragile. For efficient production of heavy ices surface mobility of radicals

(O, C, CH, etc.) necessitates warm temperatures ($T \gtrsim 30$ K) and/or photoprocessing of their precursor molecules by the X-ray/CRP-induced UV photons.

To better understand these results, we investigate the evolution of HCOOH, HCOOH ice, CH₃OH, HNCO, HNCO ice, CH₃CHO, CH₃CHO ice, and CH₂CO in two disk vertical slices at $r = 10$ and 250 AU (the laminar chemical model). The most important reactions responsible for the time-dependent evolution of their abundances in the midplane, the molecular layer, and the atmosphere are presented in Table 13, both for the inner and outer disk regions. The final list contains only top 25 reactions per region (midplane, molecular layer, atmosphere) for the entire 5 Myr time span, with all repetitions removed.

The chemical evolution of formic acid (HCOOH) starts with a single production channel via dissociative recombination of CH₃O₂⁺ either on electrons or negatively charged grains (Table 13). In turn, protonated formic acid is produced by radiative association of HCO⁺ and H₂O, and by ion-molecule reaction of methane with ionized molecular oxygen. The primal removal channels for HCOOH are photodissociation and photoionization, depletion onto dust grains at $T \lesssim 100 - 120$ K, charge transfer with ionized atomic hydrogen, and protonation by abundant polyatomic ions (HCO⁺, H₃⁺, H₃O⁺). The HCOOH ice is essentially synthesized by accretion of gas-phase formic acid, and destroyed by secondary UV photons in the disk midplane and molecular layer, and photoevaporation. The surface as well as gas-phase formation of HCOOH via neutral-neutral reaction of OH and H₂CO is only a minor channel in the laminar model. Consequently, the distribution of evolutionary timescales for gas-phase and surface HCOOH is similar and dominated by $\tau_{\text{chem}} \gtrsim 10^5$ years.

Gas-phase methanol (CH₃OH) is produced by direct surface recombination of frozen H and CH₂OH as well as frozen OH and CH₃, evaporation of methanol ice, dissociative re-

combination of protonated methanol, and dissociative recombination of $\text{H}_5\text{C}_2\text{O}_2^+$ (minor route). Its key removal pathways are surface accretion in the disk regions with $T \lesssim 100 - 120$ K, photodissociation and photoionization, and protonation by the dominant polyatomic ions. On dust surfaces methanol is produced via a sequence of hydrogenation reactions, starting from the CO ice, and is photodissociated by the UV radiation. Similarly to HCOOH, the characteristic chemical timescale for methanol is fully controlled by the slow surface chemistry ($\tau_{\text{chem}} \gtrsim 10^5$ years).

The chemical evolution of the isocyanic acid (HNCO) is also dominated by surface processes. In the gas-phase it is produced either by evaporation of HNCO ice at $T \lesssim 50 - 60$ K or by direct surface recombination of surface H and OCN. The major gas-phase destruction pathways are accretion to grains in the midplane and the molecular layer, and ion-molecule reaction with H^+ (leading to NH_2^+ and CO; Table 13). The HNCO ice is produced by the surface reaction involving H and OCN, re-accretion of the HNCO gas, and destroyed by the UV. Their characteristic timescales alike those of HCOOH and methanol.

The chemistry of acetaldehyde (CH_3CHO) involves gas-phase production by reactive collisions between O and C_2H_5 , accretion to dust grains at $T \lesssim 50 - 60$ K, and desorption at $T \lesssim 60$ K, and removal via charge transfer reactions with C^+ and ion-molecule reactions with C^+ , H_3^+ , and H_3O^+ . At later times acetaldehyde is re-produced from its protonated analog by dissociative recombination (albeit with low probability). The frozen acetaldehyde is synthesized by accretion of gas-phase CH_3CHO , via surface recombination of CH_3 and HCO ices, and destroyed by the UV-dissociation. As for other complex organics, the chemical timescale for acetaldehyde is typically longer than 1 Myr in the disk.

Finally, the gas-phase ethenone (CH_2CO) is produced via oxidation of C_2H_3 , direct surface recombination of the H and HC_2O ices, and dissociative recombination of protonated ethenone. Thermal evaporation of ethenone ice is effective when dust temperatures exceed ~ 100 K. Key removal channels include photodissociation and photoionization, freeze-out in the midplane and the molecular layer, charge transfer reaction with C^+ and H^+ , and, at later times, protonation by polyatomic ions. The chemical timescale for CH_2CO exceeds $10^5 - 10^6$ years.

Not surprisingly that turbulent mixing enhances abundances and column density of these organic species, given their long evolutionary timescales governed by surface reactions and photodissociation of ices by the CRP- and X-ray-induced secondary UV radiation field. The HCOOH and the HCOOH ice are more abundant since water ice abundances and HCO^+ abundances are increased by the mixing, leading to more efficient production of the parental ion, CH_3O^+ . Both for gas-phase and solid formic acid radial transport is important. The effect is less pronounced for HNCO as its precursor species, OCN, is enhanced by transport only by less than 1 order of magnitude. The HNCO ice, produced in the lower part of the molecular layer, is transported by diffusion to the cold midplane where it cannot be synthesized otherwise. Relative abundances of gas-phase acetaldehyde are greatly enriched by the disk mixing in the middle of the molecular layer ($z \approx 1.5 H_r$), within the inner 100 AU. As its synthesis proceeds via surface recombination of CH_3 and HCO, in the laminar model appropriate conditions are only met in the very inner midplane/molecular layer. In the fast mixing model larger

quantities of solid acetaldehyde can be accumulated as more icy grains reach the warm disk regions. The vertical mixing brings the CH_3CHO ice in the inner midplane to the molecular layer, where it photoevaporates, and then radially transported to larger distances. The ethenone abundances are vertically broadened by the mixing, and moderately enriched as the ethenone ice production is enhanced by the turbulent mixing.

5. DISCUSSION

5.1. Comparison with previous studies and future developments

In this Section we discuss the results and the drawbacks of our model in the context of other studies of the chemo-dynamical evolution of protoplanetary systems.

(*Models of the inner Solar nebula: the role of advective transport*) Historically, the interest to this topic has been initiated by the cosmochemical community studying the initial stages of the formation of the Solar system. The presence of high-temperature condensates, like CAIs and crystalline silicates, in pristine chondritic meteorites (formed within a few AU from the Sun) and comets (formed within 10–20 AU) as well as almost perfect isotopic homogeneity of the inner Solar nebula ($r \lesssim 10 - 20$ AU) at a bulk level both require an efficient mixing mechanism with a transport speed of $\lesssim 1$ AU per $5 \cdot 10^4$ yr or 10 cm s^{-1} (e.g., Wooden et al. 2007; Brownlee et al. 2008; Ciesla 2009). According to the current knowledge, the Solar nebula and other protoplanetary disks represent an outcome of the viscous evolutionary stage that follows the initial collapse of a molecular cloud core (e.g., Cassen & Moosman 1981; Cameron 1995; Larson 2003).

The ability of turbulent or advective transport to cause radial mixing of materials in the inner early Solar system has been proposed and investigated by Morfill (e.g., Morfill 1983; Morfill & Völk 1984), with a simple 1D analytical disk model and passive tracers. In a similar manner, 2D radial mixing of gaseous and solid water in the inner nebula has been studied by Cyr et al. (1998). In a long series of papers the group of Prof. H.-P. Gail (Heidelberg University) has investigated various aspects of the chemo-dynamical evolution of the inner protosolar nebula (1 – 10 AU), progressing from stationary accretion disk models and crude gas-phase chemistry toward a self-consistent 2D radiative-hydrodynamical model with the coupled C-, H-, O- gas-phase chemistry (e.g., Bauer et al. 1997; Finocchi et al. 1997; Gail 1998, 2001, 2002; Wehrstedt & Gail 2002; Gail 2004; Keller & Gail 2004; Tscharnutter & Gail 2007). In Bauer et al. (1997) the gas-phase C-, H-, N-, O-chemistry driven by dust destruction and evaporation of ices in the presence of slow radial transport has been modeled, utilizing the semi-analytical one-zone disk model of Duschl et al. (1996). The authors have found that silicates tend to evaporate under equilibrium conditions, whereas carbon dust is slowly destroyed by combustion by OH, and that at $r \lesssim 1$ AU the CO concentration is higher than that of water. In Finocchi et al. (1997) and Gail (2001) the one-zone stationary disk model has been considered, whereas in Gail (2002) and Wehrstedt & Gail (2002) the one-zone time-dependent α -disk model with a larger chemical network of 106 species, annealing of amorphous silicates, and more detailed description of carbon dust oxidation by O and OH has been used. The major finding is that the radial transport enriches the outer, $r > 10$ AU nebular regions with methane and acetylene produced by oxidation of carbon dust at $r \lesssim 1$ AU, as observed in comets of Hyakutake and

Hale-Bopp. The advection also transports crystalline silicates to the 10–20 AU region. In the later papers (Keller & Gail 2004; Tscharnutter & Gail 2007), a more accurate model has been developed, with a self-consistent 2D prescription of advective transport and turbulent diffusion, grey radiative transfer, proper dust and gas opacities, and disk hydrodynamical evolution with parametric viscosity. The model was coupled to a limited gas-phase C-, H-, O-chemistry involving nearly 90 neutral-neutral reactions. They have found that quasi-stationary accretion flows develop a 2D structure such that in the disk midplane gas moves outward, carrying out the angular momentum, whereas inward mass accretion goes through the surface layers. The radial advection dominates the diffusive mixing in outer disk regions at $r > 5$ AU. Thus, chemical species produced by the “warm” chemistry in the inner nebula can reach its outer region, where they are intermixed by turbulence with surrounding matter and freeze-out. They have considered neither X-ray- nor UV-driven processes, no ion-molecule and surface chemistry, and assumed sublimation-evaporation equilibrium for ices. Their key result is that the slow water-shift reaction transforming CO and water into CO_2 and H_2 at high pressure and temperature is important for the oxygen chemistry. The H_2 and CO evolution is insensitive to transport, while abundance distributions of e.g. O, O_2 , CO_2 are altered by the disk dynamics within 300 years of the evolution.

Contrary to these studies, our modeling is related to outer nebular regions beyond 10 AU and does not include advective transport. However, in the presence of steep chemical gradient for a molecule, radial diffusive mixing is able to transport it from 100 AU to 1 AU within about $1 - 2 \times 10^6$ years, and from 1 AU to 10 AU within about $\lesssim 3 \times 10^5$ years, which is still less than a typical disk lifetime of several Myrs (see Eq. (7) and Fig. 1). Our chemical network incorporates much more species and reactions, including surface chemistry, and the high-energy processing of the gas and icy mantles. Nonetheless, the calculated H_2 and CO column densities are not sensitive to the diffusive mixing in our model, similar to what was found by Tscharnutter & Gail (2007) (Fig. 9 and Table 5). Also, in agreement with Gail et al. results, we show that the synthesis of hydrocarbons, including CH_4 and C_2H_2 , is intensified by the mixing, particularly in the zone of comet formation around 10–20 AU (Fig. 8). Furthermore, CO_2 ice, which is produced via surface reactions in the warm inner midplane and can be considered as an example of a “warm” species, is transported outward by the 2D-turbulent mixing. In addition, we also found that oxidation chemistry is important for the evolution of O-bearing species, though we do not account for the carbon dust destruction, unlike Tscharnutter & Gail (2007).

(*Models of protoplanetary disks: the role of advective transport*) Next, we focus on disk models that has been used to simulate chemical evolution of protoplanetary disks in the astrophysical context. Aikawa et al. (1999) have utilized an isothermal α -disk model of Lynden-Bell & Pringle (1974) with $\dot{M} = 10^{-8} M_\odot \text{ yr}^{-1}$, and calculated its density structure assuming hydrostatic equilibrium in vertical direction. They have used the early version of the UMIST 95 chemical ratefile (Millar et al. 1997), considered sticking and thermal desorption of molecules and surface formation of molecular hydrogen, and grain re-charging (about 250 species and 2 300 reactions). No X-ray-driven and surface chemistry, other than H_2 formation, has been included.

These authors have modeled the chemical evolution in the presence of steady inward accretion, using both atomic and molecular initial abundances, and found similar results. We also find that the difference in the calculated abundances between the adopted “low metals” atomic initial abundances and those from a molecular cloud is negligible in our model. Aikawa et al. (1999) have found that it takes about 3 Myr to transport disk material from 400 AU to 10 AU (similar to the timescale of radial mixing in our model). The inward advection leads to higher concentrations of heavy hydrocarbons at $\lesssim 20$ AU, whereas methane is a dominant hydrocarbon in the outer disk region. In our laminar model methane prevails over heavier hydrocarbons in the entire disk, while in the presence of radial and vertical mixing a substantial fraction of CH_4 is converted into heavy carbon chains (especially at 10–50 AU; see Fig. 8). Aikawa et al. (1999) have concluded that the radial transport leads to simultaneous existence of the reduced (e.g. CH_4) and oxidized (e.g. CO_2) ices, as observed in comets, and as found by our chemo-dynamical modeling. Finally, they have studied in detail chemistries of O-, N-, and C-bearing species and found that H_3^+ and He^+ produce e.g. CO_2 , CH_4 , and NH_3 from CO and N_2 , and that grain properties and ionization rate are crucial factors for molecular evolution. This is consistent with our findings, but with an additional notion that X-rays further strengthen He^+ and H_3^+ influence on the chemical evolution of turbulent protoplanetary disks.

Later, Woods & Willacy (2007) have investigated the genesis of benzene in protoplanetary disks at $r \lesssim 35$ AU. They have used a D’Alessio-like flaring α -disk model with accurate UV radiative transfer and detailed calculations of the heating and cooling balance of gas. The X-ray ionization and dissociation have not been taken into consideration. The chemical network has been adopted from a sub-set of the UMIST 99 (Le Teuff et al. 2000) ratefile augmented with gas-grain and surface reactions (in total 200 species and 2 400 reactions). The passage of a gas parcel from > 35 AU onto the central star has been calculated. Woods & Willacy (2007) have found that the radial transport results in efficient production of benzene at $\lesssim 3$ AU, mostly due to ion-molecule reactions between C_3H_3 and C_3H_4^+ , followed by grain dissociative recombination. These results are very sensitive to the adopted value of C_6H_6 binding energy. Similarly, we find that benzene is produced via the same ion-molecule reaction because the surface network is limited for heavy hydrocarbons and does not include surface routes to C_6H_6 , whereas the gas-phase production is efficient. Nevertheless, as in the paper of Woods & Willacy, the C_6H_6 abundances and column densities in the inner disk at 10–30 AU are increased by vertical turbulent diffusion in our model by up to 2 orders of magnitude, see Fig. 8.

Nomura et al. (2009), using a disk chemical model with radial advection, studied the evolution of the inner region ($\lesssim 12$ AU). The α -model of a disk around a 6000 K star with the mass accretion rate of $10^{-8} M_\odot \text{ yr}^{-1}$ has been considered, with gas and dust temperatures computed independently. They have modeled penetration of the UV and X-ray radiation into the disk, and utilized the RATE 06 (Woodall et al. 2007) with gas-grain interactions. The chemical evolution of gas parcels following various inward trajectories has been calculated. The authors have found that the abundances are sensitive to the transport speed, and that the fast transport allows gaseous molecules to reach disk regions where they would otherwise be depleted. They have concluded that dynamical disk model facilities synthesis of methanol, ammonia, hydro-

gen sulfide, acetylene, etc., and predicted the observability of the $J = 3_0 - 2_0$ methanol line at 145 GHz with ALMA. As we have shown above, our 2D-mixing model follows the same tendency, and enriches molecular content of the protoplanetary disk with complex species.

Visser et al. (2009b) has developed a 2D semi-analytical evolutionary model that follows collapse of a dense core into a disk (a transition from the Class 0 to Class I phase) and tracks by trajectories infall motions of gas. They have used time-dependent RT to compute dust temperature consistently, and considered only freeze-out and evaporation of CO and water ices. Their major results are that the CO ice evaporates during collapse and later re-accretes to dust, while the water ice remains almost intact (unless heated by a protostar at $r < 10$ AU). Material inside 5–30 AU in the early disk spends $\lesssim 10^4$ years at temperatures of ~ 20 –40 K, which is sufficient to produce complex organics. With our disk physical model that is at a steady-state and incorporates a detailed gas-surface chemistry we indeed see a rise in abundances of many complex molecules, as their surface production at $T \lesssim 30$ K and evaporation are enhanced by the diffusive mixing.

(*Models of protoplanetary disks: the role of turbulent transport*) Now we compare our results to more closely related studies of disk chemical evolution with turbulent mixing. In the first paper on this topic, Ilgner et al. (2004) have investigated the influence of the 1D vertical mixing and the radial advection on chemistry of a steady 1+1D- α -disk model ($\alpha = 0.01$, $\dot{M} = 10^{-8} M_{\odot} \text{ yr}^{-1}$). The modeling of a reactive flow system has been discussed in detail. They have adopted Xie et al. (1995) description for the diffusion and Lagrangian description for advective transport (trajectories from 10 to 1 AU). Ilgner et al. (2004) have used a subset of the UMIST 95 database with gas-grain interactions and no surface chemistry (≈ 240 species, 2 500 reactions). Ilgner et al. have considered 3 steady-state solutions for the disk physical structure, and investigated the disk evolution by adding advective and turbulent transport processes. Their key findings are that the chemistry is sensitive to the disk thermal profile, that the vertical mixing removes vertical abundance gradients, and that local changes in species concentrations due to mixing can be radially transported by advection. Ilgner et al. (2004) have concluded that diffusion has a limited effect on the disk regions dominated by gas-grain kinetics, though it enhances abundances of atomic oxygen and thus alters the evolution of related species (SO, SO₂, CS, etc.). The advective transport without mixing results in destruction of oxygen and OH at $r < 5$ AU. Our model, despite being limited to outer disk regions (beyond 10 AU), confirms their results that oxygen abundances are increased by diffusion (Fig 9), further propagating into the chemistry of many related species, particularly sulfur-bearing species like SO and SO₂. We find that turbulent mixing may steepen or soften chemical gradients (e.g., for atomic ions and most of molecules, respectively), and it definitely affects more strongly the evolution of species produced via gas-surface kinetics. This fundamental feature of the presented chemical model is due adopted extended set of surface photo- and recombination processes. This further emphasizes the need in the extended surface reaction network. Some conclusions, especially those related to complex organics do depend on the complexity of the adopted surface chemistry model.

Next, Willacy et al. (2006) have utilized a steady-state α -disk model similar to that of Ilgner et al. and used the Xie

approach to account for the disk viscosity. A plane-parallel model of the UV irradiation, no stellar X-ray radiation, and a subset of the UMIST 95 database with gas-grain interactions and surface kinetics from Hasegawa et al. (1992) have been adopted. Our chemical network is about 3 times larger, and uses recently updated reaction rates. They have studied the impact of the 1D-vertical mixing on the chemical evolution of the outer disk ($r > 100$ AU). Overall, they have found that the vertical transport can increase column densities by up to 2 orders of magnitude. Another result is that the 3-layered disk structure is preserved in the mixing model, albeit depths of many molecular layers are increased. They have observed that the higher the diffusion coefficient, the higher the impact of the turbulent mixing. Our results confirm these general findings, with the chemical network, that is about 3 times larger and based on recently updated reaction rates. In contrast to the results of Willacy et al., we obtain that the evolution of the ionization degree, ammonia and N₂H⁺ are sensitive to the mixing, whereas column densities of CO, H₂CO, CN, C₂H are steadfast (Tables 5–7). This is because in our model the X-ray irradiation of the disk, production of reactive radicals by photodissociation of ices, and UV-photodesorption are taken into account. In the absence of photoevaporation, e.g., the CO production in the model of Willacy et al. becomes responsive to transport of ices from midplane and atomic C and O from atmosphere. In our model this is true only for heavy ices with large binding energies ($\lesssim 3000$ –5 000 K), like hydrocarbons. Also, our disk study focuses on the large distances from 800 till 10 AU that has not been considered by Willacy et al. If we restrict our model to the distances beyond 100 AU, the ionization degree and column densities of many other species become steadfast. Furthermore, our study supports the result that the column densities of complex molecules like methanol are greatly enhanced by the disk dynamics.

In 2006 Ilgner & Nelson have investigated in detail ionization chemistry in disks and its sensitivity to various physical and chemical effects at $r < 10$ AU, like the X-ray flares from the young T Tauri star (Ilgner & Nelson 2006b), vertical mixing (Ilgner & Nelson 2006a), amount of gas-phase metals, and validity of various chemical networks (Ilgner & Nelson 2006c). Using an α -disk model with stellar X-ray-irradiation, they have demonstrated that the simple Oppenheimer & Dalgarno (1974) network made of 5 species tend to overestimate the ionization degree since metals exchange charges with polyatomic species, and that magnetically decoupled “dead” region may exist in disks unless small grains and metals are removed from gas. Next, the influence of vertical diffusion on the ionization fraction has been studied. They have found that the mixing has no effect on $X(e^-)$ if metals are absent in the gas since recombination timescales are fast, whereas at $X(\text{Me}) \lesssim 10^{-10}$ – 10^{-8} $\tau_{\text{chem}} > \tau_{\text{mix}}$ and diffusion drastically reduces the size of the “dead” zone. Finally, it has been shown that in the disk model with sporadic X-ray flares (by up to a factor of 100 in the luminosity) the outer “dead” zone disappear, whereas the inner “dead” zone evolves along with variations of the X-ray flux. Indeed, our extended disk chemical model shows that ionization degree and abundances of charged atoms and molecules are sensitive to the transport in the disk regions with $r \lesssim 100$ –200 AU, and that polyatomic ions are important charge carriers in the disks (see also Semenov et al. 2004). Also, the role of the X-ray photons is crucial for the disk ionization fraction and its molecular composition (see also Schreyer et al. 2008; Henning et al.

2010).

The first attempts to model self-consistently disk chemical, physical, and turbulent structures in full 3D have been performed by Turner et al. (2006) and Ilgner & Nelson (2008). Both studies have employed a shearing-box approximation to calculate a patch of a 3D MHD disk at radii of $\sim 1 - 5$ AU, treated the development of the MRI-driven turbulence, and focused on the multi-fluid evolution of the disk ionization state. In the study of Turner et al. ohmic resistivity, vertical stratification, the CRP-ionization, and the Oppenheimer-Dalgarno time-dependent ionization network have been considered. They have found that turbulent mixing transports free charges into the dark disk midplane faster than these recombine, coupling the midplane matter to magnetic fields. As a result, accretion stresses in the disk “dead” zone are only several times lower than in surface layers, with a typical timescale of about 1–5 Myr. Ilgner & Nelson (2008) have adopted a similar approach but considered the X-ray ionization with $L_X = 10^{31}$ erg s $^{-1}$. They have re-confirmed their earlier findings (Ilgner & Nelson 2006a,c) that turbulent mixing has no effect on the disk ionization structure in the absence of the gas-phase metals. The presence of metals, however, prolongs the recombination timescale, and the mixing is thus able to enliven the “dead” zone at $r \geq 5$ AU (with the resulting $\alpha = 1 - 5 \cdot 10^{-3}$). Both these studies are based on a pure gas-phase chemical network, whereas in our extended gas-grain model metals are fully depleted in the disk regions with $T \lesssim 150 - 200$ K. Consequently, our modeling corresponds to the “no metals” case of Ilgner & Nelson (2008), so turbulent transport does not much affect the ionization fraction in the disk midplane (see Fig. 7, 1st panel).

Finally, in the recent paper by Heinzel et al. (2011) the chemical evolution of the protoplanetary disk along with radial viscous accretion, vertical mixing, and vertical wind transport has been investigated. The steady-state disk model with $\alpha = 0.01$, $\dot{M} = 10^{-8} M_\odot$ yr $^{-1}$, and $L_X = 10^{30}$ erg s $^{-1}$ has been adopted. The heating and cooling processes have been included to calculate consistently the gas temperature in the disk surface region. In the inner disk region the gas and dust temperatures start to diverge when the z/r ratio reaches about 0.2, which for our disk model translates to about $1.5 H_r$. Thus our approximation of equal dust and gas temperatures is accurate in the disk midplane and the lower part of the molecular layer, and becomes unrealistic in the disk atmosphere. Yet it barely affects column densities of many molecules as these are dominated by the molecular concentrations in the dense regions where $T_{\text{dust}} \approx T_{\text{gas}}$.

Heinzel et al. (2011) have adopted the gas-grain RATE06 (Woodall et al. 2007) network, no surface reactions apart from the H₂ formation, and the X-ray and UV-photochemistry (375 species and about 4350 reactions). Heinzel et al. have concluded that water and hydroxyl abundances in the disk surface regions may increase substantially via neutral-neutral reactions with molecular hydrogen produced via chemisorbed-assisted surface recombination. It has been found that the disk wind has a negligible effect on disk chemistry as its upward transport speed is too low compared to the longest chemical timescale attributed to the adsorption. Note that in our model the adsorption timescale is also long, but the surface chemistry timescales are even longer ($\gtrsim 1$ Myr). They have pointed out that the radial accretion flow alters the molecular abundances in the cold midplane, whereas diffusive turbulent mixing affects the

disk chemistry in the warm molecular layer ($r = 1.3$ AU, $T \sim 200$ K). We find that the radial turbulent transport can affect abundances in the midplane at $r \gtrsim 10$ AU (see, e.g., CO₂ ice in Fig. 9), while effective vertical mixing operates from midplane well through the molecular layer and lower disk atmosphere. They have concluded that diffusive mixing smoothes the chemical gradients and that the abundances of NH₃, CH₃OH, C₂H₂ and sulfur-containing species are the most enhanced. This has been related to increased ammonia abundances in the transport model, in which NH₃ is effectively produced via gas-phase reactions with more abundant oxygen. In our simulations temperatures are usually well below 200 K, but we also see that sulfur-bearing molecules are among the most sensitive species to the disk dynamics, along with complex organics (like methanol), hydrocarbons (like acetylene), and other species (like ammonia). This is due to their dependence on slow surface processes and evaporation (for heavy gaseous species).

(Future directions of development for disk chemical models) Overall, there is a considerable progress over the last decade in constructing more feasible chemo-dynamical models of the early Solar nebula and other protoplanetary disks. It will gain further momentum in light of the forthcoming ground-breaking Atacama Large Millimeter Array (ALMA) currently under construction in Chile. In what follows, we surmise possible future directions of the development of the nebular and protoplanetary disks chemical models. The full 3D chemo-MHD models of the entire disk evolution within 1–5 Myr are beyond possible even with modern computational resources available for astronomers. Only local 3D models with radically reduced chemistry and a short evolutionary time span of 1000–10000 years or semi-analytical models of the entire disk with extended chemistry and $t \sim 1$ Myr will be feasible in the foreseeable future. The inner, planet-forming disk regions subject to disk-planet(s) interactions (gaps, spiral waves, shocks) may well be far from axial symmetry and require 3D modeling approach (e.g., Wolf et al. 2002; Fukagawa et al. 2004; Piétu et al. 2005). The accurate opacities of dust and gas covering a wide range of temperatures, densities, gas composition, and dust topological and mineralogical properties will have to be developed (e.g., Semenov et al. 2003; Helling & Lucas 2009).

Likely, the steady-state disk physical model adopted in the present study needs to be re-adjusted into an evolutionary model with consistent calculations of grain evolution (e.g., Birnstiel et al. 2010; Fogel et al. 2011; Vasyunin et al. 2011), photoevaporation (e.g., Gorti et al. 2009), and accurate gas temperature (e.g., Gorti & Hollenbach 2004; Woitke et al. 2009). The grain coagulation, fragmentation, and sedimentation lead to re-distribution of the total dust surface area, higher UV ionization rates, and thus to shift of molecular layers toward the midplane, with a significant increase of molecular column densities in the intermediate layer and decrease of their depletion zones (Fogel et al. 2011; Vasyunin et al. 2011). In the evolutionary disk models the total disk mass and size, and thus its density, thermal, and ionization structures change with time, altering conditions at which chemical processes proceed both in the gas phase and onto the dust surfaces (Gorti et al. 2009). In evolutionary models covering formation and build-up disk phases, a large amount of gas and dust materials experience events of heating, cooling, re-condensation, annealing, and varying irradiation intensities (e.g., Gail 2002, 2004; Visser et al. 2009b).

A more realistic 2D or full 3D prescription of the X-ray

and UV radiation transfer modeling with scattering has to be included. The accurately calculated UV spectrum with the L_α line is vital to compute realistic photodissociation and photoionization rates, and shielding factors for CO and H₂ (see, e.g., van Zadelhoff et al. 2003; Bethell et al. 2007; Visser et al. 2009a). The realistic (may be, variable) stellar X-ray spectrum is required to calculate gas temperature in the disk atmosphere, and for modeling disk ionization structure and ion-molecule chemistry (e.g., Glassgold et al. 2005; Meijerink et al. 2008; Aresu et al. 2011). At densities of $\lesssim 10^4 - 10^6 \text{ cm}^{-3}$ gas temperature decouples from that of dust, which will affect the chemical and dynamical evolution in the upper disk layers (e.g., Kamp & Dullemond 2004; Owen et al. 2011). The dissipation of Alfvénic waves generated by the MHD processes inside the disk can also heat gas in the disk atmospheres (e.g., Hirose & Turner 2011).

In comparison to the status of the disk physical structure where many key issues have been realized and partly solved, the advances in modeling disk chemistry are less straightforward. First of all, chemical studies employ various networks fully or partly based on astrochemical ratefiles that have been developed to model distinct astrophysical environments. Hopefully, this will be relieved with the advent of the public Kinetic Database for Astrochemistry (KIDA)⁶ that includes state-of-the-art rate data (Wakelam et al. 2010b). Unfortunately, the intrinsic uncertainties in gas-phase reaction rates hamper the accuracy of chemical predictions both on abundances and column densities (see, e.g., Wakelam et al. 2006; Vasyunin et al. 2008; Wakelam et al. 2010a). The pace at which these quantities are measured in laboratories or calculated by quantum chemical models precludes the rapid progress for thousands of astrochemically-relevant processes (Savin et al. 2011).

In the inner ($\lesssim 5 \text{ AU}$) disk regions with $T \gtrsim 100 - 300 \text{ K}$ and densities exceeding 10^{12} cm^{-3} three-body processes, many reverse reactions, and neutral-neutral reactions with large barriers are activated, and have to be fully taken into account (e.g., Aikawa et al. 2002; Tscharnatur & Gail 2007; Harada et al. 2010). The X-ray-driven ionization and dissociation of molecules other than H₂ are poorly understood, but important for disk chemistry (e.g., Glassgold et al. 2009). In the upper disk regions, upon gas-phase or surface recombination or due to ionization/dissociation an excess of energy may translate into (ro-)vibrational excitation of a product molecule, which may react differently with other species (e.g., Pierce & A'Hearn 2010). This aspect has so far been almost completely neglected in astrochemical models.

In cool outer disk regions gas-grain interactions and surface reactions are essential, yet the latter are often disregarded in disk models. The same is true for nuclear-spin-dependent chemical reactions involving ortho- and para-states of key species, such as H₃⁺, H₂, H₂O, etc. (e.g., Pagani et al. 1992, 2009; Crabtree et al. 2011). Usually weak physisorption of molecules is considered in chemical models, while molecules can also form chemical bonds with dust surfaces, leading to heterogeneous surface chemistry active both in cold and hot regions, particularly on PAHs and carbonaceous grains (e.g., Fraser et al. 2005; Cazaux et al. 2005; Cuppen & Hornekær 2008). Despite the recent laboratory efforts to measure binding energies of key molecules like CO, N₂, water, etc. to various astrophysical ices and their photo-

todesorption yields, many of these values are still lacking accurate estimates (Bisschop et al. 2006; Öberg et al. 2009b,a). The dynamics, reactivity, photodissociation, and desorption of ices embedded into dust mantles are hard to measure or model, and even harder to interpret (see, e.g., results for the water ice Andersson et al. 2006; Andersson & van Dishoeck 2008; Bouwman et al. 2011). For example, sub-surface diffusion may increase desorption efficiency in the case of well-mixed ices within the H₂O ice matrix. Along with thermal, UV-, CRP- and X-ray-triggered desorption (Leger et al. 1985; Najita et al. 2001; Walsh et al. 2010), typically considered in disk chemical studies, other non-thermal mechanisms, like grain-grain destruction and explosive desorption (Shalabiea & Greenberg 1994) can be operative. The surface recombination on porous grain surfaces or within heterogeneous ices is also non-trivial to model accurately (e.g., Cuppen et al. 2009; Fuchs et al. 2009; Ioppolo et al. 2011). The surface chemistry can be restricted to several uppermost monolayers of the grain, while often in chemical models the corresponding rates are calculated assuming it is active everywhere in the ice mantle (e.g., Hasegawa & Herbst 1993). In addition, the presence of large, photostable PAHs in the gas assists synthesis of polyatomic molecules by providing surface area for surface recombination, ability to re-radiate energy released upon non-destructive ion-PAH recombination, and due to the combustion chemistry in the inner disk region (e.g., Wakelam & Herbst 2008; Kress et al. 2010; Perez-Becker & Chiang 2011). Finally, calculated molecular concentrations depend on the adopted set of elemental abundances that may vary from region to region, and underlying assumptions about depletion of heavy elements from the gas phase (e.g., Wakelam et al. 2010a).

5.2. Cold molecules in DM Tau

In the following two subsections we elaborate on feasibility of the present study to explain observations of diagnostic molecules and ices in protoplanetary disks and the Solar system.

The kinetic temperature distributions have been measured in nearby disks of DM Tau, LkCa 15, MWC 480, and AB Aur by Dartois et al. (2003); Piétu et al. (2005, 2007) and Henning et al. (2010), using the Plateau de Bure Interferometer and the (1-0) and (2-1) emission lines of CO isotopologues, HCO⁺, and C₂H. These emission lines have different opacities and thus sample gas temperature at various heights above the disk equatorial plane (see Dartois et al. 2003). CO lines are particularly suitable for such studies because they are easily excited at low densities of 10^4 cm^{-3} , while the CO isotopologue abundances vary by orders of magnitude. Consistently with predictions from a passively heated, flaring model (e.g., Chiang & Goldreich 1997; D'Alessio et al. 1999; Dullemond & Dominik 2004), vertical temperature gradients have been found. In disks around hot stars midplane temperatures are quite high. At $\sim 100 \text{ AU}$, the disk around the 10 000 K Herbig A0 AB Aur has gas temperatures ranging from $20 \pm 3 \text{ K}$ (as measured by C¹⁸O J = 1 – 0) to $35 - 40 \text{ K}$ (¹³CO 1 – 0, 2 – 1) and to 68 K (¹²CO 2 – 1), see Piétu et al. (2005). A similar trend has been obtained for a disk surrounding the cooler, 8 500 K Herbig A4 MWC 480 star, with CO temperatures growing from $21 \pm 4 \text{ K}$ in the midplane to $48 \pm 1 \text{ K}$ in the molecular layer at 100 AU from the star (Piétu et al. 2007).

In the bright, large 800 AU disk around cold, 3750 K

⁶ <http://kida.obs.u-bordeaux1.fr>

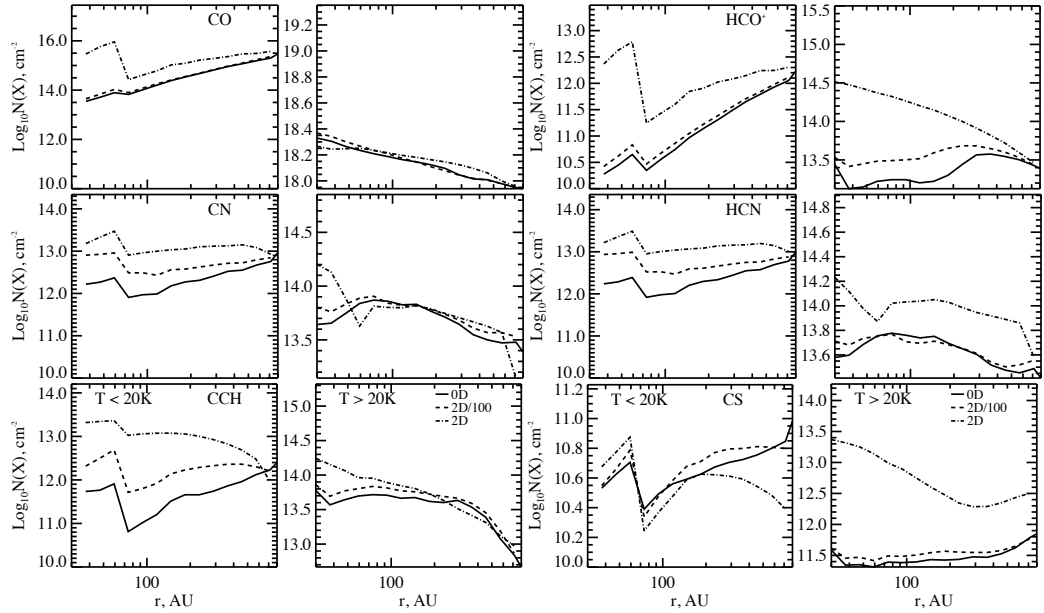


Figure 13. (Top to bottom) The vertical column densities of CO, HCO⁺, CN, HCN, CCH, and CS at $t = 5$ Myr in the cold ($T < 20$ K; left) and warm ($T > 20$ K; right) disk regions. Results are shown for the 3 disk models: (1) the laminar chemistry (solid line), (2) the 2D-mixing model with $Sc = 100$ (dashed line), and (3) the 2D-mixing model with $Sc = 1$ (dash-dotted line).

(M1) DM Tau star very cold CO temperatures of ≈ 15 K at 100 AU have been reported by Dartois et al. (2003), based on analysis of the PdBI ^{13}CO (1-0) spectral map. In the later study by Pi  tu et al. (2007) even lower temperatures of 8 and 15 K probed by the (1-0) and (2-1) transitions of ^{13}CO , and $T_{\text{kin}} = 14 \pm 2$ K probed by the HCO⁺ (1-0) line have been derived for the outer DM Tau disk. In contrast, in the same disk optically thick ^{12}CO lines give kinetic temperature of about 25 K. Henning et al. (2010) found very low kinetic temperature of ≈ 7 K for C₂H in the DM Tau system, using the CCH (1-0) and (2-1) PdBI data. Finally, in Chapillon et al. (2011, submitted) similarly low values for the CN (1-0) temperatures have been inferred. While derived low temperatures are characteristic for midplane regions of protoplanetary disks surrounding cool T Tauri stars, the presence of gaseous molecules at such extreme conditions is puzzling. The evaporation temperatures for CO, C₂H, and CN are about 20, 30, and 40 K, respectively (see Table 1), and in dense, dark midplane ($T \sim 10 - 20$ K) they are rapidly depleted, $\tau_{\text{acc}} \lesssim 10^3 - 10^4$ years (Tables 3-4).

In Paper I (Semenov et al. 2006) the problem of the cold CO gas reservoir in the DM Tau disk has been tackled using the 1+1D D'Alessio et al. (1999) $\alpha = 0.01$ flaring disk model with the 2D radial-vertical turbulent diffusion. We have found that the CO column density of about 10^{16} cm^{-2} is required in the disk midplane to explain the puzzling observations of the cold CO in DM Tau. Such CO column densities in the disk region with $T \leq 25$ K have been obtained in the model with vertical and radial mixing at all radii, while in the laminar model these values only appeared at $r \gtrsim 500$ AU. The CO molecules are transported from the warm molecular layer to the cold disk midplane, maintaining concentration of CO even at late times, $t \gtrsim 10^5 - 10^6$ years.

Aikawa (2007) have used a steady-state α -disk structure and a 1D-vertical mixing model to show that the warm CO gas from the intermediate layer can be transported down to the cold midplane at a rate that can be competitive with the

CO adsorption rate. The efficiency of this process has been found particularly pronounced for the disk model when moderate grain growth is allowed, with grain sizes $\lesssim 1\mu\text{m}$. A substantial grain growth leads to a decrease of the averaged dust surface area and thus less active freeze-out (see also results of Fogel et al. 2011; Vasyunin et al. 2011).

Later, Hersant et al. (2009) have utilized a power-law, α -disk model with an isothermal midplane, strong UV scattering, and 1D-vertical mixing. They have found that the UV-desorption of CO and other ices prevails over their upward transport by the vertical mixing to warm regions, leading to a large amount of gaseous CO, HCO⁺, HCN in the midplane even in the laminar model. This is due to the adopted high UV-desorption yield of $\sim 0.1\%$ (e.g.,   berg et al. 2009b) and assumed high UV penetration efficiency caused by the UV scattering on small dust grains in the disk atmosphere.

Compared to Paper I, we now use the full chemical network based on the OSU model, higher photodesorption yields of 10^{-3} , and the slow surface hydrogenation rates based on the results of Katz et al. (1999), with 5% of products to be released back to the gas upon surface recombination (Garrod et al. 2007). In Figure 13 we show the column densities of CO, HCO⁺, CN, HCN, C₂H, and CS at 5 Myr in the disk regions with $T < 20$ K (odd rows) and $T > 20$ K (even rows) calculated with the laminar, the slow 2D-, and the fast 2D-mixing models. Note that in the inner region at $r \lesssim 30$ AU kinetic temperatures are higher than 20 K even in the midplane (Fig. 1, 1st panel).

As can be clearly seen, turbulent transport does enhance molecular abundances and column densities in the DM Tau disk midplane for the all species apart from CS. Compared to the results of Paper I, the CO column densities in the midplane region ($T < 20$ K) are increased by the diffusive mixing by 2 orders of magnitude, to values between 10^{15} and 10^{16} cm^{-2} , while in the laminar model these are still relatively high, $\gtrsim 10^{14} \text{ cm}^{-2}$. As in the study of Hersant et al. (2009) powerful CRP-induced and UV-desorption keeps some

molecules in the gas phase even in the midplane. Transport from the disk regions with $T \gtrsim 20$ K, like the molecular layer and the inner, accretion-heated midplane at $r \lesssim 30$ AU, where CO can be produced on grains, replenishes gaseous CO in the cold midplane. The column densities of “warm” CO are much higher, $\approx 10^{18} \text{ cm}^{-2}$ and are not affected by the disk dynamics. This is because chemical evolution of CO is relatively fast compared to the transport speeds, while CO is also widespread through the disk, canceling out the chemical gradient needed for its diffusion, see Section 4.3. The amount of cold CO in the mixing model is hardly sufficient to explain the puzzling ^{13}CO PdBI observations of DM Tau. On the other hand, there is enough warm CO to explain the presence of the $T \approx 26$ K CO gas derived from the optically thick ^{12}CO data tracing the disk upper region.

HCO^+ shows an increase of midplane column densities by up to a factor of 100 in the mixing case, while in the molecular layer its column densities are enhanced by a factor of $\lesssim 30$. This is due to the sensitivity of H_3^+ ion, required for HCO^+ production, to the turbulent transport (see discussion in Section 4.1). In the mixing model, H_3^+ is particularly abundant at elevated disk heights, $z \gtrsim 1 - 2 H_r$, and so is HCO^+ . The ratio of column densities of warm and cold HCO^+ is large, and nearly the same for both the laminar and 2D-mixing models, a factor of ≈ 30 and 10–100, respectively. With a typical column density of $10^{13} - 10^{14} \text{ cm}^{-2}$ at $r \gtrsim 100$ AU, the HCO^+ (1-0) line remains optically thin in the outer disk, sampling both the disk midplane and the warm molecular layer.

On the other hand, the critical density required to excite a molecular line from a linear molecule can be estimated as:

$$n_{\text{cr}} = \frac{A_{ul}}{\sigma v}, \quad (19)$$

where A_{ul} is the Einstein coefficient for spontaneous emission from the level u to l , and σ and v are the cross-section and velocity of a collisional partner, respectively. For the H_2 -dominated disk midplane with $T = 10 - 20$ K $\sigma v \approx 3 \cdot 10^{-11} \text{ cm}^3 \text{ s}^{-1}$ (e.g., Wilson et al. 2009). We adopt $A_{10} = 4.25 \cdot 10^{-5} \text{ s}^{-1}$ from the LAMDA database (Schöier et al. 2005), and find that the critical density for the $\text{HCO}^+ J = 1 - 0$ excitation is $\approx 1.5 \cdot 10^6 \text{ cm}^{-3}$. The region where densities exceed 10^6 cm^{-3} extends vertically up to $\lesssim 3$ and $1 H_r$ in the inner and outer disk, respectively, and covers the midplane and the molecular layer (see Fig. 1). Thus, HCO^+ (1-0) emission would originate from the $T > 20$ K disk region, and the resulting temperature derived from this transition would likely exceed 15 K obtained from interferometric observations by Piétu et al. (2007).

The behavior of C_2H , CN, and HCN is similar as their chemical evolution is tightly linked (Section 4.4). Their vertical column densities are not much altered by the turbulent mixing, having a typical value of $\sim 3 \cdot 10^{13} - 10^{14} \text{ cm}^{-2}$ at 100 AU. Since absolute concentrations of C_2H , CN, and HCN are highest in the molecular layer where chemical timescales are relatively short, their $T > 20$ K column densities are not strongly increased by diffusion, less than by a factor of 3. Contrary, the column densities in the DM Tau midplane ($T < 20$ K) are raised by the transport by an order of magnitude for CN and HCN, and by 2 orders of magnitude for C_2H . This is caused by the long evolutionary timescales in the midplane associated with gas-surface kinetics (e.g., gaseous HCN is produced in the midplane upon recombination of the H and CN ices). The resulting column densities through the mid-

plane are $\gtrsim 10^{13} \text{ cm}^{-2}$. Thus, in the fast 2D-mixing model column densities of warm and cold C_2H , CN, and HCN differ by only a factor of several, which further decreases outward. Using expression (19) and the LAMDA database, we estimate that the optically thin 1-0 rotational lines of C_2H , CN, and HCN are excited at densities of about $4 - 8 \cdot 10^5 \text{ cm}^{-3}$. Consequently, in the presence of strong turbulent mixing low-lying transitions of C_2H , CN, and HCN likely trace the cold midplane of DM Tau, supporting the observational evidence.

Finally, turbulent transport decreases CS column densities in the midplane region by a factor of $\lesssim 4$, simultaneously increasing it in the $T > 20$ K zone by up to 2 orders of magnitude. The chemistry of sulfur-bearing molecules is among the most altered by the mixing due to slow surface processes associated with these heavy species (see Section 4.5). However, even in the laminar model column densities of cold ($T < 20$ K) CS are lower than that of warm ($T > 20$ K) CS by an order of magnitude. The overall CS column densities in the outer disk are $\approx 3 \cdot 10^{11} - 3 \cdot 10^{12} \text{ cm}^{-2}$, and the low- J CS lines are optically thin. The critical densities of the excitation for the (2-1) and (3-2) CS transitions at 98 and 147 GHz are $\sim 5 \cdot 10^6$ and $2 \cdot 10^6 \text{ cm}^{-3}$, respectively. Therefore, if our model is correct, the kinetic temperatures derived from the low-lying CS emission lines should be above 20 K in the DM Tau disk.

Clearly, our modeling shows a potential of turbulent transport as a cause for the presence of molecules in the cold midplanes in T Tauri disks. The non-thermal broadening of the CO lines by $\lesssim 150 \text{ m s}^{-1}$ in the DM Tau system has been reported in Piétu et al. (2007), which corresponds to the turbulent velocities of $\lesssim 10\%$ of the sound speed. However, the increase in concentrations of the cold gases in our 2D-mixing model is not strong enough to rule out other explanations. First of all, more accurate modeling of the UV scattering toward the midplane would result in faster photoevaporation of ices in the lower molecular layer and upper midplane (van Zadelhoff et al. 2003; Hersant et al. 2009). Second, as mentioned in Aikawa (2007), moderate grain growth beyond 1 μm in disk central regions lengthens the depletion time for molecules such that the gas-phase CO abundances may remain high even after 1 Myr of the evolution. Indeed, Vasyunin et al. (2011) and Fogel et al. (2011) have modeled chemical evolution in disks taking grain evolution into account and found that the grain growth substantially decreases the depletion zones of molecules. Moreover, from analysis of the SED slopes in millimeter and centimeter wavelengths large grain sizes of 1 mm have been inferred for many young systems in various star-forming regions, including Taurus-Auriga association (e.g., Rodmann et al. 2006; Lommen et al. 2010; Ricci et al. 2010). The DM Tau disk has an inner hole of $\sim 4 - 20$ AU with grains as large as 1 mm, and hence is in a transitional phase (e.g., Calvet et al. 2005; Sargent et al. 2009; Andrews et al. 2011). From advanced theoretical models of grain coagulation, fragmentation, sedimentation, and turbulent stirring the grain evolution should proceed everywhere in the disk, though the mean grain sizes remain smaller in the outer disk compared to the inner disk region (e.g., Brauer et al. 2008; Birnstiel et al. 2010). Recently, Guilloteau et al. (2011) have used high-resolution, multi-frequency interferometric PdBI observations to discern more accurately the dust emissivity slopes at millimeter wavelengths in a sample of young stars. Their analysis has indeed shown that the outer disk of DM Tau contains large grains with sizes $\gtrsim 1 \mu\text{m}$. We advocate for a combined action of

turbulent transport and grain growth as a mechanism to maintain a sizable reservoir of cold gases in the DM Tau system.

$^{12}\text{CO}(3-2)$

5.3. Comparison with observations

Table 14
Observed and modeled column densities in DM Tau at 250 AU

Species	Observed	Refs	Modeled		
			Laminar	2D-mixing ($Sc = 100$)	2D-mixing ($Sc = 1$)
$^{12}\text{CO}^*$	3.0 (17)	(1)	3.0 (17)	3.0 (17)	3.0 (17)
HCO^+	1.7 (13)	(1,2)	8.0 (12)	1.2 (13)	2.5 (13)
H_2CO	1.0–2.0 (13)	(3)	6.2 (12)	6.7 (12)	4.0 (12)
N_2H^+	4.0 (11)	(2)	3.4 (11)	4.7 (11)	1.2 (12)
CS	4.0 (12)	(3)	8.1 (10)	1.1 (11)	5.6 (11)
CN	4.0 (13)	(4)	1.4 (13)	1.5 (13)	1.8 (13)
HCN	8.0 (12)	(4,5)	1.2 (13)	1.2 (13)	2.7 (13)
HNC	3.0 (12)	(4,5)	1.0 (13)	1.0 (13)	2.4 (13)
C_2H	3.0 (13)	(6)	1.1 (13)	1.3 (13)	1.4 (13)
Agreement**			7/8	7/8	6/8
* **					

References. — (1) Pietu et al. (2007); (2) Dutrey et al. (2007); (3) Dutrey et al. (2011, submitted); (4) Chapillon et al. (2011, submitted); (5) Schreyer et al. (2008); (6) Henning et al. (2010)

* The calculated column densities are scaled down to match the observed values for ^{12}CO . The renormalization factor is applied to the column densities of other species.

** Agreement is achieved when the observed and calculated column densities for a molecule do not differ by more than a factor of 4).

Table 15
Observed and modeled column densities of ices in DM Tau at $r = 10–30$ AU

Species	Relative abundance	Ref	10 AU	20 AU	30 AU
H_2O	100		100	100	100
CO	5–30	(1,2,3,4)	< 0.01	0.7	16
CO_2	3–20	(1,4)	10	20	0.6
H_2CO	0.04–1	(1,2,3,4)	0.02	0.015	< 0.01
CH_3OH	2	(2,3,4)	0	< 0.01	< 0.01
HCOOH	0.06–0.09	(3,4)	0.02	0	0
HCOOCH_3	0.06–0.08	(3,4)	0	0	0
CH_4	0.6–5	(1,3,4)	0	40	30
C_2H_2	0.1–0.5	(3,4)	0	0	0
C_2H_6	0.3–0.4	(3,4)	0.07	0	0
NH_3	0.1–2	(1,3,4)	33	20	15
HCN	≤ 0.25	(1,2,3,4)	12	3.6	0.5
HNC	0.01–0.04	(4,4)	0.5	0.02	0
HNCO	0.06–0.1	(3,4)	0	0	0
N_2	~ 0.02	(1)	0	0	0
CH_3CN	0.01–0.02	(3,4)	0	0	0
H_3CN	0.02	(3,4)	0.003	0	0
NH_2CHO	0.01–0.02	(3,4)	0	0	0
H_2S	0.75–1.5	(1,2,3,4)	0.15	0.09	0.06
CS	~ 0.1	(2)	0	0	0
SO	0.2–0.8	(1,3,4)	0	0	0
SO_2	0.1–0.2	(1,3,4)	0	0	0
OCS	0.1–0.4	(1,3,4)	0	0	0
H_2CS	0.02	(3,4)	0.006	0	0
S_2	0.005	(4)	0	0	0

References. — (1) Aikawa et al. (1999); (2) Biver et al. (1999); (3) Bockelée-Morvan et al. (2000); (4) Crovisier & Bockelée-Morvan (1999)

(Molecules in protoplanetary disks) Some previous studies of the laminar disk chemistry have reported reasonable quantitative agreement with observationally-inferred column densities (e.g., Aikawa et al. 2002; Semenov et al. 2005; Dutrey et al. 2007b; Schreyer et al. 2008). On the other hand, the radial profiles of the column densities derived from fitting

high-resolution interferometric data have not been fully reproduced by conventional disk models. In the 1D-vertical mixing study of Willacy et al. (2006) the modeling results have been compared with single-dish and interferometric observations of several molecules in the disks around DM Tau, LkCa 15, and TW Hya. The good agreement between theoretical and observed column densities for the fast mixing model has been inferred from the single-dish data, whereas the interferometric data have not been reproduced. Calculating infrared emission lines for the disk model with radial advective and vertical mixing transport, Heinzeller et al. (2011) have shown that it improves agreement with the *Spitzer* observations of the inner disks around AA Tau, DR Tau, and AS 205, compared to predictions of the laminar chemical model.

We compile a table with column densities at 250 AU derived from the analysis of high-quality PdBI interferometric observations and compare them with the results of our laminar, slow, and fast 2D-mixing models (see Table 14). Calculated column densities have intrinsic uncertainties of a factor $\sim 3–5$, caused by reaction rate uncertainties (Vasyunin et al. 2008), whereas observational data suffer from calibration inaccuracies ($\sim 10–20\%$), distance uncertainties (10–20%), etc. Therefore, we assume that the agreement is good when observed and modeled values differ by a factor of $\lesssim 4$ and bad otherwise. The disk total surface density cannot be accurately derived from the continuum data, as these suffer from poorly known dust opacities at (sub)-millimeter wavelengths that can vary by factors of several (Semenov et al. 2003). Instead, the observed CO column density distribution can be used as a proxy to the disk gas density structure. The problem here is that the ^{12}CO rotational lines are optically thick and thus probe localized disk region, whereas from optically thin CO isotopologue lines the total CO column densities can only be recovered if $^{12}\text{C}/^{13}\text{C}$ or $^{16}\text{O}/^{18}\text{O}$ isotope ratios are known. We use ^{13}CO and ^{12}CO column densities obtained for the outer DM Tau disk from the interferometric observations by Piétu et al. (2007) and constrain the total CO column density at 250 AU to $\approx 3 \cdot 10^{17} \text{ cm}^{-2}$. The corresponding theoretical value is almost the same in the laminar and mixing models, $N(\text{CO}) \approx 10^{18} \text{ cm}^{-2}$ (Fig. 9). To match this value, modeled column densities in Table 14 were renormalized accordingly.

Unlike Willacy et al. (2006), all the considered models match quite well the observed column densities, apart from

the CS data. The stellar and disk parameters are well known for the nearby DM Tau system, so its physical structure can be reliably reconstructed. The detected species are simple and their chemical evolution is governed by a limited amount of mostly gas-phase processes, with many accurately acquired rate constants. However, CS column densities are underpredicted by factors of $\sim 7 - 50$, though situation considerably improves for the fast 2D-mixing model. Dutrey et al. (2011, submitted) have observed SO, H₂S, and CS in DM Tau, LkCa 15, and MWC 480 with the IRAM 30-m and PdBI interferometer. They have derived upper limits for H₂S and SO in the DM Tau disk at 300 AU, namely, $N(\text{H}_2\text{S}) \lesssim 2 \cdot 10^{11} \text{ cm}^{-2}$ and $N(\text{SO}) \lesssim 8 \cdot 10^{11} \text{ cm}^{-2}$, whereas CS has been firmly detected with the column density of $N(\text{CS}) \lesssim 3.5 \cdot 10^{12} \text{ cm}^{-2}$. Dutrey et al. have found that the sulfur content of the three disks cannot be explained by modern chemical models as these result in higher abundances of H₂S and SO compared to the CS abundances. This is also the case in our modeling. While having too less CS, our disk models overproduce column densities of sulfur monoxide and hydrogen sulfide. The reason for such a disagreement, as we discussed in Section 4.5, is that the sulfur chemistry is hampered by poorly known reaction data and may lack key reactions, and the depletion of elemental sulfur from the gas is also crudely constrained.

Generally, the fast 2D-mixing model produces more molecules per CO compared to the laminar disk chemistry, and overproduces HNC with respect to the observations. The utilized chemical network leads to the synthesis of hydrogen cyanide and isocyanide with almost equal probability in the all disk models. On the other hand, the observed column density of HCN is higher than that of HNC by a factor of $\sim 2 - 3$. The HCN/HNC ratios of $\lesssim 1$ are typical for dark, dense cores (Tennekes et al. 2006; Hily-Blant et al. 2010), while in irradiated environments like PDR regions this ratio exceeds 1 (e.g., Loenen et al. 2008). Indeed, in the study of Fogel et al. (2011) with accurate description of the UV RT including the L _{α} radiation and the moderate grain growth the resulting ratio of HCN/HNC is about 1.5. The HCN/HNC ratio of 3 has been obtained by Vasyunin et al. (2011) for the disk model with consistently calculated grain evolution and the UV penetration. An increase in the HCN/HNC ratio to 3-5 due to lowering the disk mass or including dust sedimentation has been reported by Aikawa & Herbst (1999). Furthermore, Sarrasin et al. (2010) have accurately calculated the collisional data for HCN and HNC with He and found that the use of the HCN rates to interpret HNC observations in dark clouds may lead to the underestimation of the HCN/HNC ratio. Apparently, the use of ISM-like dust grains or the crude approach to calculate UV penetration utilized in our disk model make the UV opacities too high in the molecular layer to result in HCN/HNC > 1.

Column densities or upper limits have also been reported for other species. Using the IRAM 30-m antenna, Dutrey et al. (1997) have not been able to detect molecular lines of SiO, SiS, HC₃N, C₃H₂, CH₃OH, CO⁺, SO₂, HNCS, HCOOCH₃ in DM Tau. Among these species, only SiO, C₃H₂, and SO₂ have large modeled column densities between 10¹² and 10¹³ cm⁻² at 250 AU. The SO₂ lacks permanent dipole moment and has no pure rotational spectra, unless oxygen atoms are isotopically different. Its ro-vibrational lines are excited at $T \gtrsim 50 - 100$ K, so that the emission arises only from an inner disk region ($r \lesssim 5 - 10$ AU). The C₃H₂ molecule can be in ortho- or para-state (e.g., Madden et al.

1989; Morisawa et al. 2006), though in our model these details are not taken into account. The linear isomer H₂CCC (propadienylidene) has a large dipole moment of about 4 D and rotational spectrum starting at cm wavelengths. However, the IRAM 30-m observations of TMC1 and IRC +10216 by Cernicharo et al. (1991) have revealed that the abundance of the linear isomer is only $\sim 1\%$ of that of the cyclopropenylidene. The cyclic isomer has a rich ro-vibrational spectrum, with emission lines at (sub-)millimeter wavelengths that are excited at $n_{\text{cr}} \sim 10^6 \text{ cm}^{-3}$ (LAMDA database; Green et al. 1987; Schöier et al. 2005). Due to energy partition the individual lines are not as strong as in the case of HCO⁺, making them hard to detect. Finally, the outflow tracer, SiO, has a dipole moment of 3.1 D and strong rotational lines at (sub-)mm, excited at $\sim 10^5 \text{ cm}^{-3}$ (Schöier et al. 2005). The calculated column density of SiO at 250 AU is $4 \cdot 10^{12} \text{ cm}^{-2}$ in the laminar model and 10^{13} cm^{-2} in the fast 2D-mixing model. These values are sensitive to the abundance of the elemental silicon remained in the gas and may not be representative of DM Tau in the “low metals” set of initial abundances of Lee et al. (1998a) adopted in our modeling.

The recent non-detection/tentative detection of cold water vapor in the DM Tau disk by the *Herschel*/HIFI have been reported by Bergin et al. (2010). They have interpreted the observational data with an advanced chemical disk and the line radiative transfer model, and inferred the disk-averaged water column densities within $\sim 5 \cdot 10^{12} - 3 \cdot 10^{13} \text{ cm}^{-2}$. Our calculated disk-averaged H₂O column densities are $5 \cdot 10^{14} \text{ cm}^{-2}$ and $2 \cdot 10^{15} \text{ cm}^{-2}$ in the laminar and fast mixing models, respectively. Therefore, all our models overestimate the abundance of gaseous water in DM Tau by a factor of at least 15. Similarly large values have been obtained in the studies of disk chemistry with grain evolution by Vasyunin et al. (2011) and Fogel et al. (2011). Bergin et al. have concluded that most water ice is trapped in large dust grain aggregates that sedimented toward the DM Tau midplane and thus cannot be easily photodesorbed. However, if this is the case, other molecules like CO, CN, etc. have to be depleted from the gas phase much more severely, and should not be present in the cold midplane. The presence of large reservoir of cold CO, CN, HCN, C₂H observed in the DM Tau midplane contradicts with such hypothesis, unless other molecules begin accreting onto dust grains later than water, when grains are already large, $\gtrsim 1 \mu\text{m}$.

(*Molecules in comets of the Solar system*) We calculate column densities of ices at 10, 20, and 30 AU and compare them with molecules observed in comets as done in Aikawa et al. (1999), see Table 15. Observed values are taken from Aikawa et al. (1999); Biver et al. (1999); Bockelée-Morvan et al. (2000); Crovisier & Bockelée-Morvan (1999, and references therein). The difference in calculated ice column densities between the laminar and mixing models is smaller than their radial variations, so in Table 15 only results of the laminar model are presented. The comets have formed in the early Solar nebula at distances of $\gtrsim 10 - 20$ AU and later have been expelled outwards (Lissauer 1987). Comets are reservoirs of pristine compounds, and their chemical composition is indicative of evolutionary history of the outer Solar system during the first several million years (e.g., Ehrenfreund & Charnley 2000). However, molecules detected in their comae can be partly photodissociated or are products of immediate coma chemistry and very long irradiation of bulk cometary ices

by cosmic ray particles, so direct comparison with model predictions is not straightforward. The presence of both reduced and oxidized ices in comets have been explained by Aikawa et al. (1999) as due to CRP-ionization of the disk, whereas in cosmochemical models the Fischer-Tropsch catalysis or cloud-nebula evolutionary scenario have been invoked (e.g., Greenberg 1982; Prinn & Fegley 1989). We find that our disk model incorporating the high-energy radiation is able to reproduce relatively high abundances of water, CO, and CO₂ ices, as well as abundances of CH₄ and C₂H₆ ices. Also, abundances of H₂CO, HCOOH, HCN, HNC, H₂S, and H₂CS are reproduced. However, the model overproduces NH₃ ice by a factor of $\gtrsim 7$, and severely underpredicts abundances of most of the sulfur-bearing ices (CS, SO, SO₂, OCS, S₂) and complex organics (CH₃OH, HCOOCH₃, HNCO, NH₂CHO). The chemical model with fast turbulent transport gives better results for heavy sulfur-bearing and organic molecules, but is still far below the observed values. As we discussed above, the sulfur chemistry is rather dubious in modern astrochemical databases. The adopted chemical network has a limited number of surface reactions leading to complex organic molecules and not many endothermic neutral-neutral reactions. Calculated ice abundances are also sensitive to the adopted binding energies, many of which are not accurately derived.

Apart from that, we conclude, that our disk chemical models with and without transport processes are equally and reasonably well agree to the high-quality interferometric observations of DM Tau and the chemical composition of comets in the Solar system.

5.4. Observable molecular tracers of dynamical processes

Table 16
Detectable tracers of turbulent mixing

Steadfast	Hypersensitive
CO	Heavy hydrocarbons (e.g., C ₆ H ₆)
H ₂ O ice	C ₂ S
	C ₃ S
	CO ₂
	O ₂
	SO
	SO ₂
	OCN
	Complex organics (e.g., HCOOH)

In Table 16 we show most promising tracers of transport processes in protoplanetary disks as found with our modeling. The quantity least biased by observational and modeling uncertainties is the ratio of the observed column densities of an abundant steadfast species to that of a hypersensitive molecule. Among the insensitive species (Table 5) the most promising are CO and the water ice as these terminal species incorporate substantial fractions of the elemental carbon and oxygen in disks, and are easy to observe. Cold molecular hydrogen is not observable, whereas concentrations of C⁺, light hydrocarbons, CN, HCN, and HNC are more sensitive not to mixing, but to the stellar X-ray and UV radiation (e.g., Fogel et al. 2011; Aresu et al. 2011; Kamp et al. 2011). Other molecules and ices unresponsive to mixing have low abundances or also model-dependent (e.g., S-bearing ices). Both pure rotational CO lines at (sub-)mm

and ro-vibrational CO lines at IR wavelengths have been detected in inner and outer disk regions (e.g., Pi  tu et al. 2007; Oberg et al. 2011; Salyk et al. 2011). Water ice absorption feature at 3 μ m has also been detected in protoplanetary disks (e.g., Terada et al. 2007) and envelopes around young protostars (e.g., Boogert et al. 2008).

Among species sensitive and hypersensitive to the turbulent transport (Tables 6–7) most promising are gaseous and solid heavy hydrocarbons, C₂S, C₃S, SO, SO₂, CO₂, O₂, and complex organic molecules (e.g., HCOOH). Basically, any non-terminal, abundant molecule produced mostly via grain-surface kinetics can be used as a tracer of dynamical transport in protoplanetary disks. The OH⁺ and H₂O⁺ ions are sensitive to the disk ionization structure and thus cannot be reliable tracers of turbulent mixing. Due to atmospheric opacity, molecular oxygen can only be observed from space (e.g., Larsson et al. 2007). Gas-phase molecules actually detected in disks are warm CO₂ at IR (e.g., Salyk et al. 2011) and SO at millimeter wavelengths (Fuente et al. 2010). Rotational lines of C₂S, C₃S and various hydrocarbons and hydrocarbon anions have been detected in cold dense cores (e.g., Dickens et al. 2001; Kalenskii et al. 2004; Sakai et al. 2010). The emission lines of SO, SO₂, and several organic molecules have been identified in submillimeter spectra of young stellar objects (e.g., J  rgensen et al. 2005). CO₂ ice feature at 15.2 μ m has been detected in molecular clouds (e.g., Kim et al. 2011) and toward embedded young low-mass stars (e.g., Pontoppidan et al. 2008b). In addition, plethora of other ices like CH₄, SO₂, HCOOH, H₂CO, and CH₃OH have been observed in Class I/II objects (e.g., Zasowski et al. 2009).

The column density ratios of these sensitive molecules to the steadfast CO and H₂O ice vary between our laminar and fast 2D-mixing models by 2–4 orders of magnitude (see CDR values in Table 7). In the not so far distant future forthcoming observational facilities like ALMA, extended VLA, and James Webb Space Telescope will allow us to observe many of the mixing tracers along with CO and water ice in nearby protoplanetary disks of various ages, masses, and sizes, and testify our predictions.

6. SUMMARY AND CONCLUSIONS

We study the influence of dynamical processes on the chemical evolution of protoplanetary disks. Our analysis is based on the 2D flared α -model of a ~ 5 Myr DM Tau disk coupled to the large-scale gas-grain chemical code. To account for production of complex molecules, the chemical network is supplied with a set of surface reactions (up to HCOOH, CH₃OH, CH₃OCH₃, etc.) and photoprocessing of ices. For the first time our disk model covers a wide range of radii, 10–800 AU, and includes warm planet-forming zone and cold outer region. Turbulent transport of gases and ices is modeled using the mixing-length approximation in full 2D (based on the α -prescription for viscosity). Since turbulent transport efficiency of molecules in disks is not well known, we consider two dynamical models with the Schmidt number of 1 and 100. We come up with a simple analysis for laminar chemical models that allows to highlight the potential sensitivity of a molecule to turbulent transport. It is shown that the higher the ratio of the characteristic chemical timescale to the turbulent transport timescale for a given molecule, the higher the probability that its column density will be affected by dynamical processes. With our chemo-dynamical models, we find that the turbulent transport influences abundances and column densities of many gas-phase species and especially

ices. The results of the chemical model with reduced turbulent diffusion are much closer to those from the laminar model, but not completely. Mixing is important in disks since a chemical steady-state is not reached for many species due to long timescales associated with surface chemical processes and slow evaporation of heavy molecules ($t \gtrsim 10^5$ years). When a grain with an icy mantle is transported from a cold disk midplane into a warm intermediate/inner region, the warm-up makes heavy radicals mobile on dust surface, enriching the mantle with complex ices, which can be released into the gas in appropriate temperature regions. In contrast, simple radicals and molecular ions, which chemical evolution proceed solely in the gas phase, are not much affected by dynamics. We divide all molecules into 3 distinct groups with respect to the sensitivity of their column densities to the diffusive mixing. The molecules that are unresponsive to dynamical transport include such observed and potentially detectable molecules as C₂H, C⁺, CH₄, CN, CO, HCN, HNC, H₂CO, OH, as well as water and ammonia ices. Their column densities computed with the laminar and fast 2D-mixing model do not differ by more than the factor of 2–5 (“steadfast” species). The molecules which vertical column densities in the laminar and dynamical models differ by no more than 2 order of magnitude include, e.g., C₂H₂, some carbon chains, CS, H₂CS, H₂O, HCO⁺, HCOOH, HNCO, N₂H⁺, NH₃, CO ice, H₂CO ice, CH₃OH ice, and electrons (“sensitive” species). Molecules which column densities are modified by diffusion by more than 2 orders of magnitude include, e.g., C₂S, C₃S, C₆H₆, CO₂, O₂, SiO, SO, SO₂, long carbon chain ices, CH₃CHO ice, HCOOH ice, O₂ ice, and OCN ice (“hypersensitive” species). The sulfur-bearing molecules, along with polyatomic (organic) molecules frozen onto the dust grains, are among the most sensitive species to the turbulent mixing. The chemical evolution of assorted molecules in the laminar and turbulent models is thoroughly analyzed and compared with previous studies. We find that the observed column densities in the DM Tau disk are well reproduced by both the laminar and the mixing disk models. The observed abundances of reduced and oxidized cometary ices are also successfully reproduced by the both models. A combination of efficient UV photodesorption, grain growth, and turbulent mixing leads to non-negligible amount of molecular gases in the cold disk midplane. We propose several observable or potentially detectable tracers of dynamical processes in protoplanetary disks, e.g. ratios of the CO₂, O₂, SO, SO₂, C₂S, C₃S column densities to that of CO and the water ice. Some of these tracers have been observed in disks by the current radiointerferometers and infrared facilities (e.g. PdBI, SMA, Spitzer, Keck, VLT) and some will be targeted by the *Herschel* telescope. The detection of complex species (e.g., dimethyl ether, formic acid, methyl formate, etc.) in protoplanetary disks with ALMA and JWST will be a strong indication that chemical evolution of these objects is influenced by transport processes.

This research made use of NASA’s Astrophysics Data System. DS acknowledges support by the *Deutsche Forschungsgemeinschaft* through SPP 1385: “The first ten million years of the solar system - a planetary materials approach” (SE 1962/1-1). DW acknowledges support from the the Federal Targeted Program “Scientific and Educational Human Resources of Innovation-Driven Russia” for 2009–2013.

REFERENCES

- Agúndez, M., Cernicharo, J., & Goicoechea, J. R. 2008, A&A, 483, 831
 Aikawa, Y. 2007, ApJ, 656, L93
 Aikawa, Y., & Herbst, E. 1999, A&A, 351, 233
 Aikawa, Y., Momose, M., Thi, W.-F., van Zadelhoff, G.-J., Qi, C., Blake, G. A., & van Dishoeck, E. F. 2003, PASJ, 55, 11
 Aikawa, Y., & Nomura, H. 2006, ApJ, 642, 1152
 Aikawa, Y., Umebayashi, T., Nakano, T., & Miyama, S. M. 1999, ApJ, 519, 705
 Aikawa, Y., van Zadelhoff, G. J., van Dishoeck, E. F., & Herbst, E. 2002, A&A, 386, 622
 Andersson, S., Al-Halabi, A., Kroes, G., & van Dishoeck, E. F. 2006, J. Chem. Phys., 124, 064715
 Andersson, S., & van Dishoeck, E. F. 2008, A&A, 491, 907
 Andrews, S., Wilner, D., Espaillat, C., Hughes, A. M., Dullemond, C. P., McClure, M. K., Qi, C., & Brown, J. M. 2011, ArXiv e-prints
 Andrews, S. M., & Williams, J. P. 2007, ApJ, 659, 705
 Aresu, G., Kamp, I., Meijerink, R., Woitke, P., Thi, W., & Spaans, M. 2011, A&A, 526, A163+
 Armitage, P. J., Clarke, C. J., & Palla, F. 2003, MNRAS, 342, 1139
 Balbus, S. A., & Hawley, J. F. 1991, ApJ, 376, 214
 Bauer, I., Finocchi, F., Duschl, W. J., Gail, H.-P., & Schloeder, J. P. 1997, A&A, 317, 273
 Belloche, A., Menten, K. M., Comito, C., Müller, H. S. P., Schilke, P., Ott, J., Thorwirth, S., & Hieret, C. 2008, A&A, 482, 179
 Bennett, C. J., Jones, B., Knox, E., Perry, J., Kim, Y. S., & Kaiser, R. I. 2010, ApJ, 723, 641
 Bergin, E., Calvet, N., D’Alessio, P., & Herczeg, G. J. 2003, ApJ, 591, L159
 Bergin, E. A., Aikawa, Y., Blake, G. A., & van Dishoeck, E. F. 2007, in Protostars and Planets V, ed. B. Reipurth, D. Jewitt, & K. Keil, 751–766
 Bergin, E. A., et al. 2010, A&A, 521, L33+
 Bethell, T. J., Zweibel, E. G., & Li, P. S. 2007, ApJ, 667, 275
 Birnstiel, T., Dullemond, C. P., & Brauer, F. 2010, A&A, 513, A79+
 Bisschop, S. E., Fraser, H. J., Öberg, K. I., van Dishoeck, E. F., & Schlemmer, S. 2006, A&A, 449, 1297
 Biver, N., et al. 1999, AJ, 118, 1850
 Bockelée-Morvan, D., et al. 2000, A&A, 353, 1101
 Boogert, A. C. A., et al. 2008, ApJ, 678, 985
 Boss, A. P. 2004, ApJ, 616, 1265
 Bouwman, J., Cuppen, H. M., Steglich, M., Allamandola, L. J., & Linnartz, H. 2011, A&A, 529, A46+
 Bradley, J. P. 2005, in Meteorites, Comets and Planets: Treatise on Geochemistry, Volume 1, ed. A. M. Davis, H. D. Holland, & K. K. Turekian (Elsevier B), 689–
 Brauer, F., Dullemond, C. P., & Henning, T. 2008, A&A, 480, 859
 Brownlee, D. E., Joswiak, D. J., Matrajt, G., Bradley, J. P., & Ebel, D. S. 2008, in Lunar and Planetary Institute Conference Abstracts, Vol. 39, Lunar and Planetary Institute Conference Abstracts, 1978–
 Brownlee, D. E., et al. 2004, Science, 304, 1764
 Buch, V., & Devlin, J. P. 1994, ApJ, 431, L135
 Busemann, H., Young, A. F., O’D. Alexander, C. M., Hoppe, P., Mukhopadhyay, S., & Nittler, L. R. 2006, Science, 312, 727
 Calvet, N., et al. 2005, ApJ, 630, L185
 Cameron, A. G. W. 1995, Meteoritics, 30, 133
 Cant, R. S., & Mastorakis, E. 2008 (Cambridge University Press, UK), 1–178
 Carr, J. S., & Najita, J. R. 2008, Science, 319, 1504
 Cassen, P., & Moosman, A. 1981, Icarus, 48, 353
 Cazaux, S., Caselli, P., Tielens, A. G. G. M., LeBourlot, J., & Walmsley, M. 2005, Journal of Physics Conference Series, 6, 155
 Cernicharo, J., Gottlieb, C. A., Guélin, M., Killian, T. C., Paubert, G., Thaddeus, P., & Vrtilek, J. M. 1991, ApJ, 368, L39
 Cernicharo, J., Kahane, C., Guélin, M., & Hein, H. 1987, A&A, 181, L9
 Chiang, E. I., & Goldreich, P. 1997, ApJ, 490, 368
 Churchwell, E., Walmsley, C. M., & Cesaroni, R. 1990, A&AS, 83, 119
 Ciesla, F. J. 2009, Icarus, 200, 655
 Clayton, R. N. 1993, Annual Review of Earth and Planetary Sciences, 21, 115
 Clayton, R. N., & Mayeda, T. K. 1996, Geochim. Cosmochim. Acta, 60, 1999
 Crabtree, K. N., Indriolo, N., Kreckel, H., Tom, B. A., & McCall, B. J. 2011, ApJ, 729, 15
 Crovisier, J., & Bockelée-Morvan, D. 1999, Space Sci. Rev., 90, 19
 Cuppen, H. M., & Hornekær, L. 2008, J. Chem. Phys., 128, 174707
 Cuppen, H. M., van Dishoeck, E. F., Herbst, E., & Tielens, A. G. G. M. 2009, A&A, 508, 275
 Cyr, K. E., Sears, W. D., & Lunine, J. I. 1998, Icarus, 135, 537
 D’Alessio, P., Calvet, N., Hartmann, L., Lizano, S., & Cantó, J. 1999, ApJ, 527, 893
 Dartois, E., Dutrey, A., & Guilloteau, S. 2003, A&A, 399, 773
 d’Hendecourt, L. B., Allamandola, L. J., & Greenberg, J. M. 1985, A&A, 152, 130
 Dickens, J. E., Langer, W. D., & Velusamy, T. 2001, ApJ, 558, 693
 Draine, B. T. 1978, ApJS, 36, 595
 Draine, B. T., & Bertoldi, F. 1996, ApJ, 468, 269
 Dullemond, C. P., & Dominik, C. 2004, A&A, 417, 159

- Duschl, W. J., Gail, H., & Tscharnutter, W. M. 1996, *A&A*, 312, 624
- Dutrey, A., Guilloteau, S., & Guelin, M. 1997, *A&A*, 317, L55
- Dutrey, A., Guilloteau, S., & Ho, P. 2007a, in *Protostars and Planets V*, ed. B. Reipurth, D. Jewitt, & K. Keil, 495–506
- Dutrey, A., et al. 2007b, *A&A*, 464, 615
- . 2008, *A&A*, 490, L15
- Dzyurkevich, N., Flock, M., Turner, N. J., Klahr, H., & Henning, T. 2010, *A&A*, 515, A70+
- Ehrenfreund, P., & Charnley, S. B. 2000, *ARA&A*, 38, 427
- Elsila, J. E., Glavin, D. P., & Dworkin, J. P. 2009, *Meteoritics and Planetary Science*, 44, 1323
- Finocchi, F., Gail, H.-P., & Duschl, W. J. 1997, *A&A*, 325, 1264
- Fleming, T., & Stone, J. M. 2003, *ApJ*, 585, 908
- Florescu-Mitchell, A. I., & Mitchell, J. B. A. 2006, *Phys. Rep.*, 430, 277
- Flynn, G. J., et al. 2006, *Science*, 314, 1731
- Fogel, J. K. J., Bethell, T. J., Bergin, E. A., Calvet, N., & Semenov, D. 2011, *ApJ*, 726, 29
- Fraser, H. J., Bisschop, S. E., Pontoppidan, K. M., Tielens, A. G. G. M., & van Dishoeck, E. F. 2005, *MNRAS*, 356, 1283
- Fromang, S., Terquem, C., & Balbus, S. A. 2002, *MNRAS*, 329, 18
- Fuchs, G. W., Cuppen, H. M., Ioppolo, S., Romanzin, C., Bisschop, S. E., Andersson, S., van Dishoeck, E. F., & Linnartz, H. 2009, *A&A*, 505, 629
- Fuente, A., Cernicharo, J., Agúndez, M., Berné, O., Goicoechea, J. R., Alonso-Albi, T., & Marcelino, N. 2010, *A&A*, 524, A19+
- Fukagawa, M., et al. 2004, *ApJ*, 605, L53
- Gail, H.-P. 1998, *A&A*, 332, 1099
- . 2001, *A&A*, 378, 192
- . 2002, *A&A*, 390, 253
- . 2004, *A&A*, 413, 571
- Gammie, C. F. 1996, *ApJ*, 457, 355
- Garcia, R. R., & Solomon, S. 1983, *J. Geophys. Res.*, 88, 1379
- Garrod, R. T., & Herbst, E. 2006, *A&A*, 457, 927
- Garrod, R. T., Wakelam, V., & Herbst, E. 2007, *A&A*, 467, 1103
- Garrod, R. T., Weaver, S. L. W., & Herbst, E. 2008, *ApJ*, 682, 283
- Glassgold, A. E., Feigelson, E. D., Montmerle, T., & Wolk, S. 2005, in *Astronomical Society of the Pacific Conference Series*, Vol. 341, *Chondrites and the Protoplanetary Disk*, ed. A. N. Krot, E. R. D. Scott, & B. Reipurth, 165–+
- Glassgold, A. E., Meijerink, R., & Najita, J. R. 2009, *ApJ*, 701, 142
- Glassgold, A. E., Najita, J., & Igea, J. 1997a, *ApJ*, 480, 344
- . 1997b, *ApJ*, 485, 920
- Glauser, A. M., Güdel, M., Watson, D. M., Henning, T., Schegerer, A. A., Wolf, S., Audard, M., & Baldovin-Saavedra, C. 2009, *A&A*, 508, 247
- Glavin, D. P., et al. 2010, *Meteoritics and Planetary Science*, 45, 1695
- Goicoechea, J. R., Pety, J., Gerin, M., Teyssier, D., Roueff, E., Hily-Blant, P., & Baek, S. 2006, *A&A*, 456, 565
- Gorti, U., Dullemond, C. P., & Hollenbach, D. 2009, *ApJ*, 705, 1237
- Gorti, U., & Hollenbach, D. 2004, *ApJ*, 613, 424
- Green, S., Defrees, D. J., & McLean, A. D. 1987, *ApJS*, 65, 175
- Greenberg, J. M. 1973, in *Molecules in the Galactic Environment*, ed. M. Gordon & L. Snyder (New York, John Wiley and Sons), 93–142
- Greenberg, J. M. 1982, in *IAU Colloq. 61: Comet Discoveries, Statistics, and Observational Selection*, ed. L. L. Wilkening, 131–163
- Guilloteau, S., Dutrey, A., Piétu, V., & Boehler, Y. 2011, *A&A*, 529, A105+
- Harada, N., Herbst, E., & Wakelam, V. 2010, *ApJ*, 721, 1570
- Hasegawa, T. I., & Herbst, E. 1993, *MNRAS*, 263, 589
- Hasegawa, T. I., Herbst, E., & Leung, C. M. 1992, *ApJS*, 82, 167
- Heinzeller, D., Nomura, H., Walsh, C., & Millar, T. J. 2011, *ApJ*, 731, 115
- Helling, C., & Lucas, W. 2009, *MNRAS*, 398, 985
- Henning, T., et al. 2010, *ApJ*, 714, 1511
- Herbst, E., & van Dishoeck, E. F. 2009, *ARA&A*, 47, 427
- Hersant, F., Gautier, D., & Huré, J.-M. 2001, *ApJ*, 554, 391
- Hersant, F., Wakelam, V., Dutrey, A., Guilloteau, S., & Herbst, E. 2009, *A&A*, 493, L49
- Hily-Blant, P., Walmsley, M., Pineau Des Forêts, G., & Flower, D. 2010, *A&A*, 513, A41+
- Hirose, S., & Turner, N. J. 2011, *ArXiv e-prints*
- Hughes, A. M., Wilner, D. J., Andrews, S. M., Qi, C., & Hogerheijde, M. R. 2011, *ApJ*, 727, 85
- Hughes, A. M., et al. 2009, *ApJ*, 698, 131
- Ilgner, M., Henning, T., Markwick, A. J., & Millar, T. J. 2004, *A&A*, 415, 643
- Ilgner, M., & Nelson, R. P. 2006c, *A&A*, 445, 205
- . 2006a, *A&A*, 445, 223
- . 2006b, *A&A*, 455, 731
- . 2008, *A&A*, 483, 815
- Ioppolo, S., van Boechemen, Y., Cuppen, H. M., van Dishoeck, E. F., & Linnartz, H. 2011, *MNRAS*, 238
- Irvine, W. M., et al. 1989, *ApJ*, 342, 871
- Jessberger, E. K., Christoforidis, A., & Kissel, J. 1988, *Nature*, 332, 691
- Jijina, J., Myers, P. C., & Adams, F. C. 1999, *ApJS*, 125, 161
- Jørgensen, J. K., Bourke, T. L., Myers, P. C., Schöier, F. L., van Dishoeck, E. F., & Wilner, D. J. 2005, *ApJ*, 632, 973
- Jørgensen, J. K., & van Dishoeck, E. F. 2010, *ApJ*, 710, L72
- Juhász, A., et al. 2010, *ApJ*, 721, 431
- Kalenskii, S. V., Slysh, V. I., Goldsmith, P. F., & Johansson, L. E. B. 2004, *ApJ*, 610, 329
- Kaltenegger, L., Traub, W. A., & Jucks, K. W. 2007, *ApJ*, 658, 598
- Kamp, I., & Dullemond, C. P. 2004, *ApJ*, 615, 991
- Kamp, I., Woitke, P., Pinte, C., Tilling, I., Thi, W., Menard, F., Duchene, G., & Augereau, J. 2011, *ArXiv e-prints*
- Kastner, J. H., Zuckerman, B., Weintraub, D. A., & Forveille, T. 1997, *Science*, 277, 67
- Katz, N., Furman, I., Biham, O., Pirronello, V., & Vidali, G. 1999, *ApJ*, 522, 305
- Keller, C., & Gail, H. 2004, *A&A*, 415, 1177
- Kim, H. J., et al. 2011, *ApJ*, 729, 84
- Kress, M. E., Tielens, A. G. G. M., & Frenklach, M. 2010, *Advances in Space Research*, 46, 44
- Kristensen, L. E., Amiaud, L., Fillion, J., Dulieu, F., & Lemaire, J. 2011, *A&A*, 527, A44+
- Lahuis, F., et al. 2006, *ApJ*, 636, L145
- Larson, R. B. 2003, *Reports of Progress in Physics*, 66, 1651
- Larsson, B., et al. 2007, *A&A*, 466, 999
- Le Teuff, Y. H., Millar, T. J., & Markwick, A. J. 2000, *A&AS*, 146, 157
- Lee, H.-H., Herbst, E., Pineau des Forets, G., Roueff, E., & Le Bourlot, J. 1996, *A&A*, 311, 690
- Lee, H.-H., Roueff, E., Pineau des Forets, G., Shalabiea, O. M., Terzieva, R., & Herbst, E. 1998a, *A&A*, 334, 1047
- Lee, T., Shu, F. H., Shang, H., Glassgold, A. E., & Rehm, K. E. 1998b, *ApJ*, 506, 898
- Lee, T. J. 1972, *Nature*, 237, 99
- Leger, A., Jura, M., & Omont, A. 1985, *A&A*, 144, 147
- Lissauer, J. J. 1987, *Icarus*, 69, 249
- Lodders, K. 2003, *ApJ*, 591, 1220
- Loenen, A. F., Spaans, M., Baan, W. A., & Meijerink, R. 2008, in *EAS Publications Series*, Vol. 31, *EAS Publications Series*, ed. C. Kramer, S. Aalto, & R. Simon, 183–185
- Lommen, D. J. P., et al. 2010, *A&A*, 515, A77+
- Lovrics, A., Csikasz-Nagy, A., Zsely, I., Zador, J., Turanyi, T., & Novak, B. 2006, *BMC Bioinformatics*, 7, 494
- Lynden-Bell, D., & Pringle, J. E. 1974, *MNRAS*, 168, 603
- Lyons, J. R., & Young, E. D. 2005, *Nature*, 435, 317
- Madden, S. C., Irvine, W. M., Swade, D. A., Matthews, H. E., & Friberg, P. 1989, *AJ*, 97, 1403
- Maloney, P. R., Hollenbach, D. J., & Tielens, A. G. G. M. 1996, *ApJ*, 466, 561
- Markwick, A. J., Ilgner, M., Millar, T. J., & Henning, T. 2002, *A&A*, 385, 632
- Mazzitelli, I. 1989, in *European Southern Observatory Conference and Workshop Proceedings*, Vol. 33, *European Southern Observatory Conference and Workshop Proceedings*, ed. B. Reipurth, 433–445
- Meijerink, R., Glassgold, A. E., & Najita, J. R. 2008, *ApJ*, 676, 518
- Meijerink, R., & Spaans, M. 2005, *A&A*, 436, 397
- Millar, T. J., Farquhar, P. R. A., & Willacy, K. 1997, *A&AS*, 121, 139
- Morfill, G. E. 1983, *Icarus*, 53, 41
- Morfill, G. E., & Völk, H. J. 1984, *ApJ*, 287, 371
- Morgan, Jr., W. A., Feigelson, E. D., Wang, H., & Frenklach, M. 1991, *Science*, 252, 109
- Morisawa, Y., et al. 2006, *ApJ*, 642, 954
- Najita, J., Bergin, E. A., & Ultom, J. N. 2001, *ApJ*, 561, 880
- Najita, J. R., Carr, J. S., Strom, S. E., Watson, D. M., Pascucci, I., Hollenbach, D., Gorti, U., & Keller, L. 2010, *ApJ*, 712, 274
- Nomura, H., Aikawa, Y., Nakagawa, Y., & Millar, T. J. 2009, *A&A*, 495, 183
- Öberg, K. I., Fuchs, G. W., Awad, Z., Fraser, H. J., Schlemmer, S., van Dishoeck, E. F., & Linnartz, H. 2007, *ApJ*, 662, L23
- Öberg, K. I., Linnartz, H., Visser, R., & van Dishoeck, E. F. 2009a, *ApJ*, 693, 1209
- Öberg, K. I., van Dishoeck, E. F., & Linnartz, H. 2009b, *A&A*, 496, 281
- Öberg, K. I., et al. 2011, *ArXiv e-prints*
- Okuzumi, S. 2009, *ApJ*, 698, 1122
- Oppenheimer, M., & Dalgarno, A. 1974, *ApJ*, 192, 29
- Owen, J. E., Ercolano, B., & Clarke, C. J. 2011, *MNRAS*, 412, 13
- Pagani, L., Salez, M., & Wannier, P. G. 1992, *A&A*, 258, 479
- Pagani, L., et al. 2009, *A&A*, 494, 623
- Panić, O., Hogerheijde, M. R., Wilner, D., & Qi, C. 2009, *A&A*, 501, 269
- Pascucci, I., Apai, D., Luhman, K., Henning, T., Bouwman, J., Meyer, M. R., Lahuis, F., & Natta, A. 2009, *ApJ*, 696, 143
- Perez-Becker, D., & Chiang, E. 2011, *ApJ*, 727, 2
- Pierce, D. M., & A'Hearn, M. F. 2010, *ApJ*, 718, 340
- Piétu, V., Dutrey, A., & Guilloteau, S. 2007, *A&A*, 467, 163
- Piétu, V., Guilloteau, S., & Dutrey, A. 2005, *A&A*, 443, 945
- Pontoppidan, K. M., Blake, G. A., van Dishoeck, E. F., Smette, A., Ireland, M. J., & Brown, J. 2008a, *ApJ*, 684, 1323
- Pontoppidan, K. M., Dullemond, C. P., van Dishoeck, E. F., Blake, G. A., Boogert, A. C. A., Evans, II, N. J., Kessler-Silacci, J. E., & Lahuis, F. 2005, *ApJ*, 622, 463
- Pontoppidan, K. M., et al. 2008b, *ApJ*, 678, 1005
- Pratap, P., Dickens, J. E., Snell, R. L., Miralles, M. P., Bergin, E. A., Irvine, W. M., & Schloerb, F. P. 1997, *ApJ*, 486, 862
- Prinn, R. G. P., & Fegley, Jr., B. 1989, *Solar nebula chemistry: origins of planetary, satellite and cometary volatiles*, ed. Atreya, S. K., Pollack, J. B., & Matthews, M. S., 78–136

- Qi, C., Wilner, D. J., Aikawa, Y., Blake, G. A., & Hogerheijde, M. R. 2008, *ApJ*, 681, 1396
- Qi, C., Wilner, D. J., Calvet, N., Bourke, T. L., Blake, G. A., Hogerheijde, M. R., Ho, P. T. P., & Bergin, E. 2006, *ApJ*, 636, L157
- Raunier, S., Chiavassa, T., Marinelli, F., Allouche, A., & Aycard, J.-P. 2003, *The Journal of Physical Chemistry A*, 107, 9335
- Ricci, L., Testi, L., Natta, A., Neri, R., Cabrit, S., & Herczeg, G. J. 2010, *A&A*, 512, A15+
- Rodmann, J., Henning, T., Chandler, C. J., Mundy, L. G., & Wilner, D. J. 2006, *A&A*, 446, 211
- Röllig, M., et al. 2007, *A&A*, 467, 187
- Sakai, N., Shiino, T., Hirota, T., Sakai, T., & Yamamoto, S. 2010, *ApJ*, 718, L49
- Salyk, C., Pontoppidan, K. M., Blake, G. A., Lahuis, F., van Dishoeck, E. F., & Evans, II, N. J. 2008, *ApJ*, 676, L49
- Salyk, C., Pontoppidan, K. M., Blake, G. A., Najita, J. R., & Carr, J. S. 2011, *ApJ*, 731, 130
- Sanford, S. A., Allamandola, L. J., & Geballe, T. R. 1993, *Science*, 262, 400
- Sano, T., Miyama, S. M., Umebayashi, T., & Nakano, T. 2000, *ApJ*, 543, 486
- Sargent, B. A., et al. 2009, *ApJS*, 182, 477
- Sarrasin, E., Abdallah, D. B., Wernli, M., Faure, A., Cernicharo, J., & Lique, F. 2010, *MNRAS*, 404, 518
- Savin, D. W., et al. 2011, *ArXiv e-prints*
- Schoier, F. L., van der Tak, F. F. S., van Dishoeck, E. F., & Black, J. H. 2005, *A&A*, 432, 369
- Schräpler, R., & Henning, T. 2004, *ApJ*, 614, 960
- Schreyer, K., et al. 2008, *A&A*, 491, 821
- Segura, A., Meadows, V. S., Kasting, J. F., Crisp, D., & Cohen, M. 2007, *A&A*, 472, 665
- Selsis, F., Despois, D., & Parisot, J. 2002, *A&A*, 388, 985
- Semenov, D., Chakraborty, S., & Thiemens, M. 2010a, *Chemical and Isotopic Evolution of the Solar Nebula and Protoplanetary Disks*, ed. Apai, D. A. & Lauretta, D. S., 97–127
- Semenov, D., Henning, T., Helling, C., Ilgner, M., & Sedlmayr, E. 2003, *A&A*, 410, 611
- Semenov, D., Pavlyuchenkov, Y., Schreyer, K., Henning, T., Dullemond, C., & Bacmann, A. 2005, *ApJ*, 621, 853
- Semenov, D., Wiebe, D., & Henning, T. 2004, *A&A*, 417, 93
- . 2006, *ApJ*, 647, L57
- Semenov, D., et al. 2010b, *A&A*, 522, A42+
- Shakura, N. I., & Sunyaev, R. A. 1973, *A&A*, 24, 337
- Shalabiea, O. M., & Greenberg, J. M. 1994, *A&A*, 290, 266
- Simon, M., Dutrey, A., & Guilloteau, S. 2000, *ApJ*, 545, 1034
- Smith, I. W. M., Herbst, E., & Chang, Q. 2004, *MNRAS*, 350, 323
- Solomon, P. M., & Wickramasinghe, N. C. 1969, *ApJ*, 158, 449
- Stäuber, P., Doty, S. D., van Dishoeck, E. F., & Benz, A. O. 2005, *A&A*, 440, 949
- Tennekes, P. P., Harju, J., Juvela, M., & Tóth, L. V. 2006, *A&A*, 456, 1037
- Terada, H., Tokunaga, A. T., Kobayashi, N., Takato, N., Hayano, Y., & Takami, H. 2007, *ApJ*, 667, 303
- Thi, W.-F., van Zadelhoff, G.-J., & van Dishoeck, E. F. 2004, *A&A*, 425, 955
- Tscharnutter, W. M., & Gail, H.-P. 2007, *A&A*, 463, 369
- Turner, B. E., Herbst, E., & Terzieva, R. 2000, *ApJS*, 126, 427
- Turner, N. J., Sano, T., & Dziourkevitch, N. 2007, *ApJ*, 659, 729
- Turner, N. J., Willacy, K., Bryden, G., & Yorke, H. W. 2006, *ApJ*, 639, 1218
- Umebayashi, T., & Nakano, T. 1980, *PASJ*, 32, 405
- . 1981, *PASJ*, 33, 617
- van Boekel, R., et al. 2004, *Nature*, 432, 479
- van der Plas, G., van den Ancker, M. E., Acke, B., Carmona, A., Dominik, C., Fedele, D., & Waters, L. B. F. M. 2009, *A&A*, 500, 1137
- van Dishoeck, E. F. 1988, in *ASSL Vol. 146: Rate Coefficients in Astrochemistry*, ed. T. Millar & D. Williams (Kluwer Academic Publishers, Dordrecht), 49–72
- van Dishoeck, E. F., Jonkheid, B., & van Hemert, M. C. 2006, in *Faraday discussion*, Vol. 133, *Chemical evolution of the Universe*, ed. I. R. Sims & D. A. Williams, 231–244
- van Zadelhoff, G.-J., Aikawa, Y., Hogerheijde, M. R., & van Dishoeck, E. F. 2003, *A&A*, 397, 789
- Vasyunin, A. I., Semenov, D., Henning, T., Wakelam, V., Herbst, E., & Sobolev, A. M. 2008, *ApJ*, 672, 629
- Vasyunin, A. I., Semenov, D. A., Wiebe, D. S., & Henning, T. 2009, *ApJ*, 691, 1459
- Vasyunin, A. I., Wiebe, D. S., Birnstiel, T., Zhukovska, S., Henning, T., & Dullemond, C. P. 2011, *ApJ*, 727, 76
- Verner, D. A., Yakovlev, D. G., Band, I. M., & Trzhaskovskaya, M. B. 1993, *Atomic Data and Nuclear Data Tables*, 55, 233
- Visser, R., van Dishoeck, E. F., & Black, J. H. 2009a, *A&A*, 503, 323
- Visser, R., van Dishoeck, E. F., Doty, S. D., & Dullemond, C. P. 2009b, *A&A*, 495, 881
- Wakelam, V. 2009, in *American Astronomical Society Meeting Abstracts*, Vol. 214, *American Astronomical Society Meeting Abstracts*, 402.15–+
- Wakelam, V., & Herbst, E. 2008, *ApJ*, 680, 371
- Wakelam, V., Herbst, E., Le Bourlot, J., Hersant, F., Selsis, F., & Guilloteau, S. 2010a, *A&A*, 517, A21+
- Wakelam, V., Herbst, E., & Selsis, F. 2006, *A&A*, 451, 551
- Wakelam, V., et al. 2010b, *Space Sci. Rev.*, 156, 13
- Walmsley, C. M., & Ungerechts, H. 1983, *A&A*, 122, 164
- Walsh, C., Millar, T. J., & Nomura, H. 2010, *ArXiv e-prints*
- Wehrstedt, M., & Gail, H. 2002, *A&A*, 385, 181
- Willacy, K., Langer, W., Allen, M., & Bryden, G. 2006, *ApJ*, 644, 1202
- Willacy, K., & Langer, W. D. 2000, *ApJ*, 544, 903
- Wilson, T. L., Rohlfs, K., & Hüttemeister, S. 2009, *Tools of Radio Astronomy*, ed. Wilson, T. L., Rohlfs, K., Hüttemeister, S. (Springer-Verlag)
- Woitke, P., Kamp, I., & Thi, W. 2009, *A&A*, 501, 383
- Wolf, S., Gueth, F., Henning, T., & Kley, W. 2002, *ApJ*, 566, L97
- Woodall, J., Agúndez, M., Markwick-Kemper, A. J., & Millar, T. J. 2007, *A&A*, 466, 1197
- Wooden, D., Desch, S., Harker, D., Gail, H.-P., & Keller, L. 2007, in *Protostars and Planets V*, ed. B. Reipurth, D. Jewitt, & K. Keil, 815–833
- Wooden, D. H., Harker, D. E., Woodward, C. E., Butner, H. M., Koike, C., Witteborn, F. C., & McMurry, C. W. 1999, *ApJ*, 517, 1034
- Woods, P. M., & Willacy, K. 2007, *ApJ*, 655, L49
- . 2009, *ApJ*, 693, 1360
- Wünsch, R., Gawryszczak, A., Klahr, H., & Różyczka, M. 2006, *MNRAS*, 367, 773
- Xie, T., Allen, M., & Langer, W. D. 1995, *ApJ*, 440, 674
- Yamamoto, S., Saito, S., Kawaguchi, K., Kaifu, N., & Suzuki, H. 1987, *ApJ*, 317, L119
- Yate, C. J., & Millar, T. J. 2003, *A&A*, 399, 553
- Zasowski, G., Kemper, F., Watson, D. M., Furlan, E., Bohac, C. J., Hull, C., & Green, J. D. 2009, *ApJ*, 694, 459